Consiglio Nazionale delle Ricerche

PUBBLICAZIONE AI SENSI DELL'ART. 19 DEL D.LGS. N. 33 DEL 14 MARZO 2013,
MODIFICATO DALL'ART. 18 DEL D.LGS N. 97 DEL 25 MAGGIO 2016
INTEGRATO DALL'ART.1 C. 145 DELLA LEGGE 27 DICEMBRE 2019 N. 160

BANDO N. 368.36 RIC – AREA STRATEGICA "ATOMI FOTONI MOLECOLE"

CONCORSO PUBBLICO, PER TITOLI ED ESAMI, PER L'ASSUNZIONE CON CONTRATTO DI LAVORO A TEMPO PIENO E INDETERMINATO DI N.7 UNITÀ DI PERSONALE PROFILO RICERCATORE - III LIVELLO PROFESSIONALE - PRESSO STRUTTURE DEL CONSIGLIO NAZIONALE DELLE RICERCHE

TRACCE DELLE PROVE D'ESAME ESTRATTE A SORTE

TRACCIA N.2 A CARATTERE GENERALE

Il candidato descriva una tematica pertinente all'area strategica relativa al presente concorso e che ritiene di particolare interesse descrivendo lo stato dell'arte, i problem aperti, l'impatto che tale ricerca potrebbe produrre ed in particolare le metodologie teoriche e/o sperimentali rilevanti in questo ambito. Il testo deve essere redatto in lingua inglese. Il testo scritto non deve superare la lunghezza di due facciate di foglio protocollo.

The candidate should describe a research topic relevant to the strategic area related to this selection procedure, which he/she considers of particular interest, describing the state of the art, the open problems, the impact that such research could produce and in particular, the relevant theoretical and/or experimental methodologies in this field. The text must be written in English. The written text must not exceed the length of two pages.

TRACCIA N. "A" A CONTENUTO TEORICO-PRATICO

Il candidato scelga uno dei tre articoli proposti e rediga un abstract in inglese della lunghezza massima di 150 parole.

The candidate should choose one of the enclosed papers and write an abstract in English. The abstract must not exceed 150 words.

RESEARCH ARTICLE

The ergodic hypothesis is one of the central principles of statistical physics. In ergodic time evolution of a quantum many-body system, local degrees of freedom become fully entangled with the rest of the system, leading to an effectively classical hydrodynamic evolution of the remaining slow observables (*1*). Hence, ergodicity is responsible for the demise of observable quantum correlations in the dynamics of large many-body systems and forms the basis for the emergence of local thermodynamic equilibrium in isolated quantum systems (*2*–*4*). It is therefore of fundamental interest to investigate how ergodicity breaks down and to understand the long-time stationary states that ensue in the absence of ergodicity.

One path to breaking ergodicity is provided by the study of integrable models, in which thermalization is prevented owing to the constraints imposed on the dynamics by an infinite set of conservation rules. Such models have been realized and studied in a number of experiments with ultracold atomic gases (*5*–*7*). However, integrable models represent very special and fine-tuned situations, making it difficult to extract general underlying principles.

Theoretical studies over the past decade point to many-body localization (MBL) in a disordered isolated quantum system as a more generic alternative to thermalization dynamics. In his original paper on single-particle localization, Anderson already speculated that interacting many-body systems subject to sufficiently strong disorder would also fail to thermalize (*8*). Only recently, however, have convincing theoretical arguments been put forward that Anderson localization remains stable under the addition of moderate interactions, even in highly excited many-body states (*9*–*11*). Further theoretical studies have established the many-body localized state as a distinct dynamical phase of matter that exhibits previously unknown universal behavior (*12*–*22*). In particular, the relaxation of local observables does not follow the conventional paradigm of thermalization and is expected to show explicit breaking of ergodicity (*23*).

Although Anderson localization of noninteracting particles has been experimentally observed in a variety of systems, including light scattering from semiconductor powders in three-dimensional (3D) (*24*), photonic lattices in 1D (*25*) and 2D (*26*), and cold atoms in 1D and 3D random (*27*–*29*) and quasirandom (*30*) disorder, the interacting case has proven more elusive. Initial experiments with interacting systems have focused on the superfluid- (*31*–*33*) or metal-to-insulator (*34*) transition in the ground state. Evidence for inhibited macroscopic mass transport was reported even at elevated temperatures (*34*) but is hard to distinguish from the exponentially slow motion expected from conventional activated transport or effects stemming from the inhomogeneity of the cloud. Possible precursors of MBL have also been reported in a transport experiment by using conventional thin-film electronic insulators (*35*).

Here, we report the experimental observation of ergodicity breaking because of MBL away from the ground state. Our experiments are performed in a 1D system of ultracold fermions in a bichromatic, quasirandomly disordered lattice potential. We identified the many-body localized phase by monitoring the time evolution of local observables following a quench of system parameters. Specifically, we prepared a high-energy initial state with a strong, artificially prepared charge density wave (CDW) order (Fig. 1A) and measured the relaxation of this CDW in the ensuing unitary evolution. Our main observable is the imbalance $\mathcal{I}$ between the respective atom numbers on even (N_e) and odd (N_o) sites

$$\mathcal{I} = \frac{N_e - N_o}{N_e + N_o} \quad (1)$$

which directly measures the CDW order. Although the initial CDW ($\mathcal{I} \sim 0.9$) will quickly relax to zero in the thermalizing case, this is not true in a localized system, in which ergodicity is broken and the system cannot act as its own heat bath (Fig. 1B) (*36*). Intuitively, if the system is strongly localized, all particles will stay close to their original positions during time evolution, thus only smearing out the CDW a little. A longer localization length ξ corresponds to more extended states and will lead to a lower steady-state value of the imbalance. The long-time stationary value of the imbalance thus effectively serves as an order parameter of the MBL phase and allows us to map the phase boundary between the ergodic and nonergodic phases in the parameter space of interaction versus disorder strength. In particular, close to the transition, the imbalance is expected to vanish asymptotically as a power law $\propto 1/\xi^{\alpha}$ with $\alpha > 0$ (*37*). In contrast to previous experiments, which studied the effect of disorder on the global expansion and transport dynamics (*27*, *30*, *31*, *33*, *34*), the CDW order parameter acts as a purely local probe, directly capturing the ergodicity breaking. Although ultimately facing a similar challenge, namely distinguishing very slow dynamics from no dynamics, the CDW is expected to undergo much faster dynamics, facilitating the detection of MBL.

Theoretical model

Our system can be described by the 1D fermionic Aubry-André model (*38*) with interactions (*36*), given by the Hamiltonian

$$\hat{H} = -J\sum_{i,\sigma}(\hat{c}^{\dagger}_{i,\sigma}\hat{c}_{i+1,\sigma} + \text{h.c.}) + \Delta\sum_{i,\sigma}\cos(2\pi\beta i + \phi)\hat{c}^{\dagger}_{i,\sigma}\hat{c}_{i,\sigma} + U\sum_{i}\hat{n}_{i,\uparrow}\hat{n}_{i,\downarrow} \quad (2)$$

Here, J is the tunneling matrix element between neighboring lattice sites, $\hat{c}^{\dagger}_{i,\sigma}$ denotes the creation operator, and $\hat{c}_{i,\sigma}$ denotes the annihilation operator for a fermion in spin state $\sigma \in \{\uparrow, \downarrow\}$ on site i. The second term describes the quasirandom disorder—the shift of the on-site energy due to an additional incommensurate lattice, characterized

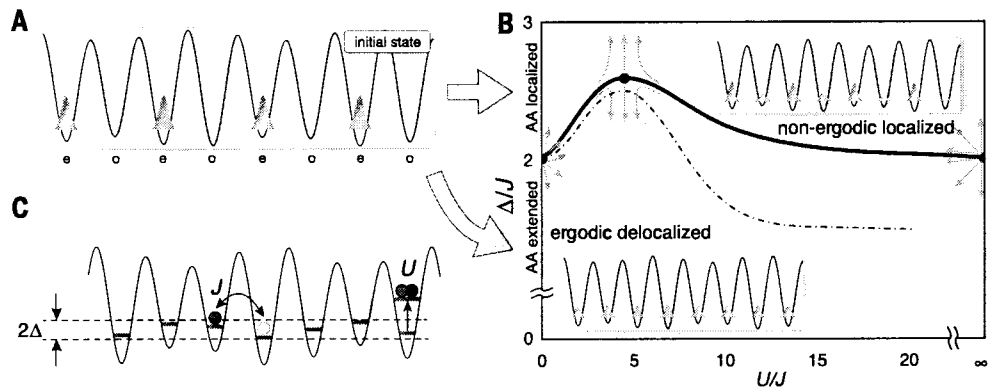

Fig. 1. Schematics of the many-body system, initial state, and phase diagram. (**A**) Initial state of our system consisting of a CDW, in which all atoms occupy even sites (e) only. For an interacting many-body system, the evolution of this state over time depends on whether the system is ergodic or not. (**B**) Schematic phase diagram for the system. In the ergodic, delocalized phase (white), the initial CDW quickly decays, whereas it persists for long times in the nonergodic, localized phase (yellow). The striped area indicates the dependence of the transition on the doublon fraction, with the black solid line indicating the case of no doublons. The black dash-dotted line represents the experimentally observed transition for a finite doublon fraction, extracted from the data in Fig. 4. The gray arrows depict the postulated pattern of renormalization group flows controlling the localization transition. For $U = 0$, as well as in the limit of infinite U with no doublons present (*37*), the transition is controlled by the noninteracting Aubry-André critical point, represented by the unstable gray fixed points. Generically, however, it is governed by the MBL critical point (*48*), shown in red. The $U = 0$ and $U = \infty$ as well as the $\Delta/J = 0$ limits represent special integrable cases that are not ergodic (*51*, *52*). (**C**) A schematic representation of the three terms in the Aubry-André Hamiltonian (Eq. 2).

by the ratio of lattice periodicities β, disorder strength Δ, and phase offset ϕ. Finally, U represents the on-site interaction energy, and $\hat{n}_{i,\sigma} = \hat{c}^{\dagger}_{i,\sigma}\hat{c}_{i,\sigma}$ is the local number operator (Fig. 1C).

This quasirandom model is special in that for almost all irrational β (*37*), all single-particle states become localized at the same critical disorder strength $\Delta/J = 2$ (*38*). For larger disorder strengths, the localization length decreases monotonically. Such a transition was indeed observed experimentally in a noninteracting bosonic gas (*30*). In contrast, truly random disorder will lead to single-particle localization in one dimension already for arbitrarily small disorder strengths. Previous numerical work indicates MBL in quasirandom systems to be similar to that obtained for a truly random potential (*36*).

Experiment

We experimentally realized the Aubry-André model by superimposing on the primary, short lattice (λ_s = 532 nm) a second, incommensurate disorder lattice with λ_d = 738 nm (thus, $\beta = \lambda_s/\lambda_d \approx 0.721$) and control J, Δ, and ϕ via lattice depths and relative phase between the two lattices (*37*). The interactions (U) between atoms in the two different spin states $|\uparrow\rangle$ and $|\downarrow\rangle$ are tuned via a magnetic Feshbach resonance (*37*). In total, this provides independent control of U, J, and Δ and enables us to continuously tune the system from an Anderson insulator in the noninteracting case to the MBL regime for interacting particles.

An additional long lattice (λ_l = 1064 nm = $2\lambda_s$) forms a period-two superlattice (*39*, *40*) together with the short lattice and is used during the preparation of the initial CDW state and during detection (*37*). Deep lattices along the orthogonal directions [$\lambda_\perp$ = 738 nm and $V_\perp = 36(1)E_R$] create an array of decoupled 1D tubes. Here, $E_R = h^2/(2m\lambda_{lat}^2)$ denotes the recoil energy, with h being Planck's constant, m the mass of the atoms, and λ_{lat} the respective wavelength of the lattice lasers.

We used a two-component degenerate Fermi gas of ^{40}K atoms, consisting of an equal mixture of 90×10^3 to 110×10^3 atoms in each of the two lowest hyperfine states $|F, m_F\rangle = |\frac{9}{2}, -\frac{9}{2}\rangle \equiv |\downarrow\rangle$ and $|\frac{9}{2}, -\frac{7}{2}\rangle \equiv |\uparrow\rangle$, at an initial temperature of 0.20(2) T_F, where T_F is the Fermi temperature. The atoms were initially prepared in a finite temperature band insulating state (*41*), with up to 100 atoms per tube in the long and orthogonal lattices. We then split each lattice site by ramping up the short lattice in a tilted configuration (*37*) and subsequently ramped down the long lattice. This creates a CDW, in which there are no atoms on odd lattice sites but zero, one, or two atoms on each even site (*40*, *42*). This initial CDW is then allowed to evolve for a given time in the $8.0(2)E_R$ deep short lattice at a specific interaction strength U in the presence of disorder Δ. In a final step, we detected the number of atoms on even and odd lattice sites by using a band-mapping technique that maps them to different bands of the superlattice (*37*, *42*). This allows us to directly measure the imbalance $\mathcal{I}$, as defined in Eq. 1, in much larger systems than what is numerically feasible.

Results

We tracked the time evolution of the imbalance $\mathcal{I}$ for various interactions U and disorder strengths Δ (Fig. 2). At short times, the imbalance exhibits some dynamics consisting of a fast decay followed by a few damped oscillations. After a few tunneling times $\tau = h/(2\pi J)$, the imbalance approaches a stationary value. In a clean system ($\Delta/J = 0$), and for weak disorder, the stationary value of the imbalance approaches zero. For stronger disorder, however, this behavior changes dramatically, and the imbalance attains a nonvanishing stationary value that persists for all observation times. Because the imbalance must decay to zero on approaching thermal equilibrium at these high energies, the nonvanishing stationary value of $\mathcal{I}$ directly indicates nonergodic dynamics. Deep in the localized phase, in which unbiased numerical density-matrix renormalization group (DMRG) calculations are feasible because of the slow entanglement growth,

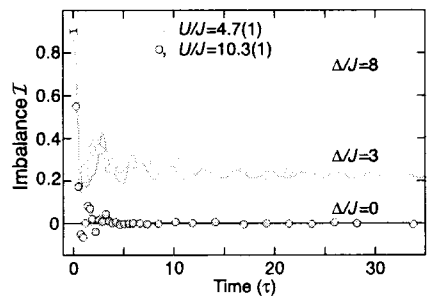

Fig. 2. Time evolution of an initial CDW. A CDW, consisting of fermionic atoms occupying only even sites, is allowed to evolve in a lattice with an additional quasirandom disorder potential. After variable times, the imbalance $\mathcal{I}$ between atoms on odd and even sites is measured. Experimental time traces (circles) and DMRG calculations for a single homogeneous tube (lines) (*37*) are shown for various disorder strengths Δ. Each experimental data point denotes the average of six different realizations of the disorder potential, and the error bars show the SD of the mean. The shaded region indicates the time window used to characterize the stationary imbalance in the rest of the analysis.

we found the stationary value obtained in the simulations to be in very good agreement with the experimental result. These simulations were performed for a single homogeneous tube without any trapping potentials (*37*). The stronger damping of oscillations observed in the experiment can be attributed to a dephasing caused by variations in J between different 1D tubes (*37*, *42*).

We experimentally observed an additional very slow decay of $\mathcal{I}$ on a time scale of several hundred tunneling times for all interaction strengths, which we attribute to the fact that our system is not perfectly closed owing to small background gas losses, technical heating, photon scattering, and coupling to neighboring

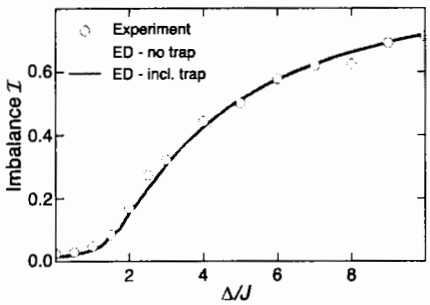

Fig. 3. Stationary values of the imbalance $\mathcal{I}$ as a function of disorder strength Δ for noninteracting atoms. The Aubry-André transition is at $\Delta/J = 2$. Circles show the experimental data, along with exact diagonalization (ED) calculations with (red line) and without (gray line) trap effects (*37*). Each experimental data point is the average of three different evolution times (13.7, 17.1, and 20.5 τ) and four different disorder phases ϕ, for a total of 12 individual measurements per point. To avoid any interaction effects, only a single spin component was used. The ED calculations are averaged over similar evolution times to the experiment and 12 different phase realizations. Error bars show the SD of the mean.

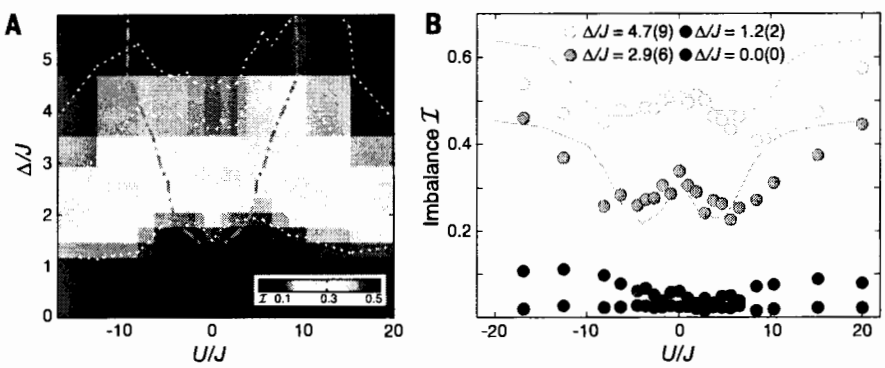

Fig. 4. Stationary imbalance for various interaction and disorder strengths. (**A**) Stationary imbalance $\mathcal{I}$ as a function of interactions U and disorder strength Δ. Moderate interactions reduce the degree of localization compared with the noninteracting or strongly interacting cases. The white dotted lines are contours of equal $\mathcal{I}$, and the solid white line is the contour of $\mathcal{I}$ matching the Aubry-André transition ($U = 0$ and $\Delta/J = 2$) extended to the interacting case. It indicates the MBL transition. The green dot-dashed line shows the fitted minima of $\mathcal{I}$ for each Δ (*37*). Each individual data point (vertices of the pseudo-color plot) is the average of the same 12 parameters as in Fig. 3. The color of each square represents the average imbalance of the four points on the corners. All data were taken with a doublon fraction of 34(2)%. (**B**) Cuts along four different disorder strengths. The effect of interactions on the localization gives rise to a characteristic "W" shape. Solid lines are the results of DMRG simulations for a single homogeneous tube. Error bars indicate the SD of the mean.

tubes (*37*, *43*). Another potential mechanism for delocalization at long times is related to the intrinsic SU(2) spin symmetry in our system (*44*). However, for the relevant observation times our numerical simulations do not indicate the presence of such a thermalization process.

To characterize the dependence of the localization transition on U and Δ, we focused on the stationary value of $\mathcal{I}$, plotted in Fig. 3 for noninteracting atoms and in Fig. 4 for interacting atoms. For noninteracting atoms (Fig. 3), the measured imbalance is compatible with extended states within the finite, trapped system for $\Delta/J \lesssim 2$. Above the critical point of the homogeneous Aubry-André model at $\Delta/J = 2$ (*38*), however, the measured imbalance strongly increases as the single-particle eigenstates become more and more localized. The observed transition agrees well with our theoretical modeling, including the harmonic trap (*37*).

The addition of moderate interactions slightly reduces the degree of localization compared with that of the noninteracting case; they decrease the imbalance $\mathcal{I}$ and hence increase the critical value of Δ necessary to cross the delocalization-localization transition (Fig. 4, A and B). We found that localization persists for all interaction strengths. For a given disorder, the imbalance $\mathcal{I}$ decreases up to a value of $U \sim 2\Delta$ before increasing again. For large $|U|$, the system even becomes more localized than in the noninteracting case. This can be understood qualitatively by considering an initial state consisting purely of empty sites and sites with two atoms (doublons): For sufficiently strong interactions, isolated doublons represent stable quasiparticles because the two atoms cannot separate and hence only tunnel with an effective second-order tunneling rate of $J_D = \frac{2J^2}{|U|} \ll J$ (*45*, *46*). This strongly increases the effective disorder $\propto \Delta/J_D \gg \Delta/J$ and promotes localization. In the experiment, the initial doublon fraction is well below one (*37*), and the density is finite, so that we observed a weaker effect. We found the localization dynamics and the resulting stationary values to be symmetric around $U = 0$, highlighting the dynamical $U \leftrightarrow -U$ symmetry of the Hubbard Hamiltonian for initially localized atoms (*47*). The effect of interactions can be seen in the contour lines (Fig. 4A, dotted white lines) as well as directly in the characteristic "W" shape of the imbalance at constant disorder (Fig. 4B), demonstrating the re-entrant behavior of the system (*22*). This behavior extends to our best estimate of the localization transition, which is shown in Fig. 4A as the solid white line.

We can gain additional insight into how localization changes with interaction strength by computing the growth of the entanglement entropy (*37*) between the two halves of the system during the dynamics (Fig. 5A). For long times, we observed a logarithmic growth of the entanglement entropy with time as $S(t) = S_{\text{offset}} + s_*\ln(t/\tau)$, which is characteristic of the MBL phase (*12*, *13*). The slope s_* is proportional to the bare localization length ξ_*, which in a weakly interacting system in the localized phase corresponds to the single-particle localization length. In general, ξ_* is the characteristic length over which the effective interactions between the conserved local densities decay (*17*, *18*) and connects to the many-body localization length ξ deep in the localized phase. In contrast to ξ, however, ξ_* is expected to remain finite at the transition (*48*). We found s_* to exhibit a broad maximum for intermediate interaction strengths (Fig. 5B), corresponding to a maximum in the thus inferred localization length. This maximum in turn leads to a minimum in the CDW value. Both the characteristic "W" shape in the imbalance and the maximum in the entanglement entropy slope are consequences of the maximum in localization length. Equivalent information on the localization properties as obtained from the entanglement entropy can be gained in experiments by monitoring the temporal decay of fluctuations around the stationary value of the CDW (*37*). Although we do not have sufficient sensitivity to measure these fluctuations in the current experiment, we expect them to be accessible to experiments with single-site resolution (*49*, *50*).

To systematically study the effect of the initial energy density on the MBL phase, we loaded the lattice using either attractive, vanishing, or repulsive interactions (Fig. 6), predominantly changing the number of doublons in the initial state (*37*). Because the initial state consists of fully localized particles only, the local energy density is directly given by the product of interaction strength U and doublon density. We found that for an interaction strength during the evolution of $|U/J| \leq 6$, the energy density does not substantially affect the localization properties, proving that MBL persists over a wide energy range. For $|U/J| > 8$, localization properties depend substantially on the doublon fraction because of the second emerging energy scale J_D, as discussed above. Thus, the localization transition can be tuned via changing the doublon fraction at large U. This constitutes a direct observation of a many-body mobility edge because the doublon density dominates the energy density.

For the case of repulsive loading, which results in a low fraction of doubly occupied sites, the imbalance for $U/J = 0$ and strong interactions match within error. Indeed, a rigorous mapping

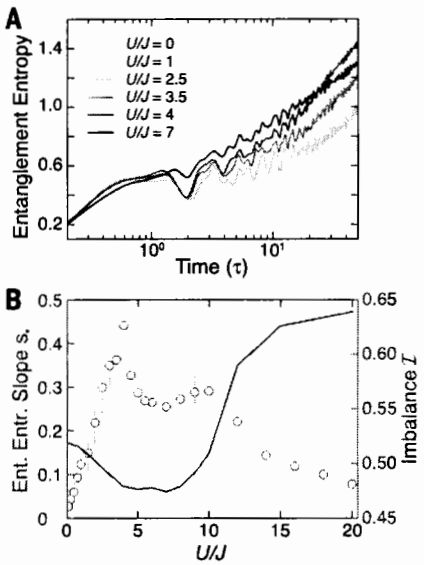

Fig. 5. Calculated growth of entanglement entropy and corresponding slope. (**A**) DMRG results of the entanglement entropy growth (*37*) for various interaction strengths and $\Delta/J = 5$. For long times, logarithmic growth characteristic of interacting MBL states is visible. The experimentally used evolution times indicated by the yellow shaded region are found to be in the region of logarithmic growth. (**B**) The slope of the logarithmic growth (circles), extracted by using linear fits up to the longest simulated time (50 τ) in (A), shows a nonmonotonic dependence on the interaction strength, which is correlated with the inverse of the steady-state value of the CDW order parameter (red line). Error bars reflect different initial starting times for the fit.

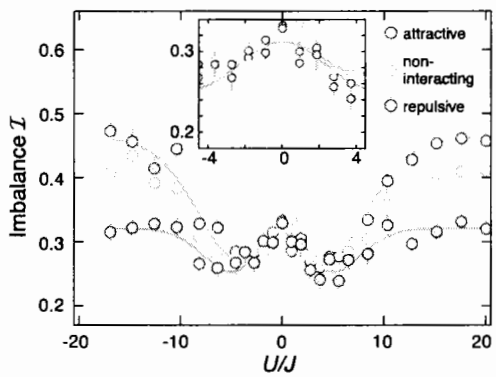

Fig. 6. Stationary imbalance $\mathcal{I}$ as a function of interaction strength during loading. Data were taken with disorder $\Delta/J = 3$. The loading interactions of $a_{load} = -89(2)\ a_0$ (attractive, where a_0 denotes Bohr's radius), $0(1)\ a_0$ (noninteracting), and $142(1)\ a_0$ (repulsive) correspond to initial doublon fractions of 51(1), 43(2), and 8(6)%, respectively (*39*). Each $\mathcal{I}$ value is the average of the same 12 parameters as in Fig. 3. Error bars show the SD of the mean. Solid lines are guides to the eye. The gray shaded area spans the limiting cases of 0 and 50% doublons, simulated by using DMRG for a single homogeneous tube.

can be made between the noninteracting system and the dynamics in the doublon-free subspace at strong interactions $|U/J| \to \infty$ (*37*). At very large interactions and high doublon fractions, the additional long time scales start to also compete with heating and loss processes, rendering the definition of stationary states challenging.

Conclusion

Our experimental demonstration of ergodicity breaking because of MBL paves the way for many further investigations. An interesting extension would be to use "true" random disorder created by, for example, an optical speckle pattern, as has been used to study Anderson localization (*27*). Another important next step is extending the present study to higher dimensions. Additional insight can also be gained by analyzing the full relaxation dynamics of local observables (*19*–*21*) in an experimental setup featuring single-site resolution (*49*, *50*). For instance, the decay of fluctuations of $\mathcal{I}$ with time could be directly measured, providing an even more direct connection to the entanglement entropy. Another important direction for future investigation is the effect of opening the system in a controlled way. This could be done, for example, by adding a near-resonant laser so as to deliberately enhance photon scattering or by using a Bose-Fermi mixture, in which excitations of the Bose-Einstein condensate form a well-controlled bath for the fermions. This will allow a systematic study of the critical dynamics associated with the MBL phase transition, in which the bath relaxation time now provides the only scale. Such a study would also allow the MBL phase to be clearly distinguished experimentally from classical glassy dynamics. The latter, unlike MBL, is insensitive to coupling of the system to an external bath.

REFERENCES AND NOTES

1. J. Lux, J. Müller, A. Mitra, A. Rosch, *Phys. Rev. A* **89**, 053608 (2014).
2. J. M. Deutsch, *Phys. Rev. A* **43**, 2046–2049 (1991).
3. M. Srednicki, *Phys. Rev. E Stat. Phys. Plasmas Fluids Relat. Interdiscip. Topics* **50**, 888–901 (1994).
4. M. Rigol, V. Dunjko, M. Olshanii, *Nature* **452**, 854–858 (2008).
5. B. Paredes *et al.*, *Nature* **429**, 277–281 (2004).
6. T. Kinoshita, T. Wenger, D. S. Weiss, *Nature* **440**, 900–903 (2006).
7. M. Gring *et al.*, *Science* **337**, 1318–1322 (2012).
8. P. W. Anderson, *Phys. Rev.* **109**, 1492–1505 (1958).
9. D. M. Basko, I. L. Aleiner, B. L. Altshuler, *Ann. Phys.* **321**, 1126–1205 (2006).
10. I. V. Gornyi, A. D. Mirlin, D. G. Polyakov, *Phys. Rev. Lett.* **95**, 206603 (2005).
11. J. Z. Imbrie, On many-body localization for quantum spin chains. http://arxiv.org/abs/1403.7837 (2014).
12. M. Žnidarič, T. Prosen, P. Prelovšek, *Phys. Rev. B* **77**, 064426 (2008).
13. J. H. Bardarson, F. Pollmann, J. E. Moore, *Phys. Rev. Lett.* **109**, 017202 (2012).
14. B. Bauer, C. Nayak, *J. Stat. Mech.* **09**, P09005 (2013).
15. R. Vosk, E. Altman, *Phys. Rev. Lett.* **110**, 067204 (2013).
16. M. Serbyn, Z. Papić, D. A. Abanin, *Phys. Rev. Lett.* **110**, 260601 (2013).
17. M. Serbyn, Z. Papić, D. A. Abanin, *Phys. Rev. Lett.* **111**, 127201 (2013).
18. D. A. Huse, R. Nandkishore, V. Oganesyan, *Phys. Rev. B* **90**, 174202 (2014).
19. F. Andraschko, T. Enss, J. Sirker, *Phys. Rev. Lett.* **113**, 217201 (2014).
20. R. Vasseur, S. A. Parameswaran, J. E. Moore, *Phys. Rev. B* **91**, 140202 (2015).
21. M. Serbyn, Z. Papić, D. A. Abanin, *Phys. Rev. B* **90**, 174302 (2014).
22. Y. Bar Lev, G. Cohen, D. R. Reichman, *Phys. Rev. Lett.* **114**, 100601 (2015).
23. A. Pal, D. A. Huse, *Phys. Rev. B* **82**, 174411 (2010).
24. D. S. Wiersma, P. Bartolini, A. Lagendijk, R. Righini, *Nature* **390**, 671–673 (1997).
25. Y. Lahini *et al.*, *Phys. Rev. Lett.* **100**, 013906 (2008).
26. T. Schwartz, G. Bartal, S. Fishman, M. Segev, *Nature* **446**, 52–55 (2007).
27. J. Billy *et al.*, *Nature* **453**, 891–894 (2008).
28. S. S. Kondov, W. R. McGehee, J. J. Zirbel, B. DeMarco, *Science* **334**, 66–68 (2011).
29. F. Jendrzejewski *et al.*, *Nat. Phys.* **8**, 398–403 (2012).
30. G. Roati *et al.*, *Nature* **453**, 895–898 (2008).
31. B. Deissler *et al.*, *Nat. Phys.* **6**, 354–358 (2010).
32. B. Gadway, D. Pertot, J. Reeves, M. Vogt, D. Schneble, *Phys. Rev. Lett.* **107**, 145306 (2011).
33. C. D'Errico *et al.*, *Phys. Rev. Lett.* **113**, 095301 (2014).
34. S. S. Kondov, W. R. McGehee, W. Xu, B. DeMarco, *Phys. Rev. Lett.* **114**, 083002 (2015).
35. M. Ovadia, D. Kalok, I. Tamir, S. Mitra, B. Sacepe, D. Shahar, Evidence for a finite temperature insulator. http://arxiv.org/abs/1406.7510 (2014).
36. S. Iyer, V. Oganesyan, G. Refael, D. A. Huse, *Phys. Rev. B* **87**, 134202 (2013).
37. Materials and methods are available as supplementary materials on *Science* Online.
38. S. Aubry, G. André, *Ann. Israel Phys. Soc.* **3**, 133 (1980).
39. J. Sebby-Strabley, M. Anderlini, P. S. Jessen, J. V. Porto, *Phys. Rev. A* **73**, 033605 (2006).
40. S. Fölling *et al.*, *Nature* **448**, 1029–1032 (2007).
41. U. Schneider *et al.*, *Science* **322**, 1520–1525 (2008).
42. S. Trotzky *et al.*, *Nat. Phys.* **8**, 325–330 (2012).
43. H. Pichler, A. J. Daley, P. Zoller, *Phys. Rev. A* **82**, 063605 (2010).
44. R. Vasseur, A. C. Potter, S. A. Parameswaran, *Phys. Rev. Lett.* **114**, 217201 (2015).
45. K. Winkler *et al.*, *Nature* **441**, 853–856 (2006).
46. S. Trotzky *et al.*, *Science* **319**, 295–299 (2008).
47. U. Schneider *et al.*, *Nat. Phys.* **8**, 213–218 (2012).
48. R. Vosk, D. A. Huse, E. Altman, Theory of the many-body localization transition in one dimensional systems. http://arxiv.org/abs/1412.3117 (2014).
49. W. S. Bakr, J. I. Gillen, A. Peng, S. Fölling, M. Greiner, *Nature* **462**, 74–77 (2009).
50. J. F. Sherson *et al.*, *Nature* **467**, 68–72 (2010).
51. F. Essler, H. Frahm, F. Göhmann, A. Klümper, V. Korepin, *The One-Dimensional Hubbard Model* (Cambridge Univ. Press, Cambridge, UK, 2005).
52. C. Gramsch, M. Rigol, *Phys. Rev. A* **86**, 053615 (2012).

ACKNOWLEDGMENTS

We acknowledge useful discussions with F. Essler and technical assistance by D. Garbe and F. Görg during the setup of the experiment. We acknowledge financial support by the Deutsche Forschungsgemeinschaft (FOR801, Deutsch-Israelisches Kooperationsprojekt Quantum phases of ultracold atoms in optical lattices), the European Commission (UQUAM and AQuS), the U.S. Defense Advanced Research Projects Agency (Quantum Emulations of New Materials Using Ultracold Atoms), the Minerva Foundation, ISF grant no. 1594/11, Nanosystems Initiative Munich (NIM), and the Swiss Society of Friends of the Weizmann Institute.

SUPPLEMENTARY MATERIALS

www.sciencemag.org/content/349/6250/842/suppl/DC1
Supplementary Text
Figs. S1 to S9
References (*53*–*62*)

22 January 2015; accepted 21 July 2015
Published online 30 July 2015
10.1126/science.aaa7432

A2)

ARTICLE

Early electronic computers exploited analogies with acoustic, thermal or mechanical phenomena, such as capacitance for spring stiffness, to simulate a range of practically relevant physical systems. Whereas modern digital simulations have become versatile foundational tools in science and engineering, all classical computers are fundamentally inefficient at tackling exponentially complex microscopic behaviour such as the quantum dynamics of molecules[1,2]. A proposed solution is to engineer quantum mechanical components into devices that are then inherently capable of simulating quantum systems[3–6]. Here, we demonstrate how integrated quantum photonics can be used to develop simulation methods for molecular quantum dynamics, by building on the analogies between optical modes in waveguides and vibrational modes in molecules and between single photons and quantized vibrational excitations.

Advances in the control of ultrafast molecular dynamics have revealed the importance of quantum interference among vibrational modes in behaviour such as bond-selective chemistry[2]. In applying optimal control theory to a harmonic model of chained atoms[7], it has been shown in principle how a control field could drive the dynamics of quantum interference between vibrational modes[8] to excite local bonds. However, laboratory demonstrations of selective bond dissociation required adaptive feedback control to put the principles into practice[9]. Further control over vibrational wavepackets has enabled selective dissociation governed by a single quantum of vibrational energy[10], manipulation of individual molecules at ambient conditions[11], preparations of coherent superpositions on sub-femtosecond timescales[12], and single vibrational states of ultracold molecules[13]. Molecular dynamics are now observable on their ultrafast intrinsic timescale[14].

The prospect of more sophisticated control with quantum states of light and for larger molecules increases the challenge of simulating dynamic behaviour. Light–matter interaction with squeezed states has been demonstrated experimentally in several contexts (see, for example, ref. [15]); enhanced spectroscopy and the control of molecules with multi-mode, multi-photon states has been shown theoretically (see, for example, ref. [16]), with techniques for pulse shaping of quantum states of light also demonstrated (see, for example, ref. [17]). Evolving a multi-excitation state across many vibrational modes is computationally inefficient even for the basic model in which normal modes are described as independent quantum harmonic oscillators. Owing to their bosonic nature, the probability amplitudes for input–output transitions among the modes are determined by matrix permanents, the calculation of which is generally extremely complex[18]. More detailed molecular models, for example, with anharmonic corrections to the potentials, are also likely to be computationally complex.

Quantum algorithms for the efficient simulation of Hamiltonian dynamics[4,19] have been a strong motivator for digital quantum computers, such as those that use trapped ions[20]. Promising digital algorithms for simulating reaction dynamics[21] and obtaining thermal rate constants[22] have been presented that harness the exponential quantum speed-up. Yet, achieving fault tolerance[23] and the high logical-gate counts[24] that enable these applications is extremely challenging. Ansatz-based methods, such as the variational approach for solving the eigenvalue problem[25], have reduced demands, as demonstrated recently with superconducting qubits[26], but the difficulties associated with applying such an approach to Hamiltonian dynamics have yet to be overcome. Analogue quantum simulations[6], in which a quantum system of interest can be mapped directly onto a quantum technological platform, may enable practical advantages in the nearer-term.

Progress in photonic quantum technologies over the past decade has seen the introduction of on-chip processing of photonic quantum information[27–29], full reprogrammability for linear optical circuitry[30], and the integration of photon generation[31,32] and detection[33]. Solid-state single-photon sources[34] and high-efficiency detectors[35] have recently been demonstrated as a solution to achieving large numbers of photons. Ultimately, basic methods to correct for photon loss are likely to be required before photonic quantum simulations outperform

classical algorithms[36], but the demands on error correction for specialized quantum simulators could be much lower than those for universal digital quantum simulators[37]. Here, our focus is on establishing programmable linear optical circuitry as a core capability for simulating the vibrational dynamics of the atoms within molecules.

Simulation procedure

Diagonalizing the Hessian matrix of a molecule in mass-weighted coordinates provides its vibrational spectrum and normal modes, which define a Hamiltonian of independent quantum harmonic oscillators:

$$\hat{H} = \sum_i \hbar\omega_i a_i^\dagger a_i$$

where $\hbar$ is the reduced Planck constant, ω_i is the angular frequency of the ith mode, and $a_i^\dagger$ and a_i are the bosonic creation and annihilation operators of the ith mode. The spatial localization of vibrational energy is important for understanding many molecular phenomena, such as energy transport and dissociation. We therefore consider a basis transformation

$$a_i^\dagger \rightarrow \sum_k U_{ki}^{\mathrm{L}} a_k^\dagger$$

where U^{L} is a unitary matrix, to a set of modes localized around a single atomic site or chemical bond. Dynamics in the localized basis can then be simulated via the model Hamiltonian

$$\hat{H}_{\mathrm{L}} = \sum_{k,j} H_{kj}^{\mathrm{L}} a_k^\dagger a_j$$

where

$$H_{kj}^{\mathrm{L}} = \sum_i \hbar\omega_i U_{ki}^{\mathrm{L}} \overline{U_{ji}^{\mathrm{L}}}$$

and the overbar denotes complex conjugation.

This general model can be simulated directly for m vibrational modes of any given molecule with a linear optical chip that can be programmed to implement any unitary operation over m modes. Reconfiguring such a device to implement the unitary transfer matrix $U(t_i) = \exp(-iH^{\mathrm{L}}t_i/\hbar)$ for a series of time steps $\{t_i\}$ enables simulation of the Hamiltonian $\hat{H}_{\mathrm{L}}$ on any initial multi-mode vibrational state via its mapping to a multi-mode optical input state. Here, we use a silica-on-silicon integrated photonic chip that is fully programmable over six waveguides via 30 thermo-optic phase shifters[30] to perform molecular simulations of up to six-mode vibrational systems. We simulate initial states of up to four vibrational quanta, with states of up to four single photons, produced from spontaneous parametric downconversion sources. Photons are detected with single-photon counting modules. The number and pattern of photons collected at the output of the optical modes for each circuit configuration are governed by the probabilities for the molecule to be found in the corresponding vibrational states at the corresponding time step.

Vibrational dynamics of four-atom molecules

Thioformaldehyde (H_2CS), a key molecule for spectroscopic experiments, is shown in Fig. 1a with its normal-mode spectrum. The six localized vibrational modes of H_2CS comprise two CH stretch modes, two CH bend modes, a CS stretch mode and a wagging mode, which are mapped to our photonic chip from the normal-mode basis, as depicted conceptually in Fig. 1b. We initialized the simulation for the state $|\mu\rangle \propto \mu|1_{\mathrm{CHs1}}, 1_{\mathrm{CHs2}}\rangle + \mu^2|2_{\mathrm{CHs1}}, 2_{\mathrm{CHs2}}\rangle$ (with small squeezing parameter μ), which consists of multiple excitations superposed over the two CH stretch modes ('CHs1' and 'CHs2'), by injecting the two-mode squeezed vacuum state that was produced by the spontaneous parametric downconversion source, into the two waveguides that correspond to the CH stretch modes. Photons were collected over a series of circuit configurations that correspond to time steps of the H_2CS local-basis Hamiltonian. In Fig. 1c we display the experimentally simulated evolution of the probabilities for excitations to be found in only the CH stretch modes, in only the CH bend modes and shared between these stretch and bend modes, for the two-excitation (upper panel) and four-excitation subspace (lower panel).

Dynamics in the two-excitation subspace involve both excitations oscillating between stretch and bend modes via the intermediate state in which one excitation is in each of the subspaces. The L^1 distance

$$\mathcal{D}(\boldsymbol{p}, \boldsymbol{q}) = \frac{1}{2}\sum_i |p_i - q_i|$$

between the results for an experimentally simulated time step ($\boldsymbol{p}$) and the ideal distribution ($\boldsymbol{q}$) is averaged over all time steps to give $\bar{\mathcal{D}} = 0.06 \pm 0.03$. In the four-excitation subspace, in which both of the stretch modes are initially doubly occupied, the experimentally simulated evolutions of probabilities for both stretch modes to remain doubly occupied, for both bend modes to become doubly occupied, and for combinations of one doubly occupied stretch mode and one doubly occupied bend mode are shown. The apparent damping of the oscillatory behaviour between these probabilities is attributable to the combinatorially growing space of multiple excitations available to the evolving state. The distance between the experimentally simulated and ideal evolutions for the full four-photon distributions, averaged over all time steps, is $\bar{\mathcal{D}} = 0.16 \pm 0.07$. The full distributions for these and all subsequent experiments are provided in Supplementary Information.

Because time is a programmable parameter in our simulator, we are able to study molecular vibrations whose evolution involves different timescales, such as the local CH stretch mode in H_2CS, which is a superposition of normal modes with lower and higher frequencies. The probability for a single excitation to remain localized in a CH stretch mode was simulated on two timescales that differ by an order of magnitude. Heralded single photons were injected into the mode that corresponds to a local CH stretch. The circuit was programmed to implement sets of unitary transformations that correspond to a short (30 fs) high-resolution window and that correspond to a longer (300 fs) low-resolution window, the behaviour of which can be observed by averaging over the high-resolution windows. In Fig. 1d we display data for these simulations, which exhibit both higher- and lower-frequency oscillations. Averaging over both evolutions gives a mean distance of $\bar{\mathcal{D}} = 0.014 \pm 0.006$.

Our six-mode simulator can explore the full space of vibrational dynamics for a general molecule of up to four atoms, as we demonstrate for P_4, SO_3, HNCO, HFHF and N_4. In Fig. 1e–i we show the time evolution of a single excitation initially prepared in a local stretch mode. The change in the occupation probability to a second, spectrally overlapped (coupled) local mode is plotted. We observe dynamics with varying characteristic times governed by the vibrational spectra of the molecules. Owing to its geometry and bonding structure, P_4 has the longest-period oscillations between opposing stretches, with SO_3 showing similar stretch-mode coupling behaviour on shorter timescales. By contrast, HNCO and HFHF display faster dynamics with increased mode coupling between hydrogen-bond stretches and bends. In Fig. 1i we show the dynamics of both a single excitation and two excitations initially prepared in stretch modes of N_4. The additional structure in the vibrational spectrum and the introduction of multi-photon quantum interference results in a more complex time dependence of the detection probabilities. The average L^1 distance over all of these experiments is $\bar{\mathcal{D}} = 0.022 \pm 0.007$.

Decoherence and energy transfer in NMA

The flow of vibrational energy in molecules is a fundamental process for chemical reaction rates and functionality in biomolecules[38]. The vibrational quantum dynamics of a molecule within an environment can be described by the interplay of coherent unitary evolution and incoherent dephasing that results from random fluctuations of the

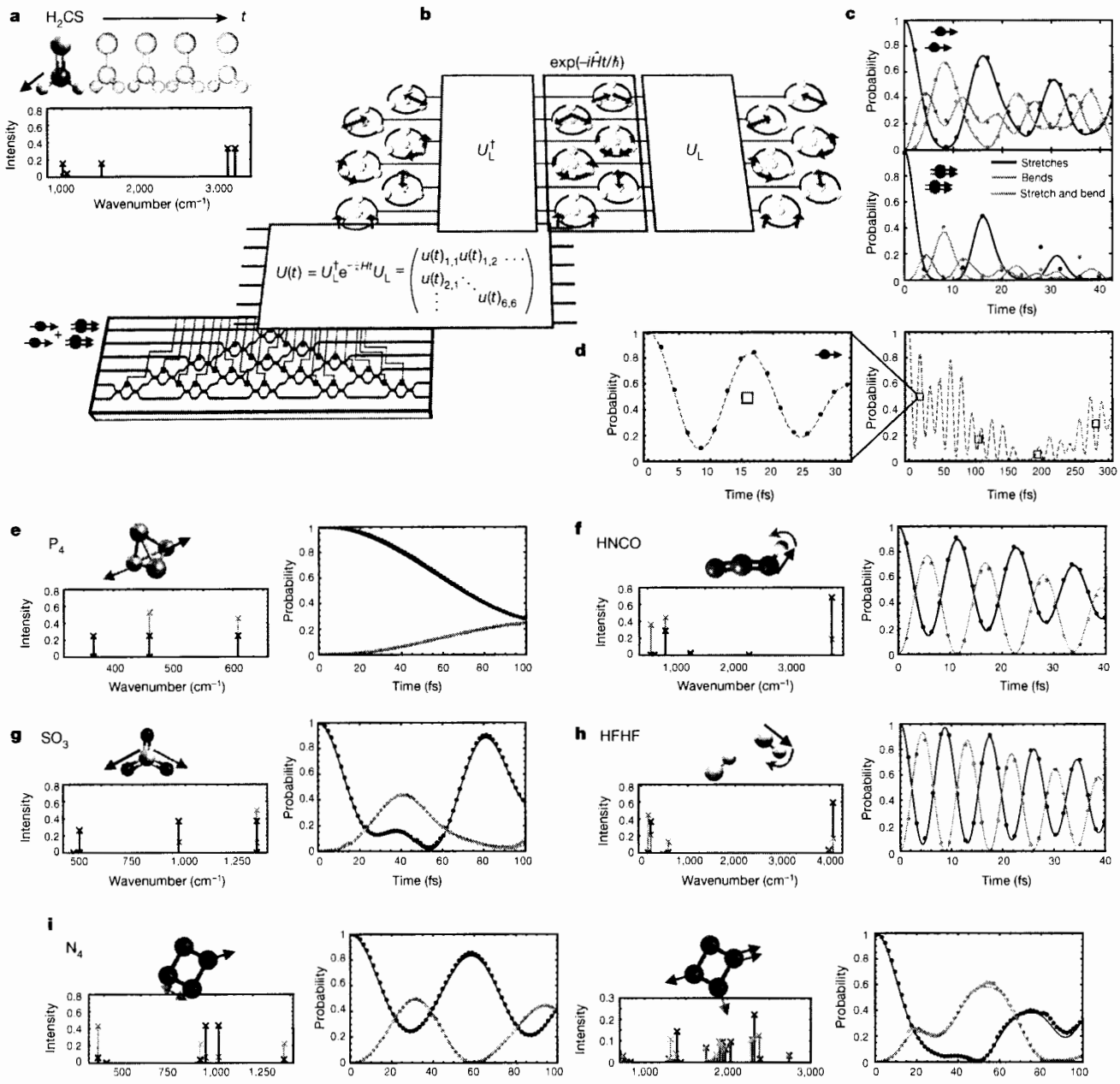

Fig. 1 | Simulating the vibrational dynamics of four-atom molecules in the harmonic approximation. a, Schematic evolution of a localized CH stretch mode (diagonal black arrow) in H_2CS, with its composition from normal modes plotted below. **b**, The evolution of the normal modes ($\exp(-i\hat{H}t/\hbar)$), shown schematically in the center of the top layer, is unitarily mapped (U_L and $U_L^\dagger$) to a set of local vibrational modes, shown schematically at the ends of the top layer. This transformation is then mapped to a time-dependent unitary transfer matrix ($U(t)$; middle layer). Simulations of photonic states under this evolution are then implemented by a reconfigurable photonic chip (bottom layer). **c**, An initial superposition of two and four excitations evolving in the localized stretch modes is simulated by injecting a two-mode squeezed vacuum state into the corresponding optical modes and collecting photon statistics for the sequence of simulated time steps. Top and bottom panels show results for the two- and four-excitation subspaces, respectively (see insets). **d**, Simulations on two timescales of the evolving probability for a single excitation to remain in a CH stretch mode. Blue squares represent the mean probability over a 30-fs window (as per left panel). **e**–**i**, The simulated evolution of a single excitation in P_4 (**e**), SO_3 (**g**), HNCO (**f**) and HFHF (**h**) between a local stretch mode (black) and another coupled local mode (blue). The local modes are represented diagrammatically alongside the spectral intensities of the normal modes involved. For N_4 (**i**), results are also shown for the evolution of two excitations. All data are plotted together with ideal theoretical curves; error bars displaying 1 s.d. from Poissonian statistics are very small.

vibrational frequencies—a process referred to as spectral diffusion. *N*-methylacetamide (NMA) is the simplest molecular model (Fig. 2a) of the peptide bond in proteins, where quantum coherence may have a role in energy transfer[39]. In this section, we simulate a model for intramolecular energy transport in NMA in the presence of dephasing.

We consider a subspace that spans six backbone vibrational modes, which support a basis of approximately localized vibrational modes, including two rocking modes (curved arrows in Fig. 2) and two stretch modes (straight arrows in Fig. 2). Uniform dephasing between all modes is achieved by a time-dependent statistical averaging over the set of experiments with transfer

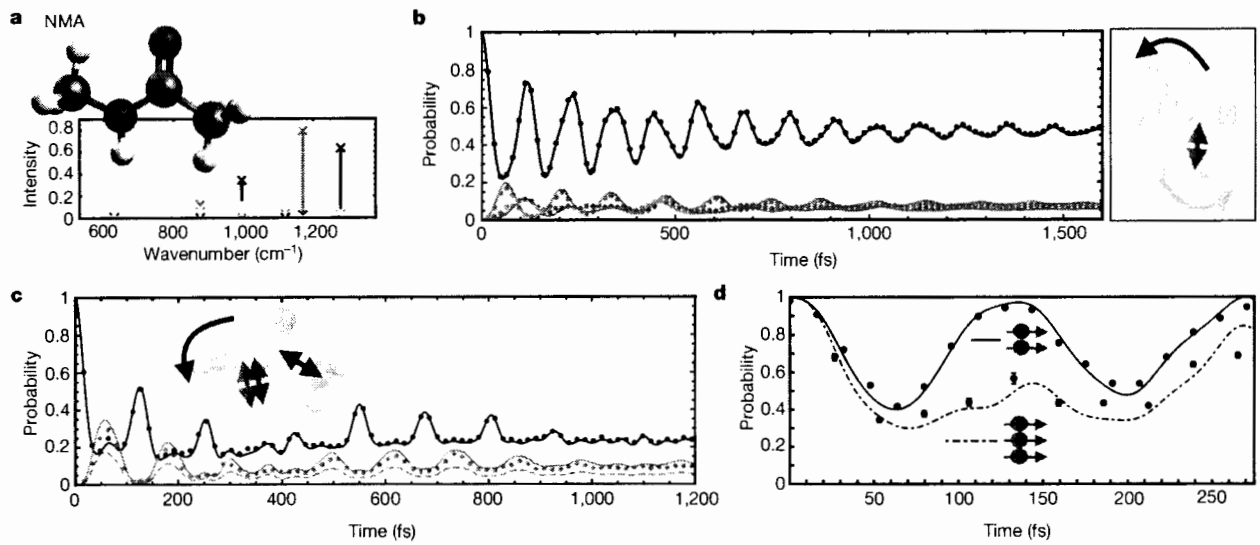

Fig. 2 | Quantum energy transfer and dephasing in NMA. a, A six-mode vibrational subspace of the NMA molecule is considered, with the spectral components of three localized modes colour-coded as per the arrows in **b**. **b**, Experimental simulation results for the probability of a single excitation (black points) that is initially in a local rocking mode (black arrow) at one end of the molecule and its transfer (blue and grey points) to local modes at the opposite end (blue and grey arrows) when subject to a dephasing channel with $T_2 = 0.53$ ps. **c**, Experimental simulation results for the evolution of a two-excitation state (black points) that is initially in separate local modes (black arrows) and its probability (blue points) of being found bunched in the NH stretch mode (blue arrows) under the same dephasing channel. Solid lines represent theory. The dashed blue line plots a theoretical curve for distinguishable (or classical) excitations to be found bunched in the NH stretch mode. **d**, Experimental simulation results for the total probability of measuring a fully anti-bunched state of two excitations with the same intial state as for **c** (black points with solid black theory curve) and of measuring a fully anti-bunched state of three excitations initialized in the modes shown in **b** (black points with dot-dashed theory curve). All error bars represent 1-s.d. estimates from Poissonian statistics.

matrices $U(t_i,k) = U_L Z(k) U_L^{\dagger} \exp(-iH^L t_i/\hbar)$, where $Z(k)$ are Heisenberg–Weyl matrices (defined in Supplementary Information) labelled by k and the average is taken over k at each time step.

Using a single photon, we simulated the probability for a single excitation initialized in a local rocking mode at one end of the molecule to be transferred to two localized modes (a rocking mode and a CC stretch mode) at the opposite end of the molecule. The experimental results shown in Fig. 2b show dynamics that are initially oscillatory, with vibrational energy transfer between the rocking modes at either end of the molecule via an intermediate CC stretch mode. The increasing effect of the suppression of coherence from dephasing results in evolution towards a steady state. Peak probabilities for energy to be localized at either end of the molecule are higher under quantum coherent dynamics than under purely ballistic classical dynamics. We used a T_2 time constant of coherence decay of 0.53 ps, but any time constant can be simulated by changing only the post-processing of data.

Simulating multiple excitations allows us to investigate the interplay of dephasing and quantum interference for multi-excitation energy transport. By injecting one photon into the waveguide that corresponds to the rocking mode and another photon into the waveguide that corresponds to the CC stretch mode, which are each localized at opposite ends of the NMA molecule (black arrows in Fig. 2c), we simulated the change in the probability for this state and for the state in which both excitations 'bunch' in an NH stretch mode (double blue arrows in Fig. 2c). The results in Fig. 2c show more complex oscillatory transfer between these bunched and anti-bunched states, which again tends towards a steady state. However, after full dephasing has occurred, the probability for two excitations to be bunched in the NH stretch mode is twice as high for excitations that behave as indistinguishable bosonic particles than for excitations that behave as distinguishable or classical particles (such as two excitations that pass through the molecule at different times).

For a given molecule, the probability that no bunching occurs (multiple excitations not localized around the same bond) generally decreases as the number of excitations increases[40]. In Fig. 2d the probability for the subspace of no-bunching events is simulated for two and three excitations under fully coherent dynamics. The initial state for the two-excitation evolution is the same as in the previous example; the initial state for the three-excitation evolution comprises an excitation in each of the local modes shown in Fig. 2b. The average distances across all single-, two- and three-excitation distributions in these examples are 0.017 ± 0.005, 0.05 ± 0.01 and 0.14 ± 0.07, respectively.

Vibrational relaxation in liquid water

We now consider extensions to the idealized model of uncoupled harmonic oscillators to account for more realistic situations, including energy dissipation and anharmonic potentials. We choose models for H_2O to demonstrate our techniques.

For a molecule that interacts with its environment, vibrational energy is exchanged via intra- and intermolecular coupling to other degrees of freedom, eventually leading to thermalization. This process is known as vibrational relaxation, and its pathways for H_2O remain an area of investigation[41,42]. Here we simulate the relaxation of H_2O via an amplitude-damping model (Fig. 3a).

We consider a Lindblad master equation, which results in a set of time-dependent Kraus operators that can be simulated via an ensemble of transfer matrices. This evolution cannot be described as a convex sum of unitary evolutions as in the previous section; however, the transfer matrices can be realized within a unitary matrix of twice the size, via unitary dilation[43]. Because H_2O has three vibrational modes, its three-dimensional (non-unitary) transfer matrices can be realized within a six-dimensional unitary matrix and implemented on our six-mode chip (Fig. 3b). We used experimentally measured relaxation times $\{\Gamma_i\}$ for liquid water at room temperature[41] in the model.

We simulated the thermalization of an excitation in a local OH stretch mode via the symmetric bend normal mode to its ground state of no excitations. In Fig. 3c we show the probability of measuring the excitation in the two local stretch modes (left panel) and the symmetric bend mode (right panel). Oscillations between the two high-energy stretch modes decay as the population is transferred via the lower-energy bend mode to the ground state. The average L^1 distance in these experiments was $\bar{D} = 0.024 \pm 0.007$.

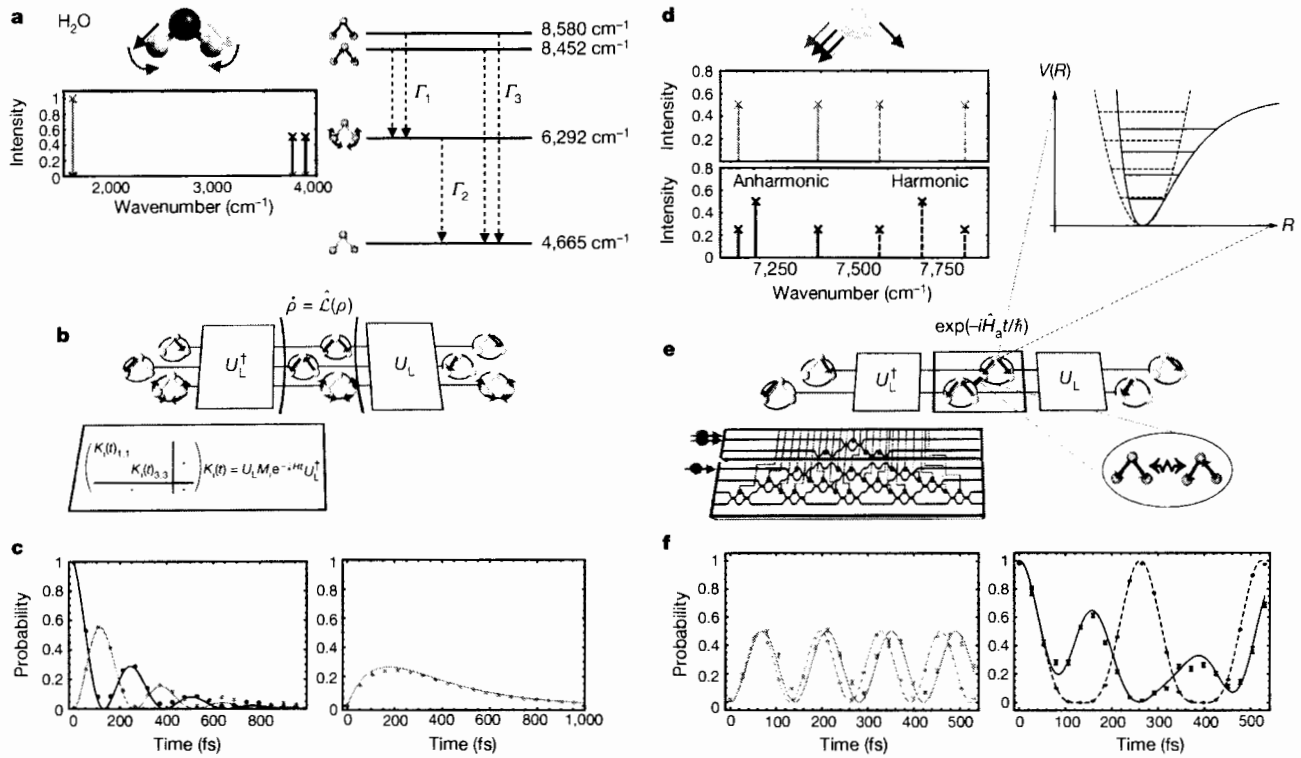

Fig. 3 | Vibrational relaxation and anharmonic evolution for H_2O. **a**, Energy-level diagram for single-excitation harmonic levels and the ground state of H_2O (right) along with the spectral components of the two local OH stretch modes (black and grey) and the symmetric bend normal mode (blue) (left). $\Gamma_{1,2,3}$ are the characteristic decay rates obtained from experiments. **b**, The open-system dynamics of vibrational relaxation, described by the Lindblad equation $\dot{\rho} = \hat{\mathcal{L}}(\rho)$ where ρ is the vibrational state, can be simulated by statistically averaging the evolution under a set of linear operators implemented via unitary dilation. The Krauss operators in the localized basis, $K(t)$, are dilated into a unitary matrix by increasing the dimension (blocked-out parts of the matrix). **c**, Experimental results for the simulated evolution of the probability for a single excitation that is initially in one OH stretch mode (black points) to be found in the other stretch mode (grey points) and in the symmetric bend (blue points) under relaxation dynamics. Solid lines are theoretical curves. **d**, Spectrum of two excitations in bunched (black) and anti-bunched (blue) local stretch modes for a harmonic (dashed) and anharmonic (solid) model. **e**, The anharmonic evolution is characterized by anharmonic potentials for single oscillators (top inset, where R is the nuclear distance and $V(R)$ is the potential energy at R) and cross-mode coupling between oscillators (bottom inset). These are implemented via a measurement-induced nonlinearity using an ancillary photon and modes. **f**, Experimental results for the simulated evolution of the probability for two excitations that are initially bunched in local stretch modes to be found in the anti-bunched state (left) and the bunched state (right) under both models (dashed, harmonic; solid, anharmonic). All error bars represent 1-s.d. estimates from Poissonian statistics.

Anharmonic potentials in H_2O

Potential energy surfaces of real molecules are anharmonic, and we now consider simulations in this regime, depicted in Fig. 3d. In addition to the second derivative in the Taylor expansion of the potential energy surface, as per the harmonic approximation, we now include all third derivatives and the semi-diagonal quartic derivatives. Applying vibrational perturbation theory yields a new Hamiltonian:

$$\hat{H}_a = \hat{H} + \hbar \sum_{i \leq j} \frac{x_{ij}}{2} \sqrt{\omega_i \omega_j} (a_i^\dagger a_i + a_j^\dagger a_j + 2 a_i^\dagger a_j^\dagger a_i a_j)$$

where $\hat{H}$ is the harmonic Hamiltonian and x_{ij} are the perturbation-theory coefficients.

Implementing this Hamiltonian requires interactions between photons—a key challenge in quantum information processing. Demonstrations of enhanced single-photon interactions have required, for example, an artificial Kerr medium using superconducting circuits[44], fibre coupling a single atom and a microresonator[45], or coupling to a single quantum dot in a micropillar cavity[46]. Importantly, the interactions that are required to implement perturbative models such as $\hat{H}_a$ can be weaker than the fully entangling operations and controlled π phase gates that are used for universal quantum computing, with a potentially lower demand for reprogrammable nonlinear optics.

Here, instead, we demonstrate an approach based on measurement-induced nonlinearities, which are in principle scalable for all-linear-optical quantum computing but involve a large overhead. It is possible to implement a conditional π phase shift on a two-photon Fock state using an ancillary photon and additional optical modes[47]. Using newly derived nonlinear phase-shift gates, we are able to implement arbitrary phase shifts between the zero-, one- and two-photon Fock states of an optical mode.

We simulate and compare harmonic and anharmonic models of vibration for H_2O, restricting to the subspace of stretch modes. Two photons injected together into the top mode of the chip serves to simulate two excitations initialized in a superposition of the eigenstates of the harmonic model that correspond to a local OH stretch. As shown in Fig. 3e, when simulating the anharmonic model, this input state is understood as the same superposition of the new energy eigenstates of $\hat{H}_a$, while a third photon injected into the third optical mode serves as the ancillary system.

In Fig. 3f we show the results of simulating the probabilities for these two vibrational excitations to remain bunched or to anti-bunch, under harmonic ($\hat{H}$) and anharmonic ($\hat{H}_a$) models. The difference in the detection patterns between the two models is a function of their different spectra (Fig. 3d). The probability of detecting a single excitation in each of the modes (anti-bunched; Fig. 3f, left panel) acquires a simple frequency shift for the anharmonic evolution that corresponds to the

adjusted energy levels (Fig. 3d, top panel). By contrast, the probabilities for the state to remain doubly occupied display markedly different dynamics between the harmonic and anharmonic cases (Fig. 3f, right panel). This is a result of the three vibrational eigenstates no longer being equally spaced in energy (Fig. 3d, bottom panel), which introduces new frequencies in the evolution. For this set of experiments, the average distances between the ideal and experimental distributions for the harmonic and anharmonic cases are 0.02 ± 0.01 and 0.06 ± 0.02, respectively.

Quantum simulation with adaptive feedback

Adaptive feedback control (AFC) is a practical laboratory technique for finding optimal control fields for molecules[9]. AFC naturally incorporates laboratory constraints to design control fields that would not be found either analytically or through numerical simulation. Nevertheless, models idealized for quantum simulation could help to identify new possibilities for molecular control, could enable their comparison over a large number of molecules and could include quantum control fields.

Our goal is to use our simulator with an adaptive feedback loop from its quantum measurement statistics to design initial quantum states for a molecule that maximally achieve a particular task over a period of evolution. Our example molecule is ammonia (NH_3), a prototype for studying dissociation, including vibrationally mediated pathways, in which the states of its products ($NH_2 + H$) depend on the prior vibrational state in the ground electronic state[10].

Our model (Fig. 4b) simulates the preparation of a vibrational state in the electronic ground state of the molecule. We then obtain the vibrational state that results from an electronic excitation by projecting the vibrational modes of the ground state onto the vibrational modes of the excited state. We approximate this projection by a unitary transformation between the modes U_{GE}; however, this transformation can in general be achieved via single-mode squeezing, displacement and linear optical transformations[48]. The evolution of the vibrational state of the electronically excited molecule is simulated under the harmonic Hamiltonian for the normal modes. By measuring the evolved state in a localized basis we identify three local NH stretch modes.

The aim of this simulation, depicted in Fig. 4c, is to let an AFC algorithm find the initial states of two vibrational excitations (in the molecule in the electronic ground state) that result in a maximal total probability of bunching in any of the three NH stretch modes (of the electronically excited molecule) over the first 10 fs of evolution, which we associate with a preferred dissociation pathway, while suppressing other bunched events, which we associate with other pathways. The algorithm begins with a trial state of two photons that simulates two excitations superposed randomly over five of the normal vibrational modes. State preparation, which is parameterized by the vector $\boldsymbol{\theta}$, is optimized iteratively by programming the simulator to implement $U(\boldsymbol{\theta}, t_i) = U_L \exp(-iHt_i/\hbar) U_{GE}^{\dagger} U(\boldsymbol{\theta})$, where U_{GE} relates to the transformation between the ground- and excited-state normal modes and U_L relates to the transformation between the excited-state normal and local modes.

An example experimental trial is shown in Fig. 4d. We used a Nelder–Mead simplex method to minimize the cost function

$$C = -\alpha \sum_i w_i \Delta p_i \in [-1, 1]$$

where Δp_i is the difference between the probability of bunching in the NH stretch modes and the remaining modes at time step i, w_i are weighting factors and α is a normalization factor. The final value in Fig. 4d is $C = -0.771$, starting from a random initial state with $C = +0.337$. We repeated this experiment with six random initial states;

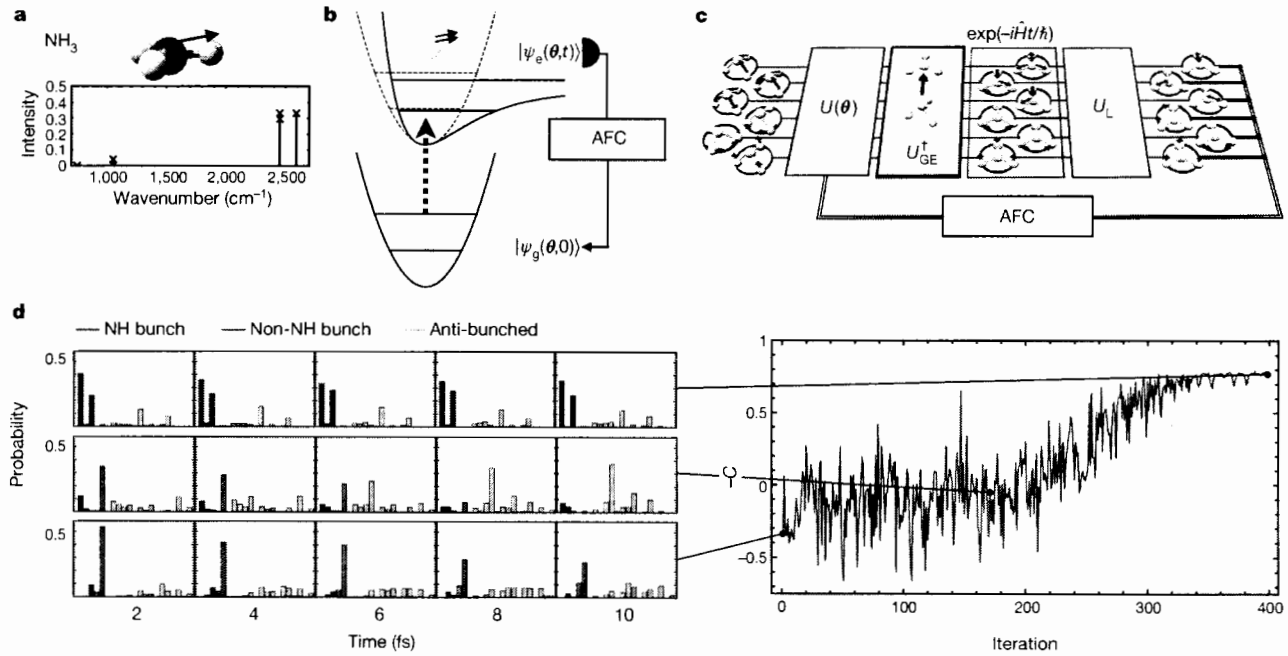

Fig. 4 | AFC algorithm for a dissociation pathway in NH_3. a, The spectral decomposition of an NH stretch mode in the electronic excited state of NH_3. **b**, A two-excitation vibrational state, parameterized by $\boldsymbol{\theta}$, is initialized in the ground-state vibrational modes ($|\psi_g(\boldsymbol{\theta}, 0)\rangle$) of NH_3. The electronic state ($|\psi_e(\boldsymbol{\theta}, t)\rangle$) is excited and the localization of vibrational energy is measured over time. These measurements are used to feedback to the state preparation to increase energy localization in NH stretch modes, promoting a particular dissociation pathway for this molecule **c**, This scenario is simulated via a parameterized unitary for state preparation $U(\boldsymbol{\theta})$, a transformation between the ground-state and excited-state modes $U_{GE}^{\dagger}$, evolution under the excited-state modes ($\exp(-i\hat{H}t/\hbar)$) and measurement in a localized basis via U_L. The resulting photon statistics are fed back through an AFC algorithm to set $\boldsymbol{\theta}$ for the next iteration (after calculating the cost function C). **d**, The left panel displays an example set of experimental results that show the full distributions for bunching in the NH stretcb modes (red), bunching in the remaining three localized modes (blue) and detection in anti-bunched patterns (yellow) for five time steps at iteration numbers 1 (bottom), 175 (middle) and 399 (top). The right panel shows $-C$ measured at every iteration.

all resulted in similar final values of the cost function, with a mean of $\overline{C} = -0.845$.

Discussion

We have introduced photonics as a platform for simulating the vibrational quantum dynamics of molecules within the harmonic, perturbatively anharmonic and Linblad models, with a photonic chip playing the part of a programmable molecule. Scaling up and extending these techniques to more involved Hamiltonians with highly anharmonic atomic potentials and electronic degrees of freedom, and to realize an advantage over classical simulation techniques[36], presents important and interesting research directions.

Device errors that must be addressed include inevitable flaws in circuit fabrication and operation, photon distinguishability and pho-ton loss. Although the precision that is required in the setting of any individual circuit parameter increases with dimension[49], linear optical elements with extinction of more than 60 dB have been demonstrated[29]. Indistinguishability, or visibilities, between independent photons have been reported at 95% for on-chip sources[32] and at more than 90% for time bins of a solid-state photon source[34]. Although ultralow-loss integrated circuitry has been demonstrated[50], photon loss is a funda-mental error in photonics; basic methods that alleviate some of this error would provide substantial improvements in rates for the class of experiments demonstrated here. The development of programmable nonlinear optics at the quantum level is a key functionality for quantum technologies and remains an important challenge for the field. With modest progress in these areas, our approach could yield an early class of practical quantum simulations that operate beyond current classical limits.

Received: 11 October 2017; Accepted: 21 March 2018;
Published online 30 May 2018.

1. Gatti, F. *Molecular Quantum Dynamics*. (Springer, Berlin, 2014).
2. Brif, C., Chakrabarti, R. & Rabitz, H. Control of quantum phenomena: past, present and future. *New J. Phys.* **12**, 075008 (2010).
3. Feynman, R. P. Simulating physics with computers. *Int. J. Theor. Phys.* **21**, 467–488 (1982).
4. Lloyd, S. Universal quantum simulators. *Science* **273**, 1073–1078 (1996).
5. Aspuru-Guzik, A. & Walther, P. Photonic quantum simulators. *Nat. Phys.* **8**, 285–291 (2012).
6. Georgescu, I. M., Ashhab, S. & Nori, F. Quantum simulation. *Rev. Mod. Phys.* **86**, 153–185 (2014).
7. Shi, S., Woody, A. & Rabitz, H. Optimal control of selective vibrational excitation in harmonic linear chain molecules. *J. Chem. Phys.* **88**, 6870–6883 (1988).
8. Shapiro, M. & Brumer, P. Coherent control of molecular dynamics. *Rep. Prog. Phys.* **66**, 859–942 (2003).
9. Assion, A. et al. Control of chemical reactions by feedback-optimized phase-shaped femtosecond laser pulses. *Science* **282**, 919–922 (1998).
10. Hause, M. L., Yoon, Y. H. & Crim, F. F. Vibrationally mediated photodissociation of ammonia: the influence of NH stretching vibrations on passage through conical intersections. *J. Chem. Phys.* **125**, 174309 (2006).
11. Brinks, D. et al. Visualizing and controlling vibrational wave packets of single molecules. *Nature* **465**, 905–908 (2010).
12. Alnaser, A. et al. Subfemtosecond steering of hydrocarbon deprotonation through superposition of vibrational modes. *Nat Commun.* **5**, 3800 (2014).
13. Tong, X., Winney, A. H. & Willitsch, S. Sympathetic cooling of molecular ions in selected rotational and vibrational states produced by threshold photoionization. *Phys. Rev. Lett.* **105**, 143001 (2010).
14. Wolter, B. et al. Ultrafast electron diffraction imaging of bond breaking in di-ionized acetylene. *Science* **354**, 308–312 (2016).
15. Clark, J. B., Lecocq, F., Simmonds, R. W., Aumentado, J. & Teufel, J. D. Sideband cooling beyond the quantum backaction limit with squeezed light. *Nature* **541**, 191–195 (2017).
16. Dorfman, K. E., Schlawin, F. & Mukamel, S. Nonlinear optical signals and spectroscopy with quantum light. *Rev. Mod. Phys.* **88**, 045008 (2016).
17. Karpiński, M., Jachura, M., Wright, L. J. & Smith, B. J. Bandwidth manipulation of quantum light by an electro-optic time lens. *Nat. Photon.* **11**, 53–57 (2017).
18. Aaronson, S. & Arkhipov, A. The computational complexity of linear optics. *Theor. Comput.* **9**, 143–252 (2013).
19. Berry, D. W., Childs, A. M., Cleve, R., Kothari, R. & Somma, R. D. Simulating Hamiltonian dynamics with a truncated Taylor series. *Phys. Rev. Lett.* **114**, 090502 (2015).
20. Lanyon, B. P. et al. Universal digital quantum simulation with trapped ions. *Science* **334**, 57–61 (2011).
21. Kassal, I., Jordan, S. P., Love, P. J., Mohseni, M. & Aspuru-Guzik, A. Polynomial-time quantum algorithm for the simulation of chemical dynamics. *Proc. Natl Acad. Sci. USA* **105**, 18681–18686 (2008).
22. Lidar, D. A. & Wang, H. Calculating the thermal rate constant with exponential speedup on a quantum computer. *Phys. Rev. E* **59**, 2429–2438 (1999).
23. Campbell, E. T., Terhal, B. M. & Vuillot, C. Roads towards fault-tolerant universal quantum computation. *Nature* **549**, 172–179 (2017).
24. Wecker, D., Bauer, B., Clark, B. K., Hastings, M. B. & Troyer, M. Gate-count estimates for performing quantum chemistry on small quantum computers. *Phys. Rev. A* **90**, 022305 (2014).
25. Peruzzo, A. et al. A variational eigenvalue solver on a photonic quantum processor. *Nat. Commun.* **5**, 4213 (2014).
26. Kandala, A. et al. Hardware-efficient variational quantum eigensolver for small molecules and quantum magnets. *Nature* **549**, 242–246 (2017).
27. Politi, A., Cryan, M. J., Rarity, J. G., Yu, S. & O'Brien, J. L. Silica-on-silicon waveguide quantum circuits. *Science* **320**, 646–649 (2008).
28. Crespi, A. et al. Integrated photonic quantum gates for polarization qubits. *Nat. Commun.* **2**, 566 (2011).
29. Harris, N. C. et al. Quantum transport simulations in a programmable nanophotonic processor. *Nat. Photon.* **11**, 447–452 (2017).
30. Carolan, J. et al. Universal linear optics. *Science* **349**, 711–716 (2015).
31. Silverstone, J. W. et al. On-chip quantum interference between silicon photon-pair sources. *Nat. Photon.* **8**, 104–108 (2014).
32. Spring, J. B. et al. Chip-based array of near-identical, pure, heralded single-photon sources. *Optica* **4**, 90–96 (2017).
33. Najafi, F. et al. On-chip detection of non-classical light by scalable integration of single-photon detectors. *Nat. Commun.* **6**, 5873 (2015).
34. Wang, H. et al. Near-transform-limited single photons from an efficient solid-state quantum emitter. *Phys. Rev. Lett.* **116**, 213601 (2016).
35. Marsili, F. et al. Detecting single infrared photons with 93% system efficiency. *Nat. Photon.* **7**, 210–214 (2013).
36. Neville, A. et al. Classical boson sampling algorithms with superior performance to near-term experiments. *Nat. Phys.* **13**, 1153–1157 (2017).
37. Cubitt, T., Montanaro, A. & Piddock, S. Universal quantum Hamiltonians. Preprint at https://arxiv.org/abs/1701.05182 (2017).
38. Leitner, D. M. Energy flow in proteins. *Annu. Rev. Phys. Chem.* **59**, 233–259 (2008).
39. Kobus, M., Nguyen, P. H. & Stock, G. Coherent vibrational energy transfer along a peptide helix. *J. Chem. Phys.* **134**, 124518 (2011).
40. Arkhipov, A. & Kuperberg, G. The bosonic birthday paradox. *Geometry Topology Monogr.* **18**, 1–7 (2012).
41. Lindner, J. et al. Vibrational relaxation of pure liquid water. *Chem. Phys. Lett.* **421**, 329–333 (2006).
42. Ramasesha, K., De Marco, L., Mandal, A. & Tokmakoff, A. Water vibrations have strongly mixed intra- and intermolecular character. *Nat. Chem.* **5**, 935–940 (2013).
43. Horn, R. A. & Johnson, C. R. *Topics in Matrix Analysis* 57–59 (Cambridge Univ. Press, Cambridge, 1991.
44. Kirchmair, G. et al. Observation of quantum state collapse and revival due to the single-photon Kerr effect. *Nature* **495**, 205–209 (2013).
45. Shomroni, I. et al. All-optical routing of single photons by a one-atom switch controlled by a single photon. *Science* **345**, 903–906 (2014).
46. De Santis, L. et al. A solid-state single-photon filter. *Nat. Nanotechnol.* **12**, 663–667 (2017).
47. Knill, E., Laflamme, R. & Milburn, G. A scheme for efficient quantum computation with linear optics. *Nature* **409**, 46–52 (2001).
48. Huh, J., Guerreschi, G. G., Peropadre, B., McClean, J. R. & Aspuru-Guzik, A. Boson sampling for molecular vibronic spectra. *Nat. Photon.* **9**, 615–620 (2015).
49. Russell, N. J., Chakhmakhchyan, L., O'Brien, J. L. & Laing, A. Direct dialling of Haar random unitary matrices. *New J. Phys.* **19**, 033007 (2017).
50. Lee, H., Chen, T., Li, J., Painter, O. & Vahala, K. J. Ultra-low-loss optical delay line on a silicon chip. *Nat. Commun.* **3**, 867 (2012).

LETTER

In an earlier experiment[12] using the original ALPHA apparatus[16], we demonstrated microwave-induced spin flips in trapped antihydrogen. The current work was carried out using the second-generation ALPHA-2 device (Fig. 1), operating at the CERN Antiproton Decelerator[17]. Unlike their matter counterparts, antihydrogen atoms must be synthesized[18] by merging cold plasmas of antiprotons and positrons in specially configured Penning–Malmberg traps. In the ALPHA-2 device, we typically mix 90,000 antiprotons, slowed and captured from the Antiproton Decelerator, with 1.6 million positrons from a Surko-type accumulator[19] to produce about 25,000 antihydrogen atoms. These numbers are monitored in daily baseline measurements that involve ejecting particles onto a multichannel plate detector.

Of the produced antihydrogen atoms, only a few will have low enough kinetic energies (0.54 K in temperature units) to be trapped in our superconducting, multipolar, magnetic-minimum trap. The current state-of-the-art is that about 20 atoms can be trapped from a single mixing sequence, and we have accumulated up to 74 atoms by repetitive mixing (M.A. *et al.*, submitted). A single mixing and capture sequence takes approximately 4 min, the bulk of which is used for preparation of plasmas of appropriate temperature, size and density (M.A. *et al.*, submitted). The actual mixing process takes less than 1 s. The trapped antimatter atoms can survive for at least 1,000 s in the cryo-pumped ultrahigh vacuum of ALPHA-2.

Referring to Fig. 1, the antiproton and positron plasmas are merged in the central Penning trap (yellow electrodes) to produce antihydrogen. An external solenoid magnet provides a uniform 1-T field for the Penning trap. The production region is near the centre of the magnetic-minimum trap, which comprises an octupole coil for transverse confinement of neutral anti-atoms and five short solenoids ('mirror coils') that can shape the axial trapping well. The trapping volume is cylindrical, with a diameter of 44.35 mm and length of 280 mm. For the current experiment, only the outer two mirror coils are used to create the axial well.

Antihydrogen atoms that leave the trap and annihilate on the electrodes of the Penning trap are registered by the ALPHA-2 annihilation detector[20]. This three-layer silicon vertex detector that surrounds the trapping volume (Fig. 1) determines the vertex position of the antiproton annihilation. The amount of trapped antihydrogen can be determined destructively at any time by intentionally ramping down the trapping magnets to release anti-atoms, while monitoring their annihilations. The dominant background in our experiment comes from cosmic rays, which trigger the detector at an average rate of $10.02 \pm 0.02\,s^{-1}$ (all errors herein are one standard deviation).

To distinguish antiproton annihilations from cosmic rays, we use extended versions of our previously developed methods of

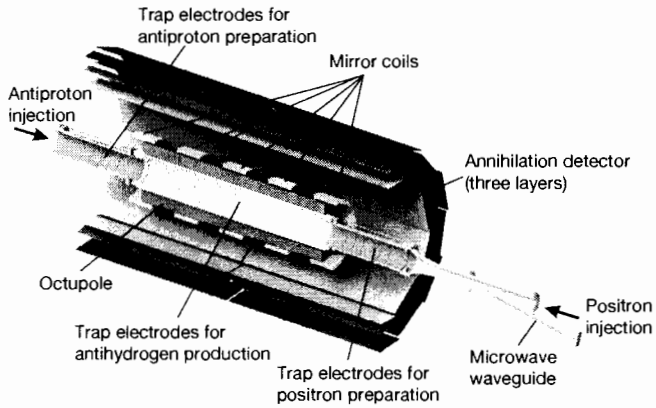

Figure 1 | The ALPHA-2 central apparatus. A cut-away schematic of the antihydrogen production and trapping region of ALPHA-2 is shown. For clarity, the vacuum wall and the cryostat for the superconducting magnets are not shown. Antiproton and positron plasmas are prepared on either side of the production region before being mixed to form antihydrogen at the centre of the minimum-B trap. All of the components shown are immersed in a uniform, 1-T, axial magnetic field, which is provided by an external solenoid (not illustrated).

multivariate analysis[12] (Methods). The multivariate analysis used for the current experiment yields a cosmic ray background rate of $0.00559 \pm 0.00051\ s^{-1}$ and an overall detection efficiency for annihilations of 0.596 ± 0.002.

Figure 2 depicts the expected energy levels of ground-state antihydrogen in a magnetic field $\boldsymbol{B}$. Atoms in either of the two levels labelled $|c\rangle$ and $|d\rangle$ have energies that increase with field strength B and can thus be trapped in a minimum-B configuration. The other two states, labelled $|a\rangle$ and $|b\rangle$, are expelled from the trap. The essential idea of the experiment is to use microwaves at about 29 GHz to resonantly drive transitions from trapped to un-trapped states as anti-atoms traverse the bottom of the magnetic potential well. At 1 T, the $|c\rangle \rightarrow |b\rangle$ and $|d\rangle \rightarrow |a\rangle$ transitions correspond to positron spin flips. Calculations for hydrogen (Fig. 3, inset) show that the inhomogeneous magnetic field produces asymmetric line shapes, with sharply defined onsets corresponding to the resonant frequency of either transition at the field minimum. The frequency difference between the two onsets represents the ground-state hyperfine splitting and is independent of the field strength and the number of anti-atoms that are trapped. It is this splitting that we seek to measure in antihydrogen and compare to that in hydrogen[9,10].

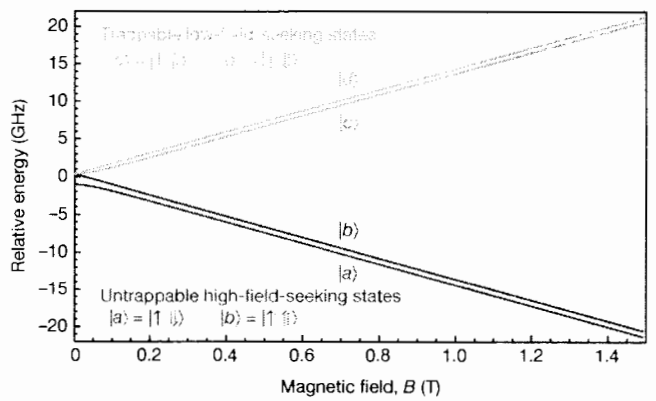

Figure 2 | Ground-state hyperfine energy levels. The energy levels are calculated assuming they are identical to those of hydrogen. The ket notation indicates the positron spin (left; ↓ or ↑) and antiproton spin (right; ⇓ or ⇑) states in the high-field limit. The shaded region illustrates part of the range of fields in the ALPHA-2 antihydrogen trap, with the minimum at 1.03 T. The full field map is shown in Fig. 3.

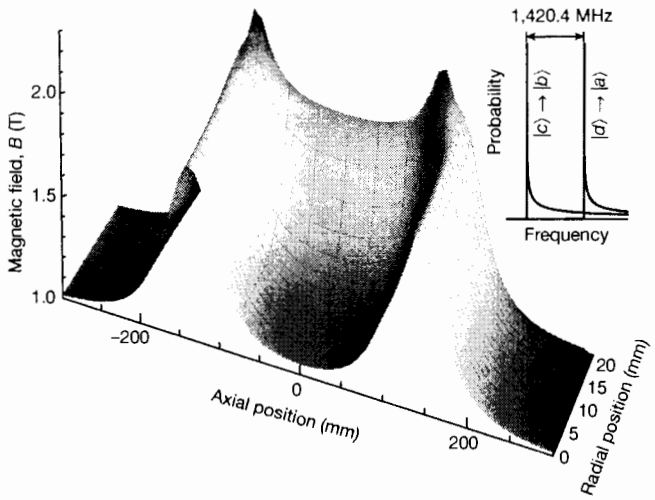

Figure 3 | Magnetic field strength. The scalar magnitude of the total magnetic field in the atom trap is plotted versus position. The radial position is measured from the symmetry axis of the trap, and the axial origin is the centre of the atom trap, defined by the outermost mirror coils. Inset, the probability of an atom being resonant at a given frequency, calculated for hydrogen; the two low-frequency onsets are separated by the ground-state splitting.

In Fig. 3 we show the magnetic field strength in ALPHA-2 as a function of position in the trapping volume. The volume of interest is at the centre of the trap, where fields, in the vicinity of the minimum, are about 1 T. Microwaves enter the apparatus through a purpose-built vacuum feed-through and are directed to the trapping volume using a waveguide (Fig. 1). We use an Agilent 8257D PSG frequency synthesizer and a Miteq AMF-4B amplifier to generate the microwave power. We injected 160 mW and 320 mW at the lower and upper transitions, respectively (see the discussion below); both are measured at the feed-through.

The experimental procedure involves producing and trapping antihydrogen atoms, removing any residual charged particles from the trap using pulsed electric fields, and then introducing microwaves into the trapping volume. The microwave frequency is stepped up in 300-kHz increments, starting from below the expected onset frequency of the $|c\rangle \rightarrow |b\rangle$ transition. The trapped antihydrogen atoms are exposed to microwave fields at each frequency for 4 s. After the first 16 steps, the starting frequency is incremented by +1,420.4 MHz and the process is repeated to scan through the onset of the $|d\rangle \rightarrow |a\rangle$ transition. The silicon vertex detector continuously monitors for the annihilation of antihydrogen atoms that are ejected following a resonant spin flip. The total illumination cycle is 2×64 s (16 points spanning the onset of each transition), after which the trap is de-energized in 1.5 s, releasing any remaining antihydrogen.

For the dataset presented here, we repeated this measurement sequence 22 times over a three-day period. A combination of single and double mixing sequences was used, achieving an average trapping rate of about 14 atoms per trial. Each day, before data acquisition, the external solenoid field was reset and the minimum field strength at the centre of the magnetic trap was determined by measuring the electron cyclotron resonance frequency of an electron plasma[21]. The precision of this measurement is estimated to be ±0.3 mT (equivalent to 8.4 MHz in electron cyclotron resonance frequency).

The results of the 22 measurement trials are plotted in Fig. 4. Cosmic background contributes 0.492 ± 0.045 events to each 4-s measurement bin. The sums of each day's trials are combined by aligning the maxima of the lower ($|c\rangle \rightarrow |b\rangle$) transition, to account for day-to-day variations in magnetic field. The responses observed should not be directly compared to traditional spectral lines or to the calculated distributions in the inset to Fig. 3, because the detailed shape is strongly influenced

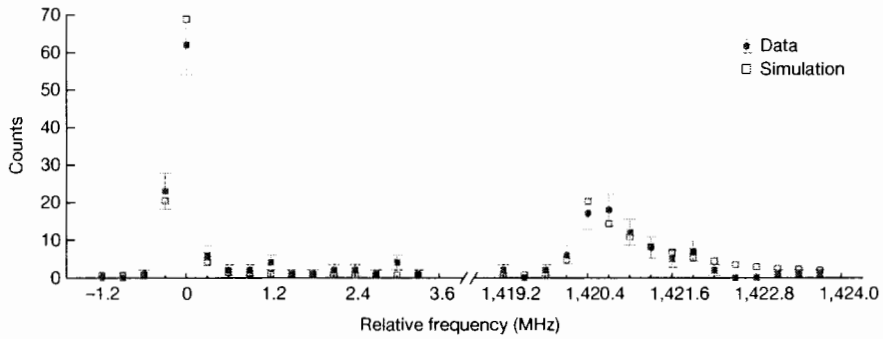

Figure 4 | Data and simulation. The number of detected antihydrogen annihilation events (filled blue squares), summed (see the text for details) over 22 trials, is plotted as a function of frequency. Note the discontinuous abscissa. The error bars represent counting statistics only. The expectations from the simulation for hydrogen in the trap are also shown (open red squares). The simulation results are scaled to match the total number (194) of observed events and are aligned to match the onset of the lower transition. The simulation includes the effect of measured fluctuations in the currents in the trapping magnets.

by the rate at which the trap is depopulated as atoms undergo spin-flip transitions.

Figure 4 reveals a qualitative difference between the shapes of the responses for the two transitions. The lower transition features a low-frequency onset and a narrow width; most of the anti-atoms are removed in the first two resonant bins. The more gradual onset and broader width of the upper transition are attributed to a lower amplitude of the *in situ* microwave magnetic field (see simulation results below). As illustrated in Fig. 1, the Penning-trap electrode stack in ALPHA-2 represents a complicated boundary surface for the injected electromagnetic radiation. It is unsurprising that disparate mixtures of standing and travelling waves are established at different frequencies. We can measure the strengths of the microwave electric fields in the vicinity of the two transitions by studying electron cyclotron resonance heating of electron plasmas stored in the trap centre[21]. These measurements lead to the conclusion that, for a given injected power, the microwave electric field strength at the centre of the trap is about seven times stronger at the lower transition frequency than at the higher one. However, we do not know the precise *in situ* relationship between the microwave electric and magnetic fields; and it is the latter that drives transitions between hyperfine levels. To partially compensate for this imbalance, we injected twice as much power at the upper transition, relative to the lower transition. This reduces the ratio of microwave-field amplitudes at the two transitions from seven to five. Our ability to further balance these amplitudes is currently limited by adverse thermal effects in the cryogenic, ultrahigh-vacuum environment.

Also shown in Fig. 4 are the results of a simulation (Methods) of the expected behaviour of hydrogen atoms in the magnetic environment of our trap. The inputs to this simulation include the trapping magnetic fields that are calculated from measured currents, the amplitudes of the microwave magnetic field that are inferred via electron cyclotron resonance and assuming plane-wave propagation in vacuum, the starting frequency for the microwave scan, the energy distribution of the trapped atoms, and the expected temporal magnetic field fluctuations, which are based on current-transformer monitoring of the currents in the trapping magnets. The simulation result is scaled to give the same total number of events as the experiment, integrated over both transitions (194 detected events). The simulation explicitly accounts for the removal of atoms from the trap as spin-flip events occur.

As described above, our experimental protocol was designed to determine the difference between the onset frequencies for the two transitions, profiting from the expected sharp increase in signal asso-ciated with resonance at the magnetic-field minimum. The slower increase that was observed in the $|d\rangle \rightarrow |a\rangle$ transition complicates the determination of the frequency splitting. It is tempting to extract a 'best' value for the hyperfine splitting by fitting the hydrogen simulation to the experimental data, particularly because the simulation reproduces the form of the data rather well. Given the fundamental nature of the quantity that is to be extracted, however, we defer any such interpretation until more detailed systematic studies can be performed.

We determine the splitting from Fig. 4 to be $1{,}420.4 \pm 0.5$ MHz, which reflects the difference between the low-frequency onsets of the two lines. The uncertainty includes contributions from drifts in the magnetic field that were observed during the scan (0.3 MHz), the procedure used for combining the data from separate days (0.3 MHz), and the determination of the onset frequencies of the two lines (0.3 MHz). This is the only available direct measurement of this fundamental quantity. The precision of our technique can be improved by reducing the step size in the frequency scan, by balancing the microwave power at the two transitions and by more precise characterization and stabilization of the magnetic fields in the atom trap. There are also plans to measure the same quantity in zero magnetic field using a beam of antihydrogen[22].

The release of the antihydrogen atoms that remain in the trap after the two transitions have been illuminated yielded 9 detected events for the 22 trials. A different multivariate analysis is used for this determination (Methods); the overall efficiency is 0.726 and we expect 1.3 total background events for the 22 trials. We conclude that about 96% of the trapped anti-atoms were removed as a result of a spin flip. Independent measurements using only the lower transition indicate that a microwave power sufficient to remove all of the trapped atoms with a 1-s time constant was injected without adverse thermal effects in the cryogenic, ultrahigh-vacuum system. In addition to being a useful diagnostic for optimizing antihydrogen trapping, the ability to selectively control the populations of the trapped quantum states will be useful for future microwave and optical spectroscopy of trapped antihydrogen.

The work described exemplifies a new approach in antimatter physics: the observation of spectral line shapes in antihydrogen. The ability to make a controlled frequency scan over an expected quantum mechanical transition in an atom of antimatter points the way to more precise tests of fundamental symmetries with antihydrogen. Charge–parity–time invariance implies that the detailed shapes—not just the resonance frequencies—of spectral lines for hydrogen and antihydrogen in the same environment must be identical. We will soon be able to use such precise measurements to subject antihydrogen to previously unobtainable scrutiny.

Also of interest is the nuclear magnetic resonance (NMR)-type transition between the $|c\rangle$ and $|d\rangle$ states, which corresponds to an antiproton spin flip. Recent advances in trapping efficiency (M.A. *et al.*, submitted) bode well for the feasibility of observing this transition in trapped antihydrogen. The absolute energy scales for the positron and antiproton spin-flip transitions in ALPHA-2 are respectively five and eight orders of magnitude smaller than that of the laser transition that was recently observed[15]. In addition to probing different interactions in the antihydrogen Hamiltonian, these energy scales offer very high sensitivity to potential new physics[23].

Online Content Methods, along with any additional Extended Data display items and Source Data, are available in the online version of the paper; references unique to these sections appear only in the online paper.

Received 27 May; accepted 30 June 2017.

1. Rabi, I. I., Kellogg, J. M. B. & Zacharias, J. R. The magnetic moment of the proton. *Phys. Rev.* **46,** 157–163 (1934).
2. Rabi, I. I., Kellogg, J. M. B. & Zacharias, J. R. The magnetic moment of the deuteron. *Phys. Rev.* **46,** 163–165 (1934).
3. Kellogg, J. M. B., Rabi, I. I. & Zacharias, J. R. The gyromagnetic properties of the hydrogens. *Phys. Rev.* **50,** 472–481 (1936).
4. Petit, P., Desaintfuscien, M. & Audoin, C. Temperature dependence of the hydrogen maser wall shift in the temperature range 295–395 K. *Metrologia* **16,** 7–14 (1980).
5. Nafe, J. E., Nelson, E. B. & Rabi, I. I. The hyperfine structure of atomic hydrogen and deuterium. *Phys. Rev.* **71,** 914–915 (1947).
6. Nafe, J. E. & Nelson, E. B. The hyperfine structure of hydrogen and deuterium. *Phys. Rev.* **73,** 718–728 (1948).
7. Nelson, E. B. & Nafe, J. E. The hyperfine structure of tritium. *Phys. Rev.* **75,** 1194–1198 (1949).
8. Nelson, E. B. & Nafe, J. E. A comparison of the *g* value of the electron in hydrogen with that in deuterium. *Phys. Rev.* **76,** 1858–1860 (1949).
9. Schwinger, J. On quantum-electrodynamics and the magnetic moment of the electron. *Phys. Rev.* **73,** 416–417 (1948).
10. Schwinger, J. Quantum electrodynamics. III. The electromagnetic properties of the electron—radiative corrections to scattering. *Phys. Rev.* **76,** 790–817 (1949).
11. Goldenberg, H. M., Kleppner, D. & Ramsey, N. F. Atomic hydrogen maser. *Phys. Rev. Lett.* **5,** 361–362 (1960).
12. Amole, C. *et al.* Resonant quantum transitions in trapped antihydrogen atoms. *Nature* **483,** 439–443 (2012).
13. Andresen, G. B. *et al.* Trapped antihydrogen. *Nature* **468,** 673–676 (2010).
14. Andresen, G. B. *et al.* Confinement of antihydrogen for 1,000 seconds. *Nat. Phys.* **7,** 558–564 (2011).
15. Ahmadi, M. *et al.* Observation of the 1S–2S transition in trapped antihydrogen. *Nature* **541,** 506–510 (2017).
16. Amole, C. *et al.* The ALPHA antihydrogen trapping apparatus. *Nucl. Instrum. Methods A* **735,** 319–340 (2014).
17. Maury, S. The antiproton decelerator: AD. *Hyperfine Interact.* **109,** 43–52 (1997).
18. Amoretti, M. *et al.* Production and detection of cold antihydrogen atoms. *Nature* **419,** 456–459 (2002).
19. Murphy, T. J. & Surko, C. M. Positron trapping in an electrostatic well by inelastic collisions with nitrogen molecules. *Phys. Rev. A* **46,** 5696–5705 (1992).
20. Amole, C. *et al.* Silicon vertex detector upgrade in the ALPHA experiment. *Nucl. Instrum. Methods A* **732,** 134–136 (2013).
21. Amole, C. *et al. In situ* electromagnetic field diagnostics with an electron plasma in a Penning–Malmberg trap. *New J. Phys.* **16,** 013037 (2014).
22. Kuroda, N. *et al.* A source of antihydrogen for in-flight hyperfine spectroscopy. *Nat. Commun.* **5,** 3089 (2014).
23. Kostelecký, V. A. & Vargas, A. J. Lorentz and CPT tests with hydrogen, antihydrogen, and related systems. *Phys. Rev. D* **92,** 056002 (2015).

METHODS

Simulation of the microwave–atom interaction. Our simulation of the microwave flip process uses quantum and classical ideas. The motion of antihydrogen through the trap is determined by solving the classical equations of motion using a fourth-order symplectic integrator. The force on the atom arises from the spatially dependent magnetic field. Because the magnetic fields are always large, the state of the antihydrogen is conserved unless the resonance condition is satisfied. While trapped, the atoms are in either the $|c\rangle$ or $|d\rangle$ states (the low-field-seeking states). These states have a magnetic moment that is approximately equal to that of the positron, which leads to a potential energy of $\mathrm{PE} \approx \mu B/2$, where $\mu = g\mu_B$. Here, μ_B is the Bohr magneton and g is the spin g-factor. The force is obtained by numerically computing the gradient of the magnitude of the magnetic field.

The energies of the hyperfine states are solved using an effective Hamiltonian with the hyperfine splitting and the magnetic moments of hydrogen as inputs. A quadratic interpolation of the energies at three consecutive time steps is used to determine whether the microwave resonance condition is met. Where in space this condition is met depends on the currents in the various magnets and on the microwave frequency. If the resonance condition occurs during the step, then the Landau–Zener approximation is used to obtain a spin-flip probability. The time derivative of the energy separation is calculated from the quadratic interpolation. The matrix element V that couples the $|c\rangle$ and $|b\rangle$ or $|d\rangle$ and $|a\rangle$ states depends on the microwave magnetic field B_{MW} perpendicular to the static magnetic field at the position at which the antihydrogen is in resonance; it is well approximated by $V = B_{MW}\mu/4$. To estimate B_{MW} we use the electron-cyclotron-resonance plasma-heating diagnostic discussed in the main text, which measures the microwave electric field E_{MW} perpendicular to the static magnetic field. We then assume B_{MW} is uniform and given by $B_{MW} = E_{MW}/c$, where c is the speed of light in vacuum. (The precise relationship between E_{MW} and B_{MW} is not known because the boundary conditions imposed by the electrode stack support a complex mixture of standing and travelling wave modes. Errors from making this assumption are reduced by averaging.)

Resonance conditions are encountered in pairs as atoms pass through the centre of the trap, and we account for the possibility that spins will flip more than once. Simulations do not predict a simple exponential decay of trapped populations when microwaves are present; the rate at which atoms encounter resonance conditions and the probability that they undergo a spin flip as they pass through resonance vary with trajectory. However, as an indication of scale, a microwave intensity of $4\,\mathrm{mW\,cm^{-2}}$ (corresponding to $B_{MW} = 0.6\,\mu\mathrm{T}$ and $V = h \times (4\,\mathrm{kHz})$, where h is Planck's constant) applied just above the onset of either transition will clear atoms in the corresponding state from the trap with a time constant of order 1 s.

Multivariate analysis of detector events. Differentiation of antihydrogen annihilations and background events (primarily cosmic rays) is achieved by discerning their distinctive topologies. A multivariate analysis package is used to distinguish between these two populations[24,25].

Two independent multivariate analyses were performed for this experiment: a low-background analysis for identifying annihilations during the 128-s microwave window and a high-signal-acceptance analysis to identify annihilations during the 1.5-s trap shutdown. The latter analysis has the same design as used in previous experiments[12,16]. The former analysis is modified to achieve a much lower background, through the addition of more variables that enhance the signal-to-background discrimination. The additional variables include: the asymmetry in hit count between the two hemispheres defined by the plane perpendicular to the event axis[12] and passing through the centre of the trap; the minimum distance of closest approach of any cosmic track candidate to the reconstructed vertex; the polar angle of the vector describing the vertex position[26] relative to the centre of the trap; and the average of the ratios between the axial and radial projections of the tracks that originate from the reconstructed vertex.

The signal and background data used for multivariate-analysis training, validation and testing (split equally) comprises a set of 305,706 annihilation events and 236,969 background events.

Data availability. The datasets generated and analysed during this study are available from corresponding author J.S.H. on reasonable request.

24. Narsky, I. StatPatternRecognition: a C++ package for statistical analysis of high energy physics data. Preprint at http://arxiv.org/abs/physics/0507143 (2005).
25. Narsky, I. Optimization of signal significance by bagging decision trees. Preprint at http://arxiv.org/abs/physics/0507157 (2005).
26. Amole, C. *et al.* Alternative method for reconstruction of antihydrogen annihilation vertices. *Hyperfine Interact.* **212,** 101–107 (2012).

Consiglio Nazionale delle Ricerche

TRACCE DELLE PROVE D'ESAME NON ESTRATTE

TRACCIA N.1 A CARATTERE GENERALE

Il candidato descriva una tematica di ricerca pertinente all'area strategica relativa al presente concorso e che ritiene di particolare interesse descrivendo lo stato dell'arte, le metodologie teoriche e/o sperimentali rilevanti e i problemi aperti in questo ambito e in particolare l'impatto che tale ricerca potrebbe produrre. Il testo deve essere redatto in lingua inglese. Il testo scritto non deve superare la lunghezza di due facciate di foglio protocollo.

The candidate should describe a research topic relevant to the strategic area related to this selection procedure, which he/she considers of particular interest, describing the state of the art, the relevant theoreticat and/or experìmental methodologies and the open problems in this field and in particular, the impact that such research could produce. The text must be written in English. The written text must not exceed the length of two pages.

TRACCIA N.3 A CARATTERE GENERALE

Il candidato descriva una tematica di ricerca pertinente all'area strategica relativa al presente concorso e che ritiene di particolare interesse descrivendo lo stato dell'arte, le metodologie teoriche e/o sperimentali rilevanti, l'impatto che tale ricerca potrebbe produrre e in particolare i problemi aperti in questo ambito. Il testo deve essere redatto in lingua inglese. Il testo scritto non deve superare la lunghezza di due facciate di foglio protocollo.

The candidate should describe a research topic relevant to the strategie area related to this selection procedure, which he/she considers of particular interest, describing the state of the art, the relevant theoretical and/or experimental methodologies, the impact that such research could produce and in particular, the open problems in this field. The text must be written in English. The written text must not exceed the length of two pages

TRACCIA N. "B" A CONTENUTO TEORICO-PRATICO

Il candidato scelga uno dei tre articoli proposti e rediga un abstract in inglese della lunghezza massima di 150 parole.

The candidate should choose one of the enclosed papers and write an abstract in English. The abstract must not exceed 150 words.

TRACCIA N. "C" A CONTENUTO TEORICO-PRATICO

Il candidato scelga uno dei tre articoli proposti e rediga un abstract in inglese della lunghezza massima di 150 parole.

The candidate should choose one of the enclosed papers and write an abstract in English. The abstract must not exceed 150 words.

nature physics

LETTERS

Spontaneous symmetry breaking occurs when an equilib-rium state exhibits a lower symmetry than the corresponding Hamiltonian describing the system. The system then spontane-ously picks one of the energetically degenerate choices of the order parameter and due to the specific energy landscape this process is accompanied by new collective modes. The typical picture, which exemplifies spontaneous symmetry breaking, uses a Mexican-hat-shaped energy potential (see Fig. 1a) that suggests the emergence of two distinct collective modes: the gapless 'Goldstone mode', which is associated with long-wavelength phase fluctuations of the order parameter, and an orthogonal gapped mode, the 'Higgs mode', which describes amplitude modulations of the order parameter. While Goldstone modes, such as phonons, appear necessarily when continuous symmetries are broken, stable Higgs modes are scarce, since decay channels might be present. The best-known example of a Higgs mode appears in the standard model of particle physics where this mode gives elementary particles their mass[1].

In the non-relativistic low-energy regime usually encountered in condensed-matter physics, the existence of a stable Higgs mode cannot be taken for granted[2]. However, under certain conditions, other symmetries, such as particle–hole symmetry, can play the role of Lorentz invariance and induce a stable Higgs mode. A notable example of a low-energy particle–hole symmetric theory hosting a stable Higgs mode is the famous Bardeen–Cooper–Schrieffer (BCS) Hamiltonian describing weakly interacting superconductors[3,12]. Evidence for the Higgs mode has been found in conventional BCS superconductors[3–5]. However, experimental detections have been solely indirect as the Higgs mode does not couple directly to electromagnetic fields owing to the gauge invariance required for its existence. The far-reaching importance of the Higgs mode is further illustrated by its observation in a variety of specially tuned systems such as antiferromagnets[13], liquid ^{3}He (ref. [14]), ultracold bosonic atoms near the superfluid/Mott-insulator transition[15,16], spinor Bose gases[17] and Bose gases strongly coupled to optical fields[18]. In contrast, weakly interacting Bose–Einstein condensates (BECs) do not exhibit a stable Higgs mode[6,10,11].

In recent years, research has focused on advanced materials exhibiting superconductivity far beyond the conventional BCS description, such as cuprates, pnictides and the unitary Fermi gas. Many of these materials are characterized by strong fermionic correlations. Even though in this context the existence of a Higgs mode has been the topic of theoretical debates[7–11], experimental evidence for the Higgs mode in systems exhibiting strong correlations between fermions is still absent.

Here, we spectroscopically excite the Higgs mode in a superfluid Fermi gas in the crossover between a weakly interacting BCS superfluid and a BEC of strongly coupled dimers (Fig. 1). We induce a periodic modulation of the amplitude of the superconducting order parameter Δ and find an excitation resonance near twice the superconducting gap value. On the BCS side, the spectroscopic feature agrees with the theoretical expectation of the Higgs mode. On the BEC side of the crossover, we find strong broadening beyond the predictions of BCS theory and, eventually, the disappearance of the mode as predicted for a weakly interacting BEC[6,10,11].

Our measurements are conducted in an ultracold quantum gas of $\sim 4\times10^5$ ^{6}Li atoms prepared in a balanced mixture of the two lowest hyperfine states $|1\rangle$ and $|2\rangle$ of the electronic ground state. The gas is trapped in a harmonic potential with frequencies of $(\omega_x, \omega_y, \omega_z) = 2\pi\times(91, 151, 235)$ Hz and is subjected to a homogeneous magnetic field, which is varied in the range of 740–1,000 G to tune the s-wave scattering length a near the Feshbach resonance located at 834 G. This results in an adjustment of the interaction parameter of the gas in the range of $-0.8 \lesssim 1/(k_F a) \lesssim 1$, (that is, across the whole BCS/BEC crossover). The Fermi energy in the centre of the gas is $E_F \simeq h\times(34\pm3)$ kHz at each of the considered interaction strengths and sets the Fermi wavevector $k_F = \sqrt{8\pi^2 m E_F / h^2}$, where m denotes the mass of the atom and h is Planck's constant.

Excitation of the Higgs mode requires a scheme that couples to the amplitude of the order parameter rather than creating phase fluctuations or strong single-particle excitations. Previous theoretical proposals[6,19,20] for exciting the Higgs mode in ultracold Fermi gases have focused on a modulation of the interaction parameter

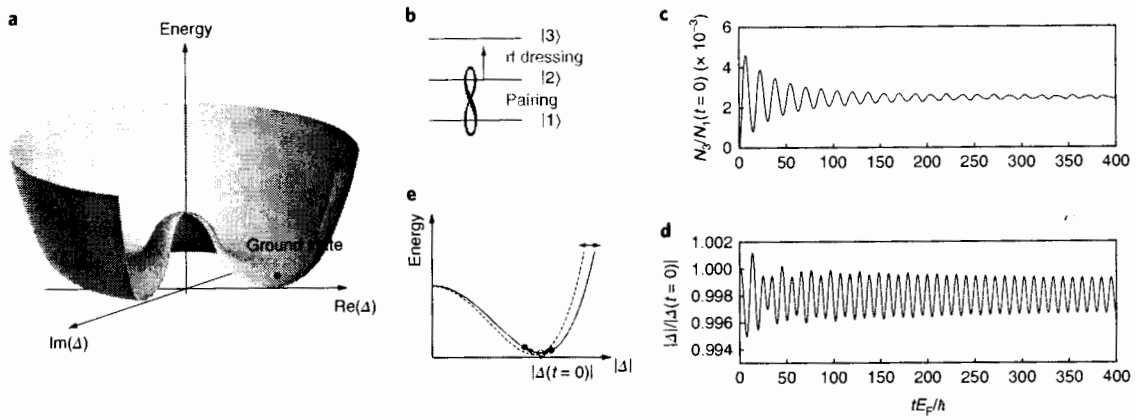

Fig. 1 | Principle of the Higgs mode excitation. a, Mexican hat potential of the free energy as a function of the real and imaginary parts of the complex order parameter Δ. The equilibrium state order parameter takes spontaneously one of the values at the energy minima. **b**, We employ rf dressing of the paired superfluid by off-resonant coupling to an unoccupied state $|3\rangle$. **c**,**d**, This results in a periodic modulation of both the occupation of the state $|3\rangle$ (**c**) and the superconducting gap (**d**). Here, N_3 is the number of atoms in state $|3\rangle$ and N_1 ($t=0$) is the initial number of atoms in state $|1\rangle$. Shown are numerical simulations for a coupling constant $1/(k_F a) = -0.6704$, $\hbar\Omega_R = 0.0353E_F$ and $\hbar\delta = -0.3247E_F$. **e**, By adjusting the modulation frequency, we achieve an excitation of the Higgs mode in the Mexican hat.

$1/(k_F a)$; however, experimentally only single-particle excitations have been observed from such a modulation[21]. We have developed a novel excitation scheme employing a radiofrequency (rf) field, dressing the state $|2\rangle$ with the initially unoccupied hyperfine state $|3\rangle$ thereby modulating the pairing between the $|1\rangle$ and $|2\rangle$ states (see Fig. 1b,c). Previous experiments investigating ultracold gases with rf spectroscopy[22–25] have focused on studying single-particle excitations. To this end, there, the duration of the rf pulse τ had been chosen shorter than the inverse of the Rabi frequency Ω_R, such that the spectra could be interpreted in the weak-excitation limit using Fermi's golden rule. In contrast, here, we employ an rf drive far red-detuned from single-particle resonances in the interacting many-body system and in the long-pulse limit $\Omega_R\tau \gg 1$, to couple to the amplitude of the order parameter. To illustrate this, consider first an isolated two-level system of the $|2\rangle$ and the $|3\rangle$ state coupled by a Rabi frequency Ω_R with detuning δ from the resonance. The occupation probability of the atoms in the $|2\rangle$ state is $p_2 = 1 - \Omega_R^2/\Omega_R'^2 \sin^2(\Omega_R' t/2)$; that is, the continuous rf dressing leads to a time-periodic modulation of the occupation of the $|2\rangle$-state with the effective Rabi frequency $\Omega_R' = \sqrt{\Omega_R^2 + \delta^2}$.

In the many-body problem of the BCS/BEC crossover, the situation is complicated by the dispersion of the (quasi) particles and the presence of interactions. In particular, a continuum of excitations typically occurs above the energy of the lowest single-particle excitation to state $|3\rangle$ (see Fig. 2a). Deep in the BCS regime, the continuum of excitations is related to the different momentum states and the excitation scheme can be approximated by coupling each occupied momentum state of the BCS quasiparticles in level $|2\rangle$ to the corresponding momentum state in state $|3\rangle$ since the rf dressing transfers negligible momentum. The effective Rabi frequency $\Omega_{R,k}' = \sqrt{\Omega_R^2 + \delta_k^2}$ and therefore the excitation probability becomes momentum dependent by the many-body detuning $\hbar\delta_k = \hbar\delta - E_k - \xi_k$, where ξ_k is the single-particle dispersion, and $E_k = \sqrt{\xi_k^2 + |\Delta|^2}$ is the quasiparticle dispersion and Δ is the s-wave superconducting order parameter. A red-detuned rf drive, as employed here, avoids resonant coupling to the single-particle excitations, however, still modulates off-resonantly the occupation of the excited states as shown in Fig. 2b.

The off-resonant periodic modulation of the occupation of the state $|2\rangle$ with controllable frequency $\Omega_{R,k}'$ induces a modulation of the amplitude of the order parameter $|\Delta|$ (Fig. 1d,e, for details see Methods) and hence couples directly to the Higgs mode. To illustrate this mechanism, we numerically solve the minimal set of coupled equations of motion describing the evolution of the order parameter in the presence of an rf coupling to state $|3\rangle$ (see Methods and Supplementary Information). We see that the Fourier spectrum of $|\Delta|$ for one modulation frequency displays—aside from a response corresponding to the modulation frequencies $\Omega_{R,k}'$—a sharp peak at the gap value $2|\Delta|$ (see Fig. 2c inset). By the momentum-resolved representation (Fig. 2c), we identify this peak to be dominated by the Higgs excitation with a momentum-independent dispersion. The amplitude of the Higgs peak is maximal when the averaged effective drive frequency $\hbar\overline{\Omega}_{mod} \approx 2|\Delta|$ in accordance with its expected frequency. The Higgs mode is a collective mode of the system and even for the harmonically trapped gas exhibits a unique frequency. Numerical studies in the BCS limit have shown that in harmonically trapped systems, the Higgs mode should occur at the frequency of twice the superconducting gap evaluated at the maximum density of the gas[8,26–29] and hence we use this as our reference for the value of the gap to compare with theory and other experiments.

In the experiment, we search for the Higgs mode by measuring the energy absorption spectrum of the fermionic superfluid in the $|1,2\rangle$ states for different interactions. Using Ω_R and δ as adjustable parameters, we dress the $|2\rangle$ state by the $|3\rangle$ state with adjustable modulation frequency given by the effective Rabi frequency. We choose a drive frequency in the single-particle excitation gap. For our experiments, we measure the modulation frequency Ω_{mod} and amplitude α of the time-dependent population of the $|3\rangle$ state (for calibration, see Methods and Supplementary Information). We then use a constant excitation amplitude $p_{|3\rangle} \simeq 0.5\%$ and apply the modulation for a fixed period of 30 ms. After the excitation, we conduct a rapid magnetic field sweep onto the molecular side of the Feshbach resonance and convert Cooper pairs into dimers and measure the condensate fraction of the molecular condensate in time-of-flight imaging. The change in the condensate fraction provides us with a sensitive measure of the excitation of modes in the quantum gas. In Fig. 3a, we plot the measured spectra as a function of the modulation frequency for different values of $1/(k_F a)$. On the BCS side of the Feshbach resonance up to unitarity, $1/(k_F a) < 0$, we observe clear resonances for which the condensate fraction reduces, signalling the excitation of a well-defined mode. For $1/(k_F a) > 0$, the energy absorption peak is gradually washed out and broadens significantly. Far on the BEC side, for $1/(k_F a) \simeq 1$,

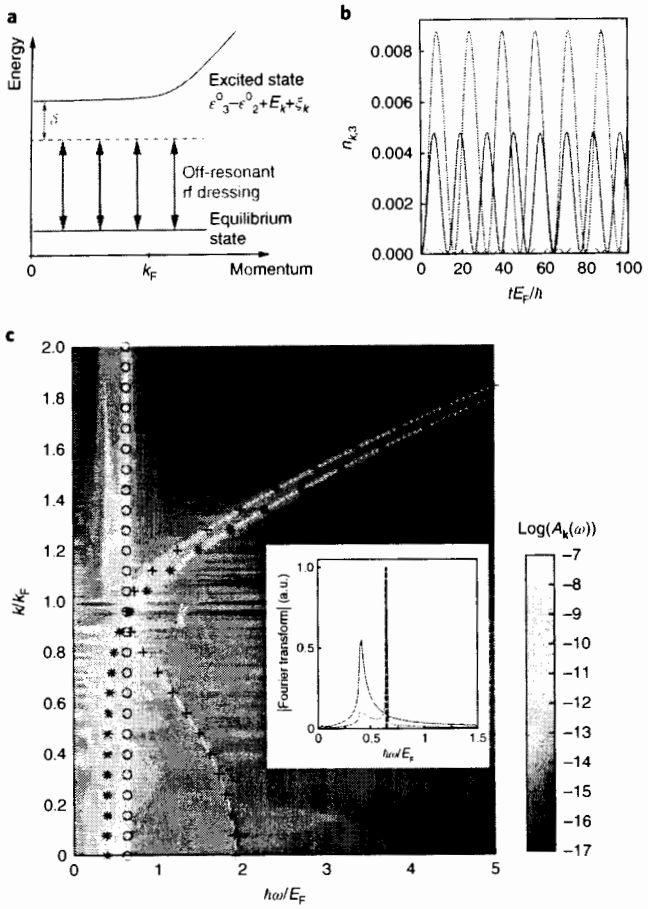

Fig. 2 | Illustration of the excitation scheme for one modulation frequency. **a**, The rf field is red-detuned from the single-particle excitation of the interacting system. It creates an off-resonant excitation to the state $|3\rangle$ with a varying detuning for different momenta. **b**, Time evolution of the momentum-resolved occupation of the $|3\rangle$ state with momentum $\mathbf{k}$ for a fixed value of $\frac{1}{k_F a}=-0.63$, a Rabi frequency $\hbar\Omega_R=0.038E_F$ and a detuning $\hbar\delta=-0.34E_F$. Blue: $k/k_F=0$, red: $k/k_F=0.8$, green: $k/k_F=1.1$. **c**, Spectral weight of the momentum-resolved gap $A_k(\omega)$ (see Methods). The circles indicate the Higgs mode, the stars mark the response to the modulation frequency and the crosses indicate the quasiparticle excitations at $2E_k$. The position of the star at $k=0$ approximately represents the effective modulation frequency for the chosen parameters. Inset: Fourier spectra (momentum integrated) of the occupation of the $|3\rangle$ state (red) and $|\Delta|$ (blue). The dashed line is the expected location of the Higgs mode at $2|\Delta|$. Panels **b**, **c** and the inset of **c** are for the same driving and detuning parameters.

we cannot observe a resonance and conclude that the Higgs mode is absent. The resonances generally exhibit an asymmetric line shape, which we fit with a Gaussian to the high-frequency side to extract the peak position and width. A contribution to the asymmetric peak shape stems from the momentum-dependence of the effective Rabi frequencies $\Omega'_{R,k}$. As indicated in Fig. 2a,b, the effective detuning (and hence the modulation frequency) varies with increasing momentum k. Therefore, a resonant excitation at the Higgs mode frequency can be achieved for high momenta k even though for low momenta the modulation frequency is below the resonant excitation.

To demonstrate the collective-mode nature of our resonance, we perform a number of checks. First, we verify that the excitation resonance frequency (to within 4%) and shape is independent of the modulation strength in the range of $0.001<\alpha<0.2$ and modulation duration between $\tau=0.5$ ms and $\tau=30$ ms (for the definition of α, see Methods and Supplementary Information). Second, we have confirmed that the observed resonance peak is not caused by single-particle excitations by measuring the excitation probability to the $|3\rangle$ state versus modulation frequency Ω_{mod} and finding a featureless broad spectrum. This and the following checks have been performed with a modulation amplitude of $\alpha=0.2$ and a modulation time of 0.5 ms, which is much shorter than the trap period of ~5 ms. Hence, the measurement is insensitive to thermalization effects and/or density redistribution within the cloud. Third, we check the momentum-dependence of the resonance. After the modulation, we perform a time-of-flight expansion for a period of 15 ms, which is approximately a quarter period of the residual harmonic potential during ballistic expansion. This procedure maps the initial momentum states to positions in the absorption image[20]. We analyse the detected condensate density in momentum intervals of $0.02\,k_F$ and find that the excitation resonance is at the same frequency for all momentum intervals (see Fig. 3b,c). Finally, we have searched for possible quasiparticle excitations resulting from our interaction modulation by employing standard rf spectroscopy[21,25,31] after the interaction modulation. The spectra show only a very weak and broad background independent of the modulation frequency. This behaviour is not unexpected since the contribution of quasiparticle excitations is smeared out in the presence of a trap as we confirmed numerically using the local-density approximation.

In Fig. 4a, we plot the position of the fitted peak of the energy absorption spectra versus the interaction parameter $1/(k_F a)$ evaluated at the centre of the sample. It has been suggested[2] that the Higgs mode frequency is close to twice the superconducting gap in the BCS/BEC crossover and can therefore be used as an approximative measure of the gap. In the crossover regime, the exact value of $|\Delta|$ is yet unknown and both experiments and numerical calculations are challenging. We compare our data to gap measurements using different methods[31,32] and several numerical calculations[33–35]. As compared to the previous experimental results, our extracted value is larger. We note that previous gap measurements rely on fitting the onset of a spectral feature, whereas our method is based on fitting a Gaussian to a slightly skewed spectral feature, and both methodologies could be susceptible to small systematic uncertainties. An upper bound is provided by the theoretical result of mean-field theory (dashed line), which is known to overestimate the superconducting gap.

In Fig. 4b, we plot the full-width at half-maximum of the Gaussian fits to the energy absorption peaks. Utilizing the BCS model for the momentum-dependent excitation discussed above, we estimate the width of our excitation resonance to be of the order Δ (see Supplementary Information). Hence, we cannot directly interpret the linewidth of our spectra as the decay rate of the Higgs mode but only as a lower limit of the lifetime. On the BCS side of the resonance, we find good agreement with our model and towards the BEC side the measured width far exceeds the prediction, indicating that the Higgs mode becomes strongly broadened, for example, due to the violation of particle-hole symmetry resulting in a decay into Goldstone modes[9,10,14,39]. Extending, in the future, our novel experimental scheme with a better momentum resolution will provide a route to finally explore the decay mechanisms of the Higgs mode, the understanding of which is a cornerstone in both high-energy particle physics and condensed-matter physics.

Methods

Methods, including statements of data availability and any associated accession codes and references, are available at https://doi.org/10.1038/.

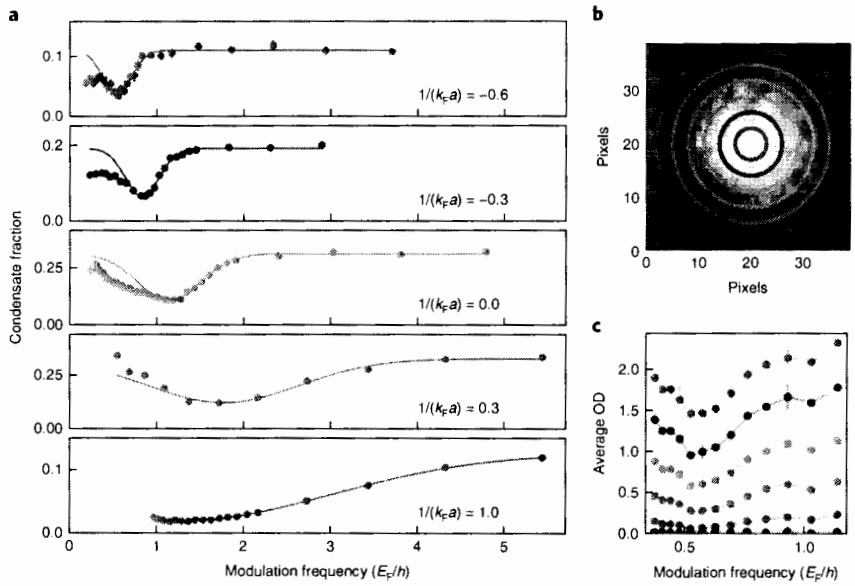

Fig. 3 | Excitation spectra of the Higgs mode. a, Excitation spectra of the Higgs mode for different interaction strengths, $1/(k_Fa)$, as labelled in the figure. The different levels of background condensate fraction are due to the different $1/(k_Fa)$. The solid lines shows the Gaussian fit to the high-frequency side of the spectra. The error bars show the standard deviation of approximately four measurements. **b**, Time-of-flight image of the condensate with the thermal background subtracted at $1/(k_Fa) \approx -0.43$. Rings indicate momentum intervals of $0.02k_F$. **c**, Momentum-resolved analysis of the Higgs excitation inside the condensate by averaging the optical density in the colour-coded rings in **b** for different modulation frequencies. The resonance occurs at the same modulation frequency for all momenta.

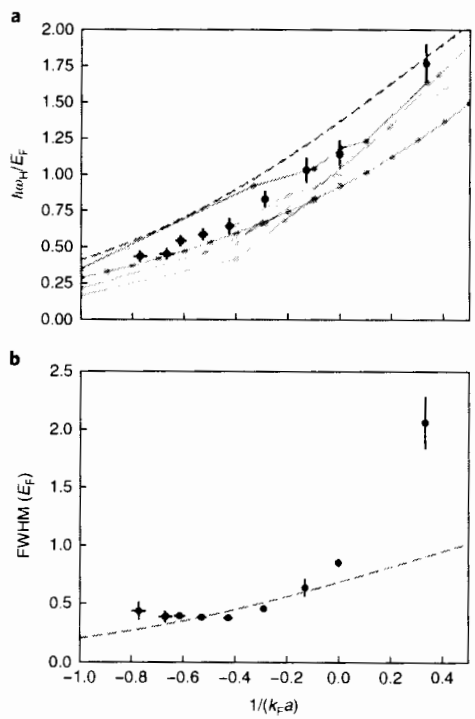

Fig. 4 | Observation of the Higgs mode. a, Measured peak positions of the energy absorption spectra (black circles). For comparison, we show numerical simulations of the gap parameter multiplied by 2: BCS mean-field theory (blue dashed line), ref. [ ] (red), ref. [ ] (green), ref. [ ] (orange), ref. [ ] (purple), ref. [ ] (brown), ref. [ ] (pink). The grey symbols show the experimental data of ref. [ ]. **b**, Measured full-width at half-maximum (FWHM) of the absorption peaks (black circles). For comparison, the BCS mean-field-theory gap is also shown (blue dashed line). The error bars in **a** and **b** represent the standard errors.

Received: 28 July 2017; Accepted: 26 March 2018;
Published online: 21 May 2018

References

1. Higgs, P. W. Broken symmetries and the masses of gauge bosons. *Phys. Rev. Lett.* **13**, 508–509 (1964).
2. Littlewood, P. B. & Varma, C. M. Gauge-invariant theory of the dynamical interaction of charge density waves and superconductivity. *Phys. Rev. Lett.* **47**, 811–814 (1981).
3. Sooryakumar, R. & Klein, M. V. Raman scattering by superconducting-gap excitations and their coupling to charge-density waves. *Phys. Rev. Lett.* **45**, 660–662 (1980).
4. Matsunaga, R. et al. Higgs amplitude mode in the BCS superconductors $Nb_{1-x}Ti_xN$ induced by terahertz pulse excitation. *Phys. Rev. Lett.* **111**, 057002 (2013).
5. Sherman, D. et al. The Higgs mode in disordered superconductors close to a quantum phase transition. *Nat. Phys.* **11**, 188–192 (2015).
6. Pekker, D. & Varma, C. Amplitude/Higgs modes in condensed matter physics. *Annu. Rev. Condens. Matter Phys.* **6**, 269–297 (2015).
7. Podolsky, D., Auerbach, A. & Arovas, D. P. Visibility of the amplitude (Higgs) mode in condensed matter. *Phys. Rev. B* **84**, 174522 (2011).
8. Scott, R. G., Dalfovo, F., Pitaevskii, L. P. & Stringari, S. Rapid ramps across the BEC–BCS crossover: A route to measuring the superfluid gap. *Phys. Rev. A.* **86**, 053604 (2012).
9. Barlas, Y. & Varma, C. M. Amplitude or Higgs modes in *d*-wave superconductors. *Phys. Rev. B* **87**, 054503 (2013).
10. Liu, B., Zhai, H. & Zhang, S. Evolution of the Higgs mode in a fermion superfluid with tunable interactions. *Phys. Rev. A* **93**, 033641 (2016).
11. Han, X., Liu, B. & Hu, J. Observability of Higgs mode in a system without Lorentz invariance. *Phys. Rev. A* **94**, 033608 (2016).
12. Littlewood, P. B. & Varma, C. M. Amplitude collective modes in superconductors and their coupling to charge-density waves. *Phys. Rev. B* **26**, 4883–4893 (1982).
13. Rüegg, C. et al. Quantum magnets under pressure: Controlling elementary excitations in $TlCuCl_3$. *Phys. Rev. Lett.* **100**, 205701 (2008).
14. Halperin, W. & Varoquax, E. in *Helium Three* (eds Halperin, W. & Pitaevskii, L.) 353–522 (Elsevier, Amsterdam, 1990).
15. Bissbort, U. et al. Detecting the amplitude mode of strongly interacting lattice bosons by Bragg scattering. *Phys. Rev. Lett.* **106**, 205303 (2011).
16. Endres, M. et al. The Higgs amplitude mode at the two-dimensional superfluid/Mott insulator transition. *Nature* **487**, 454–458 (2012).
17. Hoang, T. M. et al. Adiabatic quenches and characterization of amplitude excitations in a continuous quantum phase transition. *Proc. Natl Acad. Sci. USA* **113**, 9475–9479 (2016).

18. Leonard, J., Morales, A., Zupancic, P., Donner, T. & Esslinger, T. Monitoring and manipulating Higgs and Goldstone modes in a supersolid quantum gas. *Science* **358**, 1415–1418 (2017).
19. Yuzbashyan, E. A. & Dzero, M. Dynamical vanishing of the order parameter in a fermionic condensate. *Phys. Rev. Lett.* **96**, 230404 (2006).
20. Hannibal, S. et al. Quench dynamics of an ultracold Fermi gas in the BCS regime: Spectral properties and confinement-induced breakdown of the Higgs mode. *Phys. Rev. A* **91**, 043630 (2015).
21. Greiner, M., Regal, C. A. & Jin, D. S. Probing the excitation spectrum of a Fermi gas in the BCS–BEC crossover regime. *Phys. Rev. Lett.* **94**, 070403 (2005).
22. Chin, C. et al. Observation of the pairing gap in a strongly interacting Fermi gas. *Science* **305**, 1128–1130 (2004).
23. Ketterle, W. & Zwierlein, M. W in *Ultracold Fermi Gases, Proceedings of the International School of Physics "Enrico Fermi"* (eds M. Inguscio, W. Ketterle, and C. Salomon) **164**, 95–287 (IOS, Amsterdam, 2007).
24. Stewart, J. T., Gaebler, J. P. & Jin, D. S. Using photoemission spectroscopy to probe a strongly interacting Fermi gas. *Nature* **454**, 744–747 (2008).
25. Feld, M., Fröhlich, B., Vogt, E., Koschorreck, M. & Köhl, M. Observation of a pairing pseudogap in a two-dimensional Fermi gas. *Nature* **480**, 75–78 (2011).
26. Bruun, G. M. Low-energy monopole modes of a trapped atomic Fermi gas. *Phys. Rev. Lett.* **89**, 263002 (2002).
27. Korolyuk, A., Kinnunen, J. J. & Törmä, P. Density response of a trapped Fermi gas: A crossover from the pair vibration mode to the Goldstone mode. *Phys. Rev. A* **84**, 033623 (2011).
28. Korolyuk, A., Kinnunen, J. J. & Törmä, P. Collective excitations of a trapped Fermi gas at finite temperature. *Phys. Rev. A* **89**, 013602 (2014).
29. Tokimoto, J., Tsuchiya, S., & Nikuni, T. Higgs mode in a trapped superfluid Fermi gas. *J. Low Temp. Phys.* **187**, 765–770 (2017).
30. Ries, M. G. et al. Observation of pair condensation in the quasi-2D BEC–BCS crossover. *Phys. Rev. Lett.* **114**, 230401 (2015).
31. Schirotzek, A., Shin, Y.-i, Schunck, C. H. & Ketterle, W. Determination of the superfluid gap in atomic Fermi gases by quasiparticle spectroscopy. *Phys. Rev. Lett.* **101**, 140403 (2008).
32. Hoinka, S. et al. Goldstone mode and pair-breaking excitations in atomic Fermi superfluids. *Nat. Phys.* **13**, 943–946 (2017).
33. Chang, S. Y., Pandharipande, V. R., Carlson, J. & Schmidt, K. E. Quantum Monte Carlo studies of superfluid Fermi gases. *Phys. Rev. A* **70**, 043602 (2004).
34. Gezerlis, A. & Carlson, J. Strongly paired fermions: Cold atoms and neutron matter. *Phys. Rev. C* **77**, 032801 (2008).
35. Bulgac, A., Drut, J. E. & Magierski, P. Quantum Monte Carlo simulations of the BCS–BEC crossover at finite temperature. *Phys. Rev. A* **78**, 023625 (2008).
36. Chen, Q. Effect of the particle–hole channel on BCS–Bose–Einstein condensation crossover in atomic Fermi gases. *Sci. Rep.* **6**, 25772 (2016).
37. Haussmann, R., Rantner, W., Cerrito, S. & Zwerger, W. Thermodynamics of the BCS-BEC crossover. *Phys. Rev. A* **75**, 023610 (2007).
38. Pieri, P., Pisani, L. & Strinati, G. C. BCS–BEC crossover at finite temperature in the broken-symmetry phase. *Phys. Rev. B* **70**, 094508 (2004).
39. Ohashi, Y. & Griffin, A. Superfluidity and collective modes in a uniform gas of Fermi atoms with a Feshbach resonance. *Phys. Rev. A* **67**, 063612 (2003).

Methods

Preparation. Using standard techniques of laser cooling and sympathetic cooling in a mixture with sodium atoms in a magnetic trap, we prepare ~5×10^7 cold fermionic lithium atoms in a crossed-beam optical dipole trap of wavelength 1,070 nm in an equal mixture of the two lowest hyperfine states $|1\rangle$ and $|2\rangle$. Using subsequent evaporative cooling in a homogeneous magnetic field of 795 G, in the immediate vicinity of the Feshbach resonance at 834 G, we produce a condensate in the BCS/BEC crossover regime with a temperature of $T/T_F=0.07\pm0.02$. After preparation of the fermionic superfluid, the magnetic offset field is adiabatically adjusted in the range between 740 G and 1,000 G to control the interaction parameter $1/(k_Fa)$ in the range of $-0.8<1/(k_Fa)<1$ (that is, across the whole BCS/BEC crossover region).

Calibration of spectroscopy and analysis. We experimentally calibrate the modulation frequency and amplitude to take into account energy shifts owing to interaction effects of the initial and final states and the efficiency of the rf antenna set-up. To this end, we drive Rabi oscillations with set values of detuning δ and power and measure the population $P_{|3\rangle}$ as a function of time during the rf drive $P_{|3\rangle}=\alpha\sin^2(\Omega_{mod}t/2)$. This provides us with a direct measurement of the modulation frequency and amplitude. To model the data, we assume a Lorentzian line shape $\alpha=\frac{\Omega_R^2}{\Omega_R^2+(\delta-\delta_0)^2}$; however, we allow for a frequency shift $\delta_0(k_Fa)$ by which the detuning δ is corrected as compared to the Zeeman-energy resonance of the free atom. The fit parameter δ_0 absorbs the effects of interactions in the final state of the spectroscopy, the condensation energy of the initial state and the averaging of different momentum states and densities in the trap. Experimentally, the calibration is performed at a value of $\alpha\simeq4\%$ for which we obtain agreement with the Lorentzian model to a few per cent.

We check for unpaired atoms in the $|2\rangle$ state for red- and blue-detuned rf with respect to δ_0 as a result of the modulation. This has been achieved by rapidly ramping the field to 450 G with approximately 4 G μs^{-1}, which allows for the detection of free atoms rather than paired atoms. In the case of a red-detuned rf modulation, no enhancement of the signal of unpaired atoms could be observed over the whole range of modulation frequencies. However, blue-detuned rf modulation increases significantly the number of unpaired atoms due to single-particle excitations to the continuum (see Supplementary Fig. 1).

We also vary the driving strength α and observe that the resonance position of the peak with respect to the modulation frequency does not vary (see Supplementary Fig. 2).

Theoretical modelling. The experimental system can be described taking three different fermionic levels into account. Initially the system is prepared in a balanced mixture of states $|1\rangle$ and $|2\rangle$. Since we are mainly interested in the excitation mechanism and for this mainly the presence of a difference in the interaction strength between states ($|1\rangle$ and $|2\rangle$) and ($|1\rangle$ and $|3\rangle$) is needed, we take here only the interaction between these two states into account and decouple this term within the s-wave BCS channel. Using the rotating-wave approximation for the coupling between the states $|2\rangle$ and $|3\rangle$, we obtain the Hamiltonian

$$H=H_{BCS}+\sum_{\mathbf{k}}(\varepsilon_{\mathbf{k}}-\hbar\delta)n_{\mathbf{k},3}+\frac{\hbar\Omega_R}{2}\sum_{\mathbf{k}}(c^\dagger_{\mathbf{k},3}c_{\mathbf{k},2}+c^\dagger_{\mathbf{k},2}c_{\mathbf{k},3})$$

with

$$H_{BCS}=\sum_{\mathbf{k}}\varepsilon_{\mathbf{k}}(n_{\mathbf{k},1}+n_{\mathbf{k},2})+\sum_{\mathbf{k}}\{\Delta^*c_{-\mathbf{k},2}c_{\mathbf{k},1}+\Delta c^\dagger_{\mathbf{k},1}c^\dagger_{-\mathbf{k},2}\} \quad (1)$$

Here $\Delta=\frac{g}{V}\sum_{\mathbf{k}}\langle c_{-\mathbf{k},2}c_{\mathbf{k},1}\rangle$, Ω_R is the Rabi frequency, g is the interaction strength, V is the volume and the momentum-independent detuning is $\hbar\delta=\hbar\omega_{rf}-(\varepsilon_3^0-\varepsilon_2^0)$, where ε_n^0 is the bare energy for the state $n=2$, 3 and $\varepsilon_k=\hbar^2k^2/(2m)$ is the single-particle dispersion. We determine g from the scattering length using the expression provided in ref. [27].

To determine the time evolution of the order parameter, we derive a closed set of equations for the expectation values

$$\begin{aligned}
\hbar\frac{\partial}{\partial t}\langle c_{-\mathbf{k},2}c_{\mathbf{k},1}\rangle &= i\Big\{-2\varepsilon_{\mathbf{k}}\langle c_{-\mathbf{k},2}c_{\mathbf{k},1}\rangle-\frac{\hbar\Omega_R}{2}\langle c_{-\mathbf{k},3}c_{\mathbf{k},1}\rangle\\
&\quad+\Delta(n_{\mathbf{k},1}+n_{-\mathbf{k},2}-1)\Big\}\\
\hbar\frac{\partial}{\partial t}\langle c_{-\mathbf{k},3}c_{\mathbf{k},1}\rangle &= i\Big\{-\frac{\hbar\Omega_R}{2}\langle c_{-\mathbf{k},2}c_{\mathbf{k},1}\rangle\\
&\quad-(2\varepsilon_{\mathbf{k}}-\hbar\delta)\langle c_{-\mathbf{k},3}c_{\mathbf{k},1}\rangle+\Delta\langle c^\dagger_{-\mathbf{k},2}c_{-\mathbf{k},3}\rangle\Big\}\\
\hbar\frac{\partial}{\partial t}\langle c^\dagger_{-\mathbf{k},2}c_{-\mathbf{k},3}\rangle &= i\Big\{\Delta^*\langle c_{-\mathbf{k},3}c_{\mathbf{k},1}\rangle+\hbar\delta\langle c^\dagger_{-\mathbf{k},2}c_{-\mathbf{k},3}\rangle\\
&\quad-\frac{\hbar\Omega_R}{2}(n_{-\mathbf{k},2}-n_{-\mathbf{k},3})\Big\}\\
\hbar\frac{\partial}{\partial t}n_{\mathbf{k},1} &= -2\mathrm{Im}(\Delta^*\langle c_{-\mathbf{k},2}c_{\mathbf{k},1}\rangle)\\
\hbar\frac{\partial}{\partial t}n_{-\mathbf{k},2} &= -2\mathrm{Im}(\Delta^*\langle c_{-\mathbf{k},2}c_{\mathbf{k},1}\rangle)\\
&\quad+\hbar\Omega_R\mathrm{Im}(\langle c^\dagger_{-\mathbf{k},2}c_{-\mathbf{k},3}\rangle)\\
\hbar\frac{\partial}{\partial t}n_{-\mathbf{k},3} &= -\hbar\Omega_R\mathrm{Im}(\langle c^\dagger_{-\mathbf{k},2}c_{-\mathbf{k},3}\rangle)
\end{aligned}$$

where the number densities are defined as $n_{\mathbf{k},m}=\langle c^\dagger_{\mathbf{k},m}c_{\mathbf{k},m}\rangle$ with $m=1,2,3$. We solve these equations numerically discretizing both time t and momentum k and using the self-consistency condition $\Delta=\frac{g}{V}\sum_{\mathbf{k}}\langle c_{-\mathbf{k},2}c_{\mathbf{k},1}\rangle$ at each time step ensuring both the convergence for the time step dt and the momentum spacing. Typical values taken are $dk/k_F=5\times10^{-4}$, $dt=5\times10^{-4}\hbar/E_F$ and the cutoff for the momentum sum is $E_c=100E_F$.

The momentum-resolved spectral weight of the gap shown in Fig. 2c is computed as

$$A_{\mathbf{k}}(\omega)=V/g\left|\mathcal{F}\left\{|\Delta_{\mathbf{k}}(t)|-\frac{1}{T}\int_0^T dt\,|\Delta_{\mathbf{k}}(t)|\right\}\right| \quad (2)$$

with the momentum-dependent order parameter $\Delta_{\mathbf{k}}=(g/V)\langle C_{-\mathbf{k},2}C_{\mathbf{k},1}\rangle$. We use $T=400\hbar/E_F$ for the calculation.

Time evolution of the population of state $|3\rangle$. We compare the theoretical evolution of the population of atoms in state $|3\rangle$ (see Fig. 1c) during the application of the rf dressing to the experimental results. Supplementary Fig. 3 shows the population of the atoms in state $|3\rangle$ normalized to the initial atom number in state $|1\rangle$. The simulation and experiment were performed with the same effective modulation frequency, Ω_{mod}, and maximum atom transfer. Both curves show damped oscillations of the population of state $|3\rangle$ with time. The initial time behaviour up to approximately three oscillations agrees well between theory and experiment, which means that the dominant damping mechanism is due to a dephasing of the different momentum components. Afterwards, the experimental results show a stronger damping that we attribute to other damping mechanisms, such as, for example, the presence of collisions, which are not considered in the theoretical description.

Time evolution of the condensate fraction. We show the evolution of the condensate fraction during the application of the rf dressing in Supplementary Fig. 4. After different durations of the drive, the rapid mapping to the BEC side was performed and the condensate fraction was measured. The drive amplitude was chosen to be 5%. As a response, an oscillation of the condensate fraction close to the expected Rabi frequency can be observed over several oscillation periods with an amplitude of the order of 5%.

Comparison of the experimental and theoretical spectra. In Supplementary Fig. 5, we show a comparison of the experimentally measured spectra with the theoretical simulation. To gain insight into the structure expected from the excitation scheme, we theoretically extract the weight of the Higgs excitation for different effective modulation frequencies and plot these in the lower panel of Supplementary Fig. 5 for $1/(k_Fa)=-0.63$. To evaluate the area under the Higgs, for each momentum, we integrate around the Higgs excitation peak (shown in Fig. 2c) and then sum over all momenta along the Higgs excitation line. Let us note that this procedure leads to the artefact that at high modulation frequencies still a non-vanishing contribution to the weight is found, which, however, can be attributed to the excitation of quasiparticles in a homogeneous system and would vanish in a trapped system as considered experimentally. More importantly, we see that even though the Higgs mode has a very sharp frequency (as shown in Fig. 2c) and therefore a long lifetime, the resulting spectra show a much broader peak. The width of the peak is due to the excitation procedure. In particular, a resonant excitation of the Higgs mode is already possible if the effective modulation frequency lies below the sharp frequency of the Higgs mode, since then already some of the Rabi frequencies of the higher momentum components (compare stars in Fig. 2c) can resonantly excite the Higgs mode. Thus, the broadening of the spectral feature is mainly due to the particular excitation scheme and not a measurement of the lifetime of the Higgs mode. Let us conclude by pointing out that the full-width at half-maximum in both the theoretical and the experimental spectra is approximately $|\Delta|$.

Local-density approximation for the quasiparticle excitations. To study the effect of the harmonic trapping on the quasiparticle excitations, we performed a calculation of the system dynamics within the local-density approximation. Within the local-density approximation, we treat points of different density as effectively homogeneous systems with rescaled interaction $1/[k_F(\mathbf{r})a]$, Fermi energy $E_F(\mathbf{r})$ and chemical potential consistent with the system's density profile. We assume the density profile to be the one for non-interacting fermions as typically the profiles change only slightly for the considered interactions. The time evolution of the superconducting order parameter of the homogeneous system is performed locally for each point in the trap and rescaled to give $\Delta(\mathbf{r},t)/E_F(\mathbf{r}=0)$. We then take the density-weighted average of its Fourier transform. It is important to note that the Higgs mode—due to its collective nature—cannot be treated in this formalism, so we remove the Higgs peak in each Fourier transform by hand before we take the trap average. Integrating the resulting spectrum gives the background excitation weight (see Supplementary Fig. 6). In contrast to the peaked quasiparticle structure of a homogeneous system, we find the trap-averaged background excitation weight to be significantly broadened resulting in a featureless, broad background.

Data availability. The data that support the plots within this paper and other findings of this study are available from the corresponding author upon reasonable request.

ARTICLE

Private and secure communication is of fundamental importance in the modern world. Traditional public-key cryptography relies on the computational intractability of certain mathematical functions. In contrast, QKD[1]—which was proposed in the mid-1980s and is the best known example of a task involving quantum cryptography—provides an information-secure solution to the key exchange problem, ensured by the laws of quantum physics. QKD enables two distant users who do not initially share any information to produce a common, random string of secret bits, called a secret key. Using one-time-pad encryption, this key provides a provably secure[2] way of encrypting (and decrypting) a message, which can then be transmitted over a standard communication channel. In QKD, the information is encoded in the superposition states of physical carriers at the single-quantum level; as the fastest-travelling qubits, and owing to their intrinsic robustness to decoherence and the ease with which they can be controlled, photons are usually used as the physical carriers. Any eavesdropper on the quantum channel attempting to gain information about the key will inevitably introduce disturbances into the system, and so can be detected by the communicating users.

Since the first table-top QKD experiment[3] in 1989, with a quantum channel distance of 32 cm, much research has been devoted to achieving secure QKD over long distances, with the ultimate aim being global-scale secure QKD for practical use. The most straightforward method of QKD is sending single photons through optical fibres or terrestrial free-space directly. However, in both of these cases channel loss causes a decrease in the number of transmitted photons that scales exponentially with the length over which they are transmitted. Unlike classical telecommunications, the quantum signal in QKD cannot be noiselessly amplified, owing to the quantum non-cloning theorem[4], limiting the maximum distance for secure QKD to a few hundred kilometres[5]. Beyond this length scale, quantum communications become extremely challenging[6].

One solution to this problem is to use quantum repeaters[7] that combine entanglement swapping[8], entanglement purification[9] and quantum memories[10]. But despite remarkable progress in demonstrations of the three building blocks[11–13] and even prototype quantum repeater nodes[14–18], these laboratory technologies are still far from being applicable in practical long-distance quantum communications.

A more direct and promising solution for global-scale QKD involves satellites in space. Compared with terrestrial channels, the satellite-to-ground connection has greatly reduced losses[19]. This is mainly because the effective thickness of the atmosphere is only about 10 km, and most of the propagation path of the photons is in empty space with negligible absorption and turbulence. A ground test[20] in 2004 demonstrated the distribution of entangled photon pairs over a noisy near-ground atmosphere of 13 km—greater than the effective thickness of the atmosphere—and showed the survival of entanglement and a violation of Bell's inequality. Under the simulated conditions of huge attenuation and various types of turbulence, the feasibility of satellite-based QKD has been further verified over even longer distances[21–23], on rapidly moving platforms[24,25] and using satellite corner-cube retroreflectors[26,27].

We developed a sophisticated satellite, 'Micius', dedicated for quantum science experiments, which was successfully launched on 16 August 2016 from Jiuquan, China, and now orbits at an altitude of about 500 km (Fig. 1a; see Methods for the project timeline and design details). Using one of the satellite payloads—a decoy-state QKD transmitter at a wavelength of 850 nm—and cooperating with Xinglong ground observatory station (near Beijing, 40° 23′ 45.12″ N, 117° 34′ 38.85″ E, altitude of 890 m), we establish decoy-state QKD with

[1]Department of Modern Physics and Hefei National Laboratory for Physical Sciences at the Microscale, University of Science and Technology of China, Hefei 230026, China. [2]Chinese Academy of Sciences (CAS) Center for Excellence and Synergetic Innovation Center in Quantum Information and Quantum Physics, University of Science and Technology of China, Shanghai 201315, China. [3]Key Laboratory of Space Active Opto-Electronic Technology, Shanghai Institute of Technical Physics, Chinese Academy of Sciences, Shanghai 200083, China. [4]National Astronomical Observatories, Chinese Academy of Sciences, Beijing 100012, China. [5]Key Laboratory of Optical Engineering, Institute of Optics and Electronics, Chinese Academy of Sciences, Chengdu 610209, China. [6]Shanghai Engineering Center for Microsatellites, Shanghai 201203, China. [7]State Key Laboratory of Astronautic Dynamics, Xi'an Satellite Control Center, Xi'an 710061, China. [8]Xinjiang Astronomical Observatory, Chinese Academy of Sciences, Urumqi 830011, China. [9]National Space Science Center, Chinese Academy of Sciences, Beijing 100190, China.

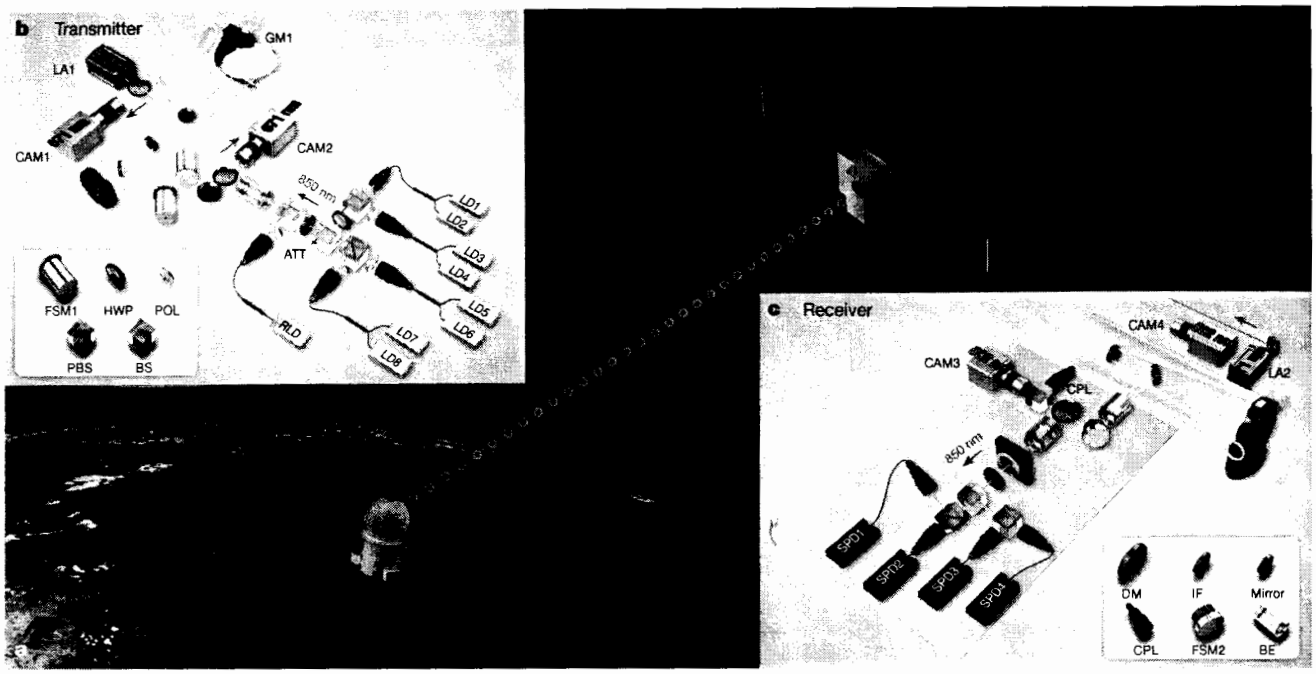

Figure 1 | Illustration of the experimental set-up. a, Overview of the satellite-to-ground quantum key distribution (QKD). The Micius satellite, weighing 635 kg, flies along a Sun-synchronous orbit at an altitude of around 500 km. It is equipped with three payloads, designed and tested to be suitable for operation in low-Earth orbit and to enable a series of space-to-ground-scale quantum experiments including QKD, a Bell test and teleportation. **b**, Schematic of the decoy-state QKD transmitter, one of the satellite's payloads. Attenuated laser pulses (with wavelengths of about 850 nm) from eight separate laser diodes (LD1–LD8) pass through a BB84 encoding module, which consists of two polarizing beam splitters (PBSs), a half-wave plate (HWP) and a beam splitter (BS). The resultant beam is then co-aligned with a green laser beam (LA1; 532 nm) for system tracking and time synchronization, and sent out through a 300-mm-aperture Cassegrain telescope. After the BB84 module, an approximately 5-μW laser is used as a polarization reference. A two-axis gimbal mirror (GM1) in the output of the telescope and a large-field-of-view camera (CAM1) are combined to control the coarse-tracking loop. Two fast steering mirrors (FSM1s) and a fast camera (CAM2) are used for fine tracking. ATT, attenuator; POL, polarizer; RLD, polarization reference laser diode; both cameras (CAM1 and CAM2) detect 671-nm light. **c**, Schematic of the decoy-state QKD decoder at the Xinglong ground station, which is equipped with a 1,000-mm-aperture telescope. The received 532-nm-wavelength laser is separated by a dichromic mirror (DM) and split into two paths: one is imaged by a camera (CAM3, which detects 532-nm light) for tracking and the other is detected for time synchronization. The 850-nm-wavelength decoy-state photons are analysed by a BB84 decoder, which consists of a beam splitter and two polarizing beam splitters, and detected by four single-photon detectors (SPD1–SPD4). The ground station sends a red laser (LA2; 671 nm) beam to the satellite for system tracking. IF, interference filter; BE, beam expander; CPL, coupler; both cameras (CAM3 and CAM4) detect 532-nm light. See Extended Data Table 1 for more technical parameters.

polarization encoding from the satellite to the ground with a kilohertz key rate over a distance of up to 1,200 km.

Experimental challenges and solutions

Robust and efficient satellite-to-ground QKD places a more stringent requirement on the efficiency of the link than do conventional satellite-based classical communication systems. To obtain a high signal-to-noise ratio, one cannot increase the signal power, only reduce the channel attenuation and background noise. In our experiment, several effects contribute to channel loss, including beam diffraction, pointing error, atmospheric turbulence and absorption.

In our QKD experiment, we adopt the downlink protocol—from the satellite to the ground (see Fig. 1a). In the downlink, beam wandering caused by atmospheric turbulence occurs at the very end of the transmission path (near the surface of Earth), where the beam size due to diffraction is typically much larger than the beam wandering. Therefore, the downlink has reduced beam spreading compared to the uplink and thus higher link efficiency.

The beam diffraction depends mainly on the size of the telescope. To narrow the beam divergence, we use a 300-mm-aperture Cassegrain telescope in the satellite (Fig. 1b), optimized to eliminate chromatic and spherical aberrations; this telescope sends the light beam with a near-diffraction-limited far-field divergence of about 10 μ rad. After travelling a distance of 1,200 km, we expect that the beam diameter expands to about 12 m. At the ground station, a Ritchey–Chretien telescope with an aperture of 1 m and a focal length of 10 m (Fig. 1c) is used to receive the QKD photons (see Methods). The diffraction loss is estimated to be 22 dB at 1,200 km.

The narrow divergence beam from the fast-moving satellite (speed of about 7.6 km s^{-1}) necessitates a high-bandwidth and high-precision acquiring, pointing and tracking (APT) system to establish a stable link. We designed cascaded multi-stage APT systems in the transmitter (Fig. 1b) and the receiver (Fig. 1c). Initial coarse orientation of the telescope is based on the forecasted orbital position of the satellite, with an uncertainty of less than 200 m. The satellite's attitude control system ensures that the transmitter is pointing to the ground station with a precision of approximately 0.5°. The satellite and the ground station send beacon lasers to each other with a divergence of 1.25 mrad (satellite to ground) and 0.9 mrad (ground to satellite) (Fig. 2a). The coarse pointing stage in the satellite transmitter consists of a two-axis gimbal mirror (with a range of 10° in both azimuth and elevation) and a complementary metal–oxide semiconductor (CMOS) camera with a field-of-view of 2.3° × 2.3° and frame rates of 40 Hz. The fine pointing stage uses a fast-steering mirror driven by piezo ceramics (with a tracking range of 1.6 mrad) and a camera with a field-of-view of 0.64 mrad × 0.64 mrad and frame rates of 2 kHz. Similar coarse and fine APT systems are also installed in the ground station (see Extended Data Table 1 for details). Using closed-loop feedback, the transmitter achieves a tracking accuracy of approximately 1.2 μrad (Fig. 2b), much smaller than the beam divergence. We estimate that at 1,200 km the loss due to atmospheric absorption and turbulence is 3–8 dB and that due to pointing error is less than 3 dB.

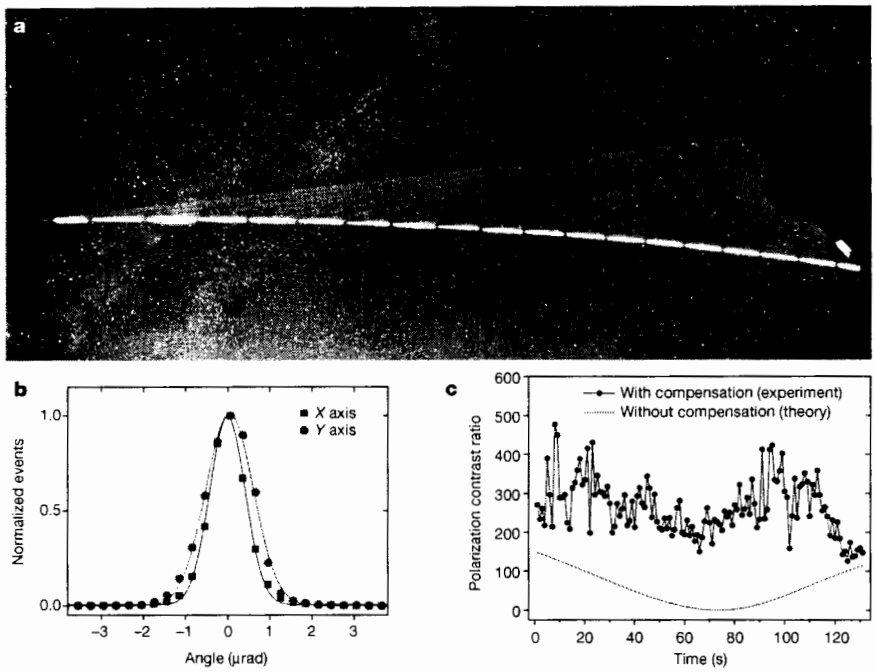

Figure 2 | Establishing a reliable space-to-ground link for quantum state transfer. a, Overlaid and time-lapse photographs of tracking laser beams as the satellite flies over the Xinglong ground station. The red and green lasers are sent from the ground and the satellite, respectively, with a divergence of 0.9–1.25 mrad. **b**, Distribution of long-time tracking error (shown as the number of detected events normalized by the maximum count in each bin) of the *X* and *Y* axes extracted from the real-time images read out from the fast camera. **c**, Polarization contrast ratio with (corresponding to our experiment) and without (determined theoretically) dynamical compensation during one orbit.

We use temporal and spectral filtering to suppress the background noise. The beacon laser, with a pulse width of 0.9 ns and a repetition rate of about 10 kHz, is used for both APT and synchronization. In good co-alignment with the QKD photons, the beacon laser can be separated by a dichroic mirror and detected by a single-photon detector in the ground station to obtain timing information. We thus avoid the space–ground clock drift, obtaining a synchronization jitter of 0.5 ns, which is used to tag the received signal photons within a 2-ns time window and filter out the background noise. In addition, we use a bandwidth filter in the receiver to reduce the background scattering. In the current experiment, we limit ourselves to night-time operation to avoid sunlight.

Finally, the relative motion of the satellite and the ground station induces a time-dependent rotation of the photon polarization seen by the receiver. We predict theoretically that the polarization contrast ratio would decrease from 150:1 to 0 during one orbit (Fig. 2c). To solve this problem, we calculate rotation angle offset by taking into account the relative motion of the satellite and the ground station and all of the birefringent elements in the optical path. Using a motorized half-wave plate for dynamical polarization compensation during the satellite passage, the average polarization contrast ratio increases to 280:1 (Fig. 2c).

Experimental procedure and results

We use the decoy-state[28,29] Bennett–Brassard 1984 (BB84)[1] protocol for QKD, which can detect photon-number-splitting eavesdropping and thus enable secure QKD using weak coherent pulses over very large distances and with very high key rates. The main idea is to use multiple intensity levels at the source of the transmitter: one signal state (the mean photon number μ_s) and several randomly interspersed decoy states (μ_1, μ_2, ...). Here we use a protocol with three intensity levels: high μ_s, moderate μ_1 and zero μ_2 (vacuum), sent with probabilities of 50%, 25% and 25%, respectively. These intensity levels are optimized by performing simulations to maximize the secret bit rate for the satellite-to-ground channel.

For downlink QKD, a transmitter (designed and tested to be suitable for operation in low-Earth orbit) is integrated in the satellite (see Fig. 1b). Eight fibre-based laser diodes—four used as signal and four as decoy states—emit laser pulses (848.6 nm, 100 MHz, 0.2 ns). The output power of the eight laser didoes is monitored in real time by internal integrated photodetectors and controlled remotely by closed-loop systems, which precisely set the required intensity of the signal and decoy states and stabilize with less than 5% variation. In-orbit measurements show that with independent temperature tuning of the eight lasers their wavelengths are matched to within 0.006 nm, much smaller than their intrinsic bandwidth (about 0.1 nm). The lasers are synchronized to be within <10 ps, much smaller than their pulse duration of around 200 ps. The output beams are coaligned to ensure that both concentricity and coaxiality are better than 95%.

The light beams are then sent to a BB84-encoding module consisting of a half-wave plate, two polarizing beam splitters and a beam splitter, which randomly prepares the emitted photons in one of the four polarization states: horizontal, vertical, linear $+45°$ or linear $-45°$. A physical thermal noise device generates a 4-bit random number for each run that drives the eight lasers and determines the output polarization and intensity levels. Independent electric control of the eight lasers and adjustment of the attenuation allow us to accurately obtain the average photon number in the output of the telescope: $\mu_s = 0.8$, $\mu_1 = 0.1$ and $\mu_2 = 0$. In the ground station, a compact decoding set-up consisting of a beam splitter, two polarizing beam splitters and four single-photon detectors (efficiency, 50%; dark counts, <25 Hz; timing jitter, 350 ps) is used for polarization-state analysis (see Fig. 1c and Methods). The overall optical efficiency, including the receiving telescope and the fibre coupling on the ground station, is approximately 16%. The satellite uses a radio-frequency channel for classical communication with the ground station (with an uplink and downlink bandwidth of 1 Mbit s^{-1} and 4 Mbit s^{-1}, respectively), and its experimental control-box payload to perform the sifting, error correction and privacy amplification.

The satellite passes Xinglong ground station along a Sun-synchronous orbit once every night starting at around 00:50 local time, for a duration of about 5 min. About 10 min before the satellite enters the shadow zone, its attitude is adjusted to point at the ground station. When the satellite exceeds an elevation angle of 5° from the horizon

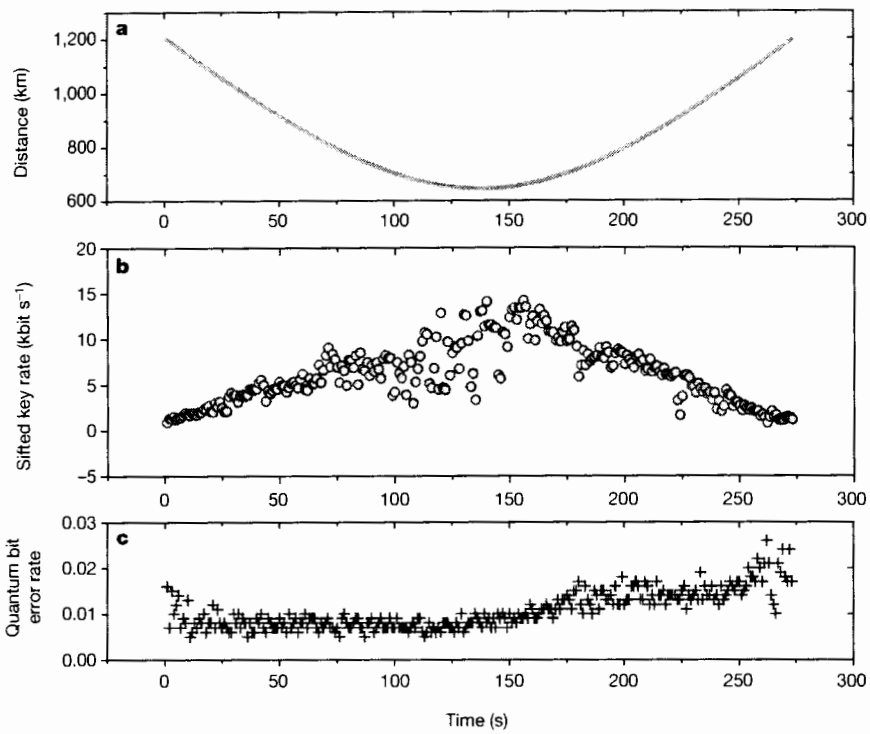

Figure 3 | Performance of satellite-to-ground QKD during one orbit. a, The trajectory of the Micius satellite measured from Xinglong ground station. **b**, The sifted key rate as a function of time and physical distance from the satellite to the station. **c**, Observed quantum bit error rate. See text for detailed discussion of the results, and Extended Data Table 2 and Extended Data Fig. 1 for additional data on different days.

plane of the ground station, a pointing accuracy of better than 0.5° is achieved. The APT systems then start bidirectional tracking and pointing to guarantee that the transmitter and receiver are robustly locked throughout the orbit. From an elevation angle of about 15°, the QKD transmitter sends randomly modulated signal and decoy photons, together with the beacon laser for timing synchronization, which are received and detected by the ground station. A single-orbit experiment ends when the satellite again reaches an elevation angle of 10°, this time on its descent (see Methods).

Since September 2016, we have routinely been able to successfully perform QKD under good atmospheric conditions. In Fig. 3a we show the data for the orbit on 19 December 2016, with a minimal (maximal) separation of 645 km (1,200 km). Within a duration of 273 s for the QKD data collection, the ground station collected 3,551,136 detection events, corresponding to 1,671,072 bits of sifted keys (see Fig. 3b). The sifted key rate decreases from about 12 kbit s^{-1} at 645 km to 1 kbit s^{-1} at 1,200 km, owing to the increase both in the physical separation distance and in the effective thickness of the atmosphere near Earth at smaller elevation angles. The time trace of the sifted key rate in Fig. 3b demonstrates that we are reliably able to obtain the keys throughout the duration of the data collection. However, more pronounced fluctuation in the key rate is observed near the central points of the orbit, when the satellite passes directly over the ground station and its effective angular velocity reaches its maximum (about 1° s^{-1}), thus placing stringent demands on the APT system. In Fig. 3c we show the observed quantum bit error rate, with an average of 1.1%, consistent with the expected error rate due to background noise and polarization visibility. The quantum bit error rates are slightly higher in the second half of the orbit, when the ground telescope faces towards Beijing and so there is more background light from the city.

We then perform error correction and privacy amplification to obtain the final keys. After randomly shuffling the sifted key, a hamming algorithm is used for error correction. We perform privacy amplification to reduce the possible knowledge of an eavesdropper by applying a random matrix over the corrected keys. Moreover, we take into account the intensity fluctuations for the signal and decoy states ($<5\%$) and, when the statistical failure probability is set to 10^{-9}, calculate a secure final key of 300,939 bits, corresponding to a key rate of approximately 1.1 kbit s^{-1}.

As in previous experiments[24,25], here the key analysis does not consider information leakage due to possible side channels from the imperfect spatial, temporal and spectral overlap of the quantum light sources. The use of multiple laser diodes for different (signal and decoy) states and intensities can cause small (a few per cent here), non-ideal state overlap, which can be straightforwardly mitigated in future work by using narrowband spectral filtering or by adopting decoy-state QKD transmitters with only a single laser diode and modulating the created state externally.

The QKD experiments performed on 23 different days, with different physical distances between the satellite and the ground station, are summarized in Extended Data Table 2 and Extended Data Fig. 1. The shortest satellite-to-station distance depends on the highest altitude angle of the day, and varies from 507.0 km at 85.7° to 1,034.7 km at 25.0°. The sifted key that is obtained has a peak key rate of 40.2 kbit s^{-1} at 530 km and decreases for larger distances, for instance to 1.2 kbit s^{-1} at 1,034.7 km. From Extended Data Fig. 1, we also observe the fluctuation in the key rate due to different weather conditions. The quantum bit error rates are measured to be 1%–3%.

We compare the performance of our satellite-based QKD with that expected from the conventional method of direct transmission through optical telecommunication fibres. In Fig. 4 we show the link efficiency over distances of 645–1,200 km extracted from the observed count rate, together with theoretically calculated link efficiency assuming fibres with loss of 0.2 dB km^{-1}. Despite the short coverage time using the Micius satellite (273 s per day) and the need for reasonably good weather conditions, we observe an enhancement in efficiency compared to telecommunication fibres, which increases for larger distances; at 1,200 km, the channel efficiency of the satellite-based QKD over the 273-s coverage time is 20 orders of magnitudes higher than that achieved using the optical fibre. As a comparison with our data in Fig. 3b, over a distance of 1,200 km, even with a perfect 10-GHz single-photon source and ideal single-photon detectors with no dark count, transmission through optical fibres would result in only a 1-bit sifted key over six million years.

Discussion and outlook

We have reported satellite-to-ground quantum communication over a distance scale of 1,200 km. Our satellite can be further used as a

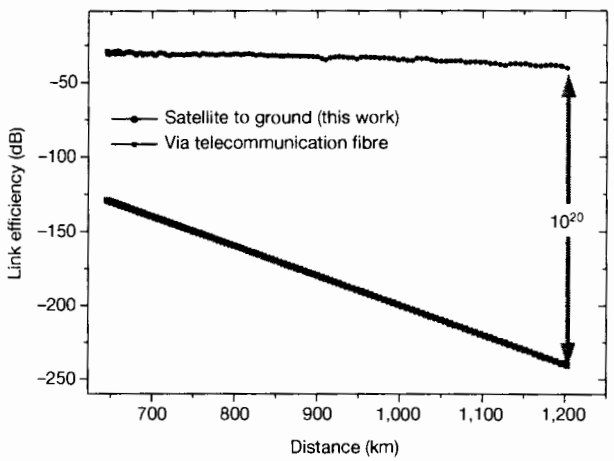

Figure 4 | QKD link efficiencies. Link efficiencies are shown for direct transmission through telecommunication optical fibres (red) and the satellite-to-ground approach (blue). The link efficiencies for the latter were calculated by dividing the photon intensity that arrived in front of the detectors at the ground station by that at the output of the satellite's transmitter. At a distance of 1,200 km, the satellite-to-ground approach (within the satellite coverage time) is more efficient than direct transmission by 20 orders of magnitude.

reliable relay to conveniently connect any two points on Earth for high-security key exchange. For example, we can first implement QKD in Xinglong, after which the key is stored in the satellite for 2 h until it reaches Nanshan station near Urumqi, a distance of about 2,500 km from Beijing. By performing another QKD between the satellite and the Nanshan station and using one-time-pad encoding, a secure key between Xinglong and Nanshan can be established. Future experimental plans include intercontinental secure-key exchanges between China and Austria, Italy and Germany.

Thus far, the shortcomings of the low-Earth-orbit satellite are limited coverage area and amount of time spent within range of each ground station. To increase the coverage, we plan to launch satellites with higher orbits and to construct a satellite constellation, requiring the development of new techniques to increase the link efficiency, including larger telescopes, better APT systems and wave-front correction through adaptive optics. However, higher-orbit satellites will spend less time in Earth's shadow; daytime QKD can be implemented using telecommunication-wavelength photons and improved spatial and spectral filtering[30].

The satellite-based QKD can be linked to metropolitan quantum networks, in which fibres are sufficient and convenient to connect numerous users in a city over distance scales of approximately 100 km (ref. 31). We thus envision a space–ground integrated quantum network, enabling useful quantum cryptography—probably the first commercial application of quantum information—at the global scale.

Online Content Methods, along with any additional Extended Data display items and Source Data, are available in the online version of the paper; references unique to these sections appear only in the online paper.

Received 20 March; accepted 21 July 2017.
Published online 9 August 2017.

1. Bennett, C. H. & Brassard, G. Quantum cryptography: public key distribution and coin tossing. In *Proc. Int. Conf. on Computers, Systems and Signal Processing* 175–179 (1984).
2. Shannon, C. E. Communication theory of secrecy systems. *Bell Syst. Tech. J.* **28,** 656–715 (1949).
3. Bennett, C. H. & Brassard, G. Experimental quantum cryptography: the dawn of a new era for quantum cryptography: the experimental prototype is working! *ACM Sigact News* **20,** 78–80 (1989).
4. Wootters, W. K. & Zurek, W. H. A single quantum cannot be cloned. *Nature* **299,** 802–803 (1982).
5. Yin, H.-L. *et al.* Measurement-device-independent quantum key distribution over a 404 km optical fiber. *Phys. Rev. Lett.* **117,** 190501 (2016).
6. Brassard, G., Lütkenhaus, N., Mor, T. & Sanders, B. C. Limitations on practical quantum cryptography. *Phys. Rev. Lett.* **85,** 1330–1333 (2000).
7. Briegel, H.-J., Dür, W., Cirac, J. I. & Zoller, P. Quantum repeaters: the role of imperfect local operations in quantum communication. *Phys. Rev. Lett.* **81,** 5932–5935 (1998).
8. Żukowski, M., Zeilinger, A., Horne, M. A. & Ekert, A. K. 'Event-ready-detectors' Bell experiment via entanglement swapping. *Phys. Rev. Lett.* **71,** 4287–4290 (1993).
9. Bennett, C. H. *et al.* Purification of noisy entanglement and faithful teleportation via noisy channels. *Phys. Rev. Lett.* **76,** 722–725 (1996).
10. Duan, L.-M., Lukin, M. D., Cirac, J. I. & Zoller, P. Long-distance quantum communication with atomic ensembles and linear optics. *Nature* **414,** 413–418 (2001).
11. Pan, J.-W., Bouwmeester, D., Weinfurter, H. & Zeilinger, A. Experimental entanglement swapping: entangling photons that never interacted. *Phys. Rev. Lett.* **80,** 3891–3894 (1998).
12. Pan, J.-W., Gasparoni, S., Ursin, R., Weihs, G. & Zeilinger, A. Experimental entanglement purification of arbitrary unknown states. *Nature* **423,** 417–422 (2003).
13. Yang, S.-J., Wang, X.-J., Bao, X.-H. & Pan, J.-W. An efficient quantum light–matter interface with sub-second lifetime. *Nat. Photon.* **10,** 381–384 (2016).
14. Chou, C.-W. *et al.* Functional quantum nodes for entanglement distribution over scalable quantum networks. *Science* **316,** 1316–1320 (2007).
15. Yuan, Z.-S. *et al.* Experimental demonstration of a BDCZ quantum repeater node. *Nature* **454,** 1098–1101 (2008).
16. Sangouard, N., Simon, C., De Riedmatten, H. & Gisin, N. Quantum repeaters based on atomic ensembles and linear optics. *Rev. Mod. Phys.* **83,** 33–80 (2011).
17. Ritter, S. *et al.* An elementary quantum network of single atoms in optical cavities. *Nature* **484,** 195–200 (2012).
18. Bernien, H. *et al.* Heralded entanglement between solid-state qubits separated by three metres. *Nature* **497,** 86–90 (2013).
19. Rarity, J. G., Tapster, P. R., Gorman, P. M. & Knight, P. Ground to satellite secure key exchange using quantum cryptography. *New J. Phys.* **4,** 82 (2002).
20. Peng, C.-Z. *et al.* Experimental free-space distribution of entangled photon pairs over 13 km: towards satellite-based global quantum communication. *Phys. Rev. Lett.* **94,** 150501 (2005).
21. Ursin, R. *et al.* Entanglement-based quantum communication over 144 km. *Nat. Phys.* **3,** 481–486 (2007).
22. Yin, J. *et al.* Quantum teleportation and entanglement distribution over 100-kilometre free-space channels. *Nature* **488,** 185–188 (2012).
23. Ma, X.-S. *et al.* Quantum teleportation over 143 kilometres using active feed-forward. *Nature* **489,** 269–273 (2012).
24. Wang, J.-Y. *et al.* Direct and full-scale experimental verifications towards ground–satellite quantum key distribution. *Nat. Photon.* **7,** 387–393 (2013).
25. Nauerth, S. *et al.* Air-to-ground quantum communication. *Nat. Photon.* **7,** 382–386 (2013).
26. Yin, J. *et al.* Experimental quasi-single-photon transmission from satellite to earth. *Opt. Express* **21,** 20032–20040 (2013).
27. Vallone, G. *et al.* Experimental satellite quantum communications. *Phys. Rev. Lett.* **115,** 040502 (2015).
28. Wang, X.-B. Beating the photon-number-splitting attack in practical quantum cryptography. *Phys. Rev. Lett.* **94,** 230503 (2005).
29. Lo, H.-K., Ma, X. & Chen, K. Decoy state quantum key distribution. *Phys. Rev. Lett.* **94,** 230504 (2005).
30. Liao, S.-K. *et al.* Long-distance free-space quantum key distribution in daylight towards inter-satellite communication. *Nat. Photon.* **11,** 509–513 (2017).
31. Chen, T.-Y. *et al.* Metropolitan all-pass and inter-city quantum communication network. *Opt. Express* **18,** 27217–27225 (2010).

METHODS

Timeline and details of China's Micius project. 2003: A pre-study project, 'free-space quantum communications', was assigned by the Chinese Academy of Sciences (CAS) to test the feasibility of satellite-based quantum communications.

2004: Distribution of entangled photons over 13 km through a noisy near-ground atmosphere over Hefei city was achieved, reaching a distance of more than the effective thickness of the aerosphere[1].

2007: The 'Quantum Experiments at Space Scale' project, aimed at developing important techniques for performing quantum experiments at the space scale, was supported by CAS.

2007: Quantum teleportation[2] over the Great Wall in Beijing, a distance of 16 km, was achieved.

2010: Direct and full-scale experimental verifications towards ground–satellite QKD were implemented near Qinghai Lake in western China, on a moving platform (using a turntable), on a floating platform (using a hot-air balloon) and with a high-loss channel (96 km, about 50 dB)[3].

2011: Quantum teleportation and bidirectional entanglement distribution over an approximately 100-km free-space channel were achieved over Qinghai Lake[4]. These results demonstrated the technical ability of handling the high-loss ground-to-satellite uplink channel and satellite-to-ground two-downlink channel.

2011: The 'Quantum Science Satellite' project was officially approved by CAS.

2012: Construction of the first prototype satellite began.

2014: The first prototype satellite was completed. The observatory station in Xinglong was completed.

2015: The flight model of the satellite was completed. The observatory stations in Nanshan and Delingha were completed. QKD and entanglement distribution experiments were conducted between the payloads of the first prototype satellite and the Delingha observatory station, over a distance of 17 km. A quantum teleportation experiment was also conducted between the payloads of the first prototype satellite and a transmitter placed in the Delingha station.

2016: The satellite passed through a series of environmental tests, including thermal vacuum, thermal cycling, shock, vibration and electromagnetic compatibility. The observatory stations in Lijiang and Ngari were completed.

2016: The Micius satellite, weighing 635 kg, was launched at 01:40 Beijing time on 16 August 2016 by a Long March 2D rocket from the Jiuquan Satellite Launch Centre, China. (A full view of the satellite before being assembled in the rocket is shown in Extended Data Fig. 2a).

The satellite's payloads. The satellite's payloads for the QKD experiment are composed of an experimental control box (with a weight of 7.56 kg, Extended Data Fig. 2b), an APT control box (9.9 kg, Extended Data Fig. 2c) and an optical transmitter (115 kg, Extended Data Fig. 2d).

The experimental control box has six functions: experimental process management, random-number generation and storage, modulation for the decoy-state photon source, synchronization-pulse recording, QKD post-processing (including raw-key sifting, error correction and privacy amplification to obtain the secure final keys) and encryption management.

The optical transmitter is composed of eight laser diodes with their drivers, a BB84 polarization-encoding module (Extended Data Fig. 2e, f), a telescope and an APT system (including a beacon laser, a coarse camera, a two-axis mirror, a fine camera, a fast-steering mirror (FSM), and so on). The QKD photons are generated and transmitted to the ground station by the optical transmitter.

The APT control box contains mainly the control electronics for the coarse-tracking loop and the fine-tracking loop. The specific functions include motor driver, FSM driver, coarse-feedback-loop controller and fine-feedback-loop controller.

Ground station in Xinglong. The Xinglong observatory is located about 110 km to the northeast of Beijing. The observatory station in Xinglong consists of a Ritchey–Chretien telescope (aperture of 1 m, focal length of 10 m) mounted on a two-axis gimbal (Extended Data Fig. 3a), a red beacon laser (671 nm, 2.7 W, 0.9 mrad), a coarse camera (field-of-view (FOV) of $0.33° \times 0.33°$, 512×512 pixels, frame rate of 56 Hz; Extended Data Fig. 3b) and an optical receiver box located on the arm of the gimbal (Extended Data Fig. 3a).

The coarse-tracking system consists of a two-axis gimbal in a control loop with a coarse camera. The coarse camera is used to detect the 532-nm beacon laser coming from the satellite. Guided by the 532-nm beacon laser, the 671-nm beacon laser installed on the ground telescope can point to the satellite precisely.

The fine-tracking system and the 850-nm photon receiver are mounted in the receiver box (part of the receiver box is shown in Extended Data Fig. 3c). The fine-tracking system consists mainly of a FSM based on a voice-coil and a fine camera (FOV of 1.3 mrad × 1.3 mrad, 128×128 pixels, frame rate of 212 Hz). A dichromic mirror is used to separate the 850-nm photons from the 532-nm beam. A beam splitter is used to divide the 532-nm beam into two parts. One is sent to the fine camera for tracking and the other is sent to an optical coupler linked to a single-photon detector for synchronization.

After passing through a beam expander, a motorized half-wave plate (HWP) and an interference filter, the 850-nm photons are received by a customized BB84 polarization-analysis module. Four multimode fibres with core diameters of 105 μm are used to connect the receiver module with four single-photon detectors. The electric output pulses from all five single-photon detectors and a global positioning system (GPS) pulse-per-second (PPS) signal are fed into a time-to-digital convertor (TDC), which records the detecting time and the channel numbers of the detectors. The acquired data are stored in the computer for further processing.

APT systems. The optical transmitter in the satellite and the receiver in the ground station both have cascaded multistage APT systems (Extended Data Fig. 4).

In the transmitter, there is a three-stage APT system. The first stage is the satellite attitude control system, which keeps the QKD photons pointing to the ground station with an error of less than 0.5°. The second stage is the coarse-control loop, which includes a two-axis gimbal mirror (azimuth and elevation rotation ranges of 10°) and a CMOS camera (FOV of $2.3° \times 2.3°$, frame rate of 40 Hz). The third stage is the fine-control loop, which is composed of a FSM driven by piezo ceramics (tracking range of 1.6 mrad) and a camera (FOV of 0.64 mrad × 0.64 mrad, frame rate of 2 kHz).

In the receiver, a two-stage APT system is used. The first stage is the coarse-control loop, including a two-axis gimbal telescope (azimuth rotation range of about −270° to +270°, elevation rotation range of about −5° to +95°) and a CCD camera (FOV of $0.33° \times 0.33°$, frame rate of 56 Hz). The second stage is the fine-control loop, including a FSM driven by a voice-coil (tracking range of ±35 mrad) and a CCD camera (FOV of 1.3 mrad × 1.3 mrad, frame rate of 212 Hz).

At the beginning, on the basis of the predicted orbit of the satellite, the receiver points a 671-nm beacon laser (2.7 W) towards the satellite in real time. The coarse camera in the satellite detects the 671-nm beacon laser to obtain the tracking error of the line-of-sight. With the feedback control of the two-axis gimbal mirror and the coarse camera, the coarse tracking error is less than 10 μrad, much smaller than the FOV of the fine camera. The fine tracking error is less than 2 μrad, owing to the feedback control of the FSM and the fine camera.

The optical transmitter in the satellite simultaneously points a beacon laser (wavelength of 532 nm, optical power of 160 mW, divergence angle of 1.25 mrad) towards the ground station. The ground station uses this beacon laser to correct its pointing direction, with an error of about 1–2 μrad. Finally, the link is locked onto the transmitter and the receiver in a closed-loop tracking.

The optical transmitter sends the QKD photons with a 'point-ahead angle' to the receiver. The 'point-ahead angle' is a series of angles to compensate for the transverse velocity of the two terminals and the speed of light, achieved by adjusting the tracking reference of the transmitter's fine-tracking loop in real time.

Synchronization. Because the transmitter and the receiver are separated by a large distance and have independent reference clocks, time synchronization is used to label QKD photon pulse sequences by their arrival time, which can be used to distinguish the QKD photons from the background noise. Because the distance between the transmitter and the receiver changes as the satellite passes over the ground station, we use both the GPS PPS signal and an assistant pulse laser in our synchronization scheme.

In the transmitter, the 532-nm beacon laser is designed as a pulse laser to perform synchronization, which is a passive Q-switching-type laser with about 10-kHz repetition frequency and 0.88-ns optical pulse width. Part of the laser is guided into a fast photodiode to convert it into an electrical pulse signal. This pulse signal and the GPS PPS signal from the satellite are fed into the TDC module of the transmitter. The acquired data are stored in the memory for further processing. Note that the time base of the TDC module is synchronized with that of the QKD photon-modulation module because they share a common clock.

In the receiver, part of the 532-nm laser beam is sent to a single-photon detector. The output signal of the single-photon detector, together with the electrical output pulses of the four single-photon detectors and the GPS PPS signal, is fed into a TDC. The acquired data are stored in the computer for further processing.

The time synchronization between the satellite and the ground can be divided into two steps. First, according to the predicted flight time of the light and the GPS PPS signal, the synchronization laser pulse sequence that is received on the ground can be matched with the satellite. Second, on the basis of the result of the first step, the time between the satellite and the ground is synchronized. We observe a typical temporal distribution of QKD photons with a standard deviation around 500 ps (Extended Data Fig. 5). A signal time window of 2 ns is used. Only events in the time window are valid.

Measuring the far-field pattern. Before the launch of the satellite, we measured the far-field pattern of the 850-nm laser in a thermal-vacuum test to simulate the in-orbit environment. Using a beam analyser, the divergence is measured to be 8 μrad × 11 μrad. The result is shown as Extended Data Fig. 5.

After the launch of the satellite, we could not measure the far-field profile directly as in the ground test. Alternatively, we adopted a scanning method,

measuring the intensity distribution of the 850-nm photons as a function of the pointing angle of the transmitter. The profile that we obtained is shown in Extended Data Fig. 5. Such a complete scan usually took a few minutes. Because the satellite is fast-moving, the satellite-to-ground distance and the atmospheric conditions vary with time. Atmospheric turbulence can be fast and can occur within a scanning cycle, which can distort the scanning plot. We observe that the result of the in-orbit test are qualitatively consistent with those from the ground test (Extended Data Fig. 5).

Experimental procedure. The experimental instruction and data process of satellite-to-ground QKD is shown in Extended Data Fig. 6. Six systems work together to implement the QKD experiment, including the scientific experiment planning centre, the ground support centre, the ground tracking telemetry and command centre, the optical ground station and the satellite platform with the payloads.

The satellite-to-ground QKD procedure is as follows (Extended Data Fig. 6). First, the experiment planning centre arranged the experiment, if the following conditions are guaranteed: (a) the calculated maximum elevation angle of the satellite to the ground station is greater than 25° (on the basis of predicted satellite orbits); and (b) the weather is forecasted to be clear and sunny. If so, instruction sequence files for the satellite are made and sent to the ground support centre. The instruction sequence file, the predicted curve data file and the polarization base compensation curve file for the motorized HWP are sent to the optical ground stations.

Second, the instruction file is translated to a coding file at the ground support centre and then sent to the ground tracking telemetry and command centre for upload to the satellite.

Third, the satellite platform and the payloads along with the optical ground station execute the instructions to transmit QKD photons from satellite to ground as follows:

(a) The satellite starts to change the pointing mode from geocentric to ground-station centric 10 min before entering the shadow zone. When the satellite exceeds an elevation angle of 5° from the horizon plane of the ground station, a pointing accuracy of better than 0.5° is achieved. At the same time, system initialization of the payloads is set.

(b) Before the satellite appears above the horizon, the telescope at the ground station activates its beacon laser at an elevation angle of 10° above the horizon to wait for the satellite. Once the elevation angle of the satellite to the ground station is more than 10°, open-loop pointing according to the predicted orbit is automatically executed. Meanwhile, the receiver at the ground station initiates data recording and starts to rotate the motorized HWP according to the polarization base compensation curve file.

(c) After reaching an elevation angle of 10° above the horizon, the satellite is fully covered by the beacon laser (671 nm) at the ground station. When the coarse-tracking camera of the optical transmitter obtains an image of the ground beacon laser, the APT is initiated to precisely track the ground beacon laser. At the same time, the beacon laser of the optical transmitter (532 nm) points towards the ground station.

(d) When the ground station receives the beacon laser from the optical transmitter, the APT control begins to precisely track the satellite beacon laser. Bidirectional tracking and locking between the transmitter and receiver is then achieved.

(e) At an elevation angle of about 15°, the satellite begins to read the random numbers and modulate the lasers for the decoy-state protocol. Both the satellite and the ground station record the GPS PPS signals and detect the 532-nm synchronous laser pulse for timing information. At the same time, the ground station records the output signals of the four single-photon detectors for the QKD measurement. All of the data are stored.

(f) When the satellite reaches an elevation angle of approximately 10° on its descent, the transmission of QKD photons and the tracking loop are terminated.

(g) After the transmission of the photons, experiment data are stored for further processing.

Decoy-state protocol and key rates. In practical QKD with a lossy channel, the security can be undermined by a photon-number-splitting attack if an imperfect single-photon source is used. For security, we need to use the decoy-state method[28,29], which verifies the lower bound on the single-photon counts.

The main idea of the decoy-state method is to change intensities randomly among several different values when sending out each pulse. Equivalently, we can regard pulses of different intensities as pulses from different sources. In this experiment, we use three different intensities: $\mu_2 = 0$ for vacuum, and μ_1 and μ_s for the decoy and signal states, respectively. In photon-number space, the state of the pulse from a non-vacuum source can be written as

$$\rho_l = \sum_k a_k^l |k\rangle\langle k|$$

where

$$a_k^l = \frac{\mu_l e^{-\mu_l}}{k!}$$

is the photon-number (k) distribution of the source of phase-randomized weak coherent states, with intensity $\mu_l = \mu_2 = 0$, $\mu_l = \mu_1$ and $\mu_l = \mu_s$ for vacuum, decoy and signal sources.

In practice, the number of pulses is finite and we have to consider the possible statistical fluctuations[28]. In such a case, we introduce an average value $\langle s_k \rangle$ for the counting rate of a k-photon state in a certain basis and use the constraints

$$S_l = \sum_k a_k^l \langle s_k \rangle$$

S_l is the directly observed value for the counting rate of source l in experiments and is regarded as a known value, but we need the average values $\langle S_l \rangle$ to calculate the secure final key rate. In general, any average value $\langle A \rangle$ can be related to its observed value A, with a fixed failure probability ξ by

$$\langle A \rangle = A(1 + \delta)$$
$$\delta \in [-\delta_1(\xi), \delta_2(\xi)]$$
$$\langle \underline{A} \rangle = A[1 - \delta_1(A, \xi)]$$
$$\langle \overline{A} \rangle = A[1 + \delta_2(A, \xi)]$$

where the under- and overbars indicate upper and lower bounds, respectively. With these preparations, we can determine a lower bound on the counting rate of a single-photon pulse $\underline{s_1}$, given the observed values of S_l in each basis. Similarly, given the observed values of error E_l, we can determine an upper bound on bit-flip error rate of a single-photon pulse in each basis and hence an upper bound on the phase-flip error rate $\overline{e_1^{ph}}$. Finally, we can calculate the secure final key rate per emissive pulse:

$$R = p_{\mu_s}\{a_1' \underline{s_1}[1 - H(\overline{e_1^{ph}})] - f S_{\mu_s} H(E_{\mu_s})\}$$

where f is the error correction inefficiency, $H(x) = -x\log_2(x) - (1-x)\log_2(1-x)$ is the binary Shannon entropy function, $a_1' = \mu_s e^{-\mu_s}$ and E_{μ_s} is the observed error rate for source intensity μ_s.

The values of the parameters used in the experiment are listed in Extended Data Table 3. We send out 1.36×10^{10} pulses in the whole experiment. The results of the experiment are listed in Extended Data Table 4; all data listed except Y_0 are results after basis correction.

Setting the failure probability to $\xi = 10^{-9}$ and the error correction inefficiency to $f = 1.4742$, as in our actual key-distillation system, we find a secure final key rate of $R = 1.38 \times 10^{-5}$, corresponding to 377,100 final keys if we had used the Chernoff bound[32].

We can also consider higher-level security by taking into consideration the uncertainties of the intensity of the source light[33]. Here we have both the light-intensity uncertainties and the statistical fluctuation. According to the experimental data, we know that $\sigma < 5\%$, and we set the failure probability to 10^{-9} with a Chernoff bound for the statistical fluctuation. We obtain a secure final key rate of $R = 1.10 \times 10^{-5}$, corresponding to 300,939 final keys.

Data availability. The data that support the findings of this study are available from the corresponding authors on reasonable request.

32. Curty, M. *et al.* Finite-key analysis for measurement-device-independent quantum key distribution. *Nat. Commun.* **5,** 3732 (2014).
33. Wang, X.-B., Yang, L., Peng, C.-Z. & Pan, J.-W. Decoy-state quantum key distribution with both source errors and statistical fluctuations. *New J. Phys.* **11,** 075006 (2009).

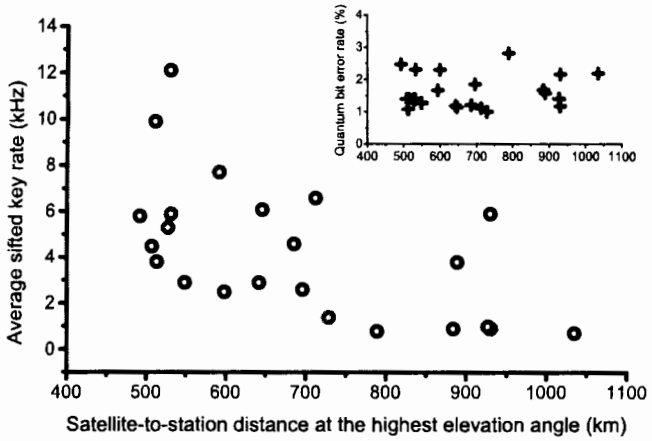

Extended Data Figure 1 | Summary of the QKD data obtained for 23 different days. The *x* axis is the shortest satellite-to-station distance, which occurs at the highest elevation angle and varies for different days. The *y* axis is the average sifted key rate that is obtained over the 273-s orbit. The inset shows the quantum bit error rate.

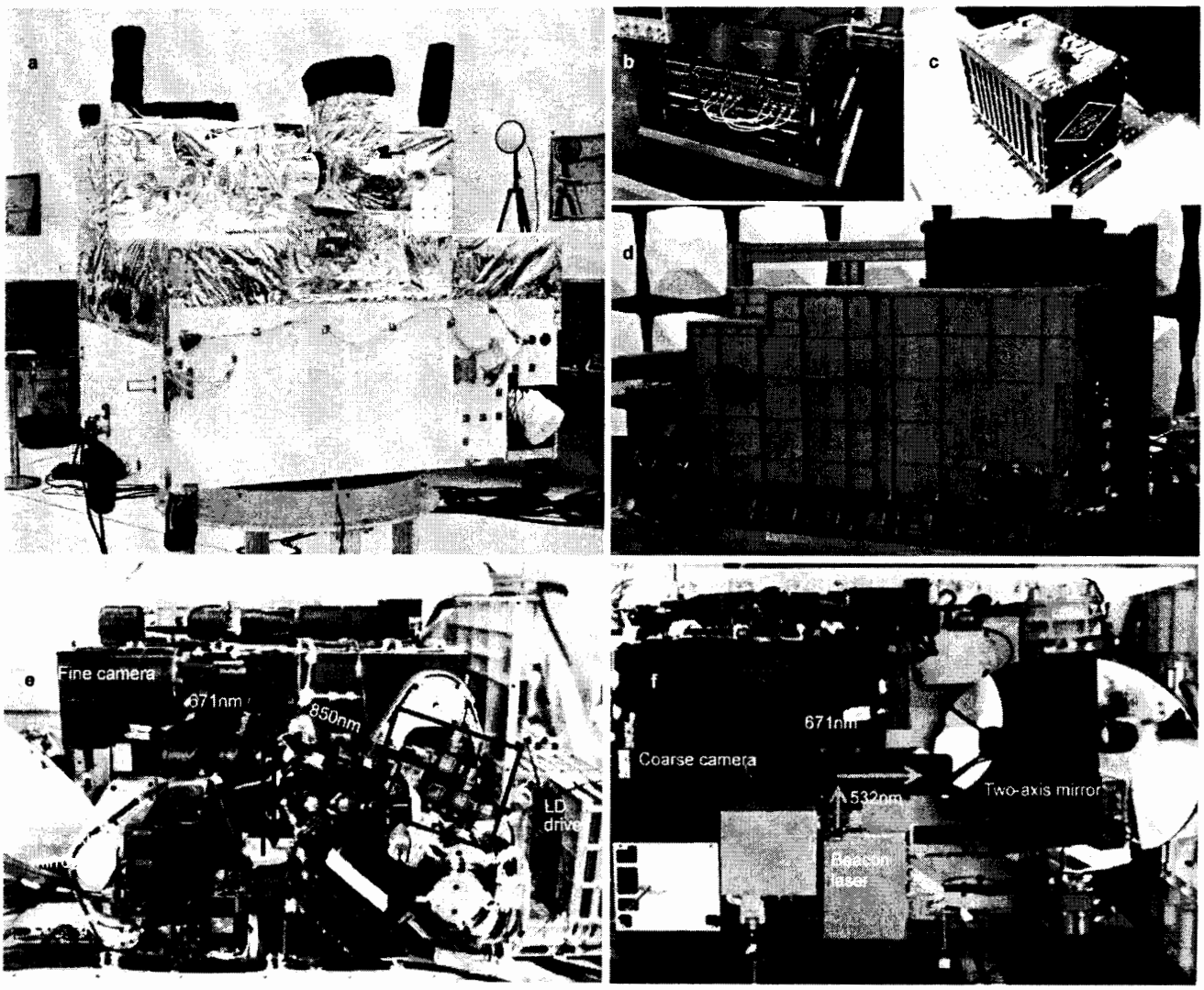

Extended Data Figure 2 | The Micius satellite and the payloads. **a**, A full view of the Micius satellite before being assembled into the rocket. **b**, The experimental control box. **c**, The APT control box. **d**, The optical transmitter. **e**, Left side view of the optical transmitter optics head. **f**, Top side view of the optical transmitter optics head.

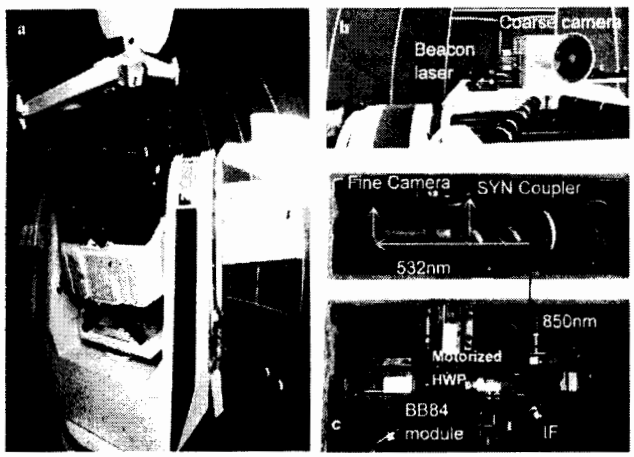

Extended Data Figure 3 | Hardware at Xinglong ground station. a, The two-axis gimbal telescope. **b**, Beacon laser and coarse camera. **c**, One of the two layers of the optical receiver box.

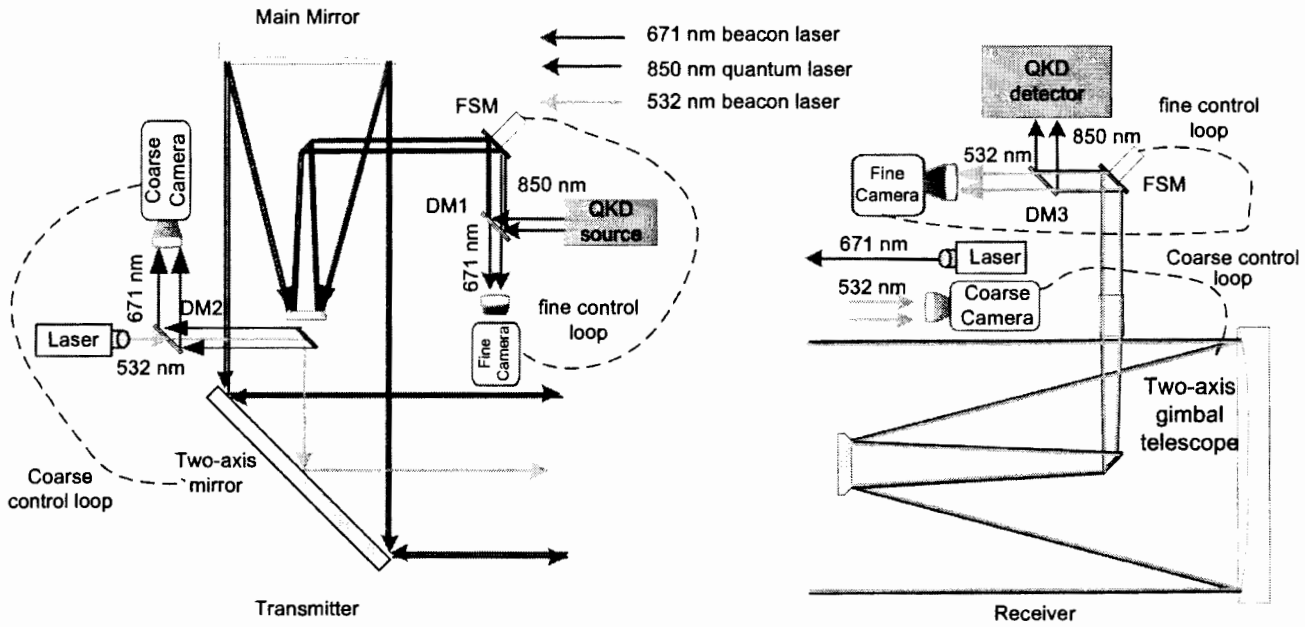

Extended Data Figure 4 | Sketch of the tracking systems on the satellite and at the ground station. DM1: dichroic mirror transmitting 671-nm light and reflecting 850-nm light. DM2: transmitting 532-nm light; reflecting 671-nm light. DM3: transmitting 532-nm light; reflecting 850-nm light.

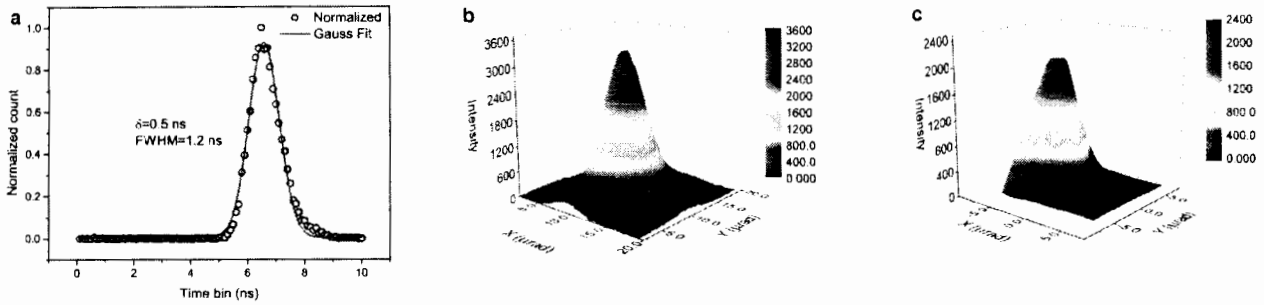

Extended Data Figure 5 | A typical temporal distribution of 850-nm photons and the measured far-field pattern. a, A typical temporal distribution of 850-nm photons after the time synchronization process. The data measurement time is 1 s. Each time bin is 100 ps. The counts are normalized and a variance of $\delta = 0.5$ ns is obtained with Gaussian fitting. **b**, Far-field pattern measured from the thermal-vacuum test on the ground. The divergence angles (full angle at $1/e^2$ maximum) are 8 μrad for the X axis and 11 μrad for the Y axis. **c**, Far-field pattern measured from the satellite-to-ground scanning test. The divergence angles (full angle at $1/e^2$ maximum) are 9 μrad for the X axis and 11 μrad for the Y axis.

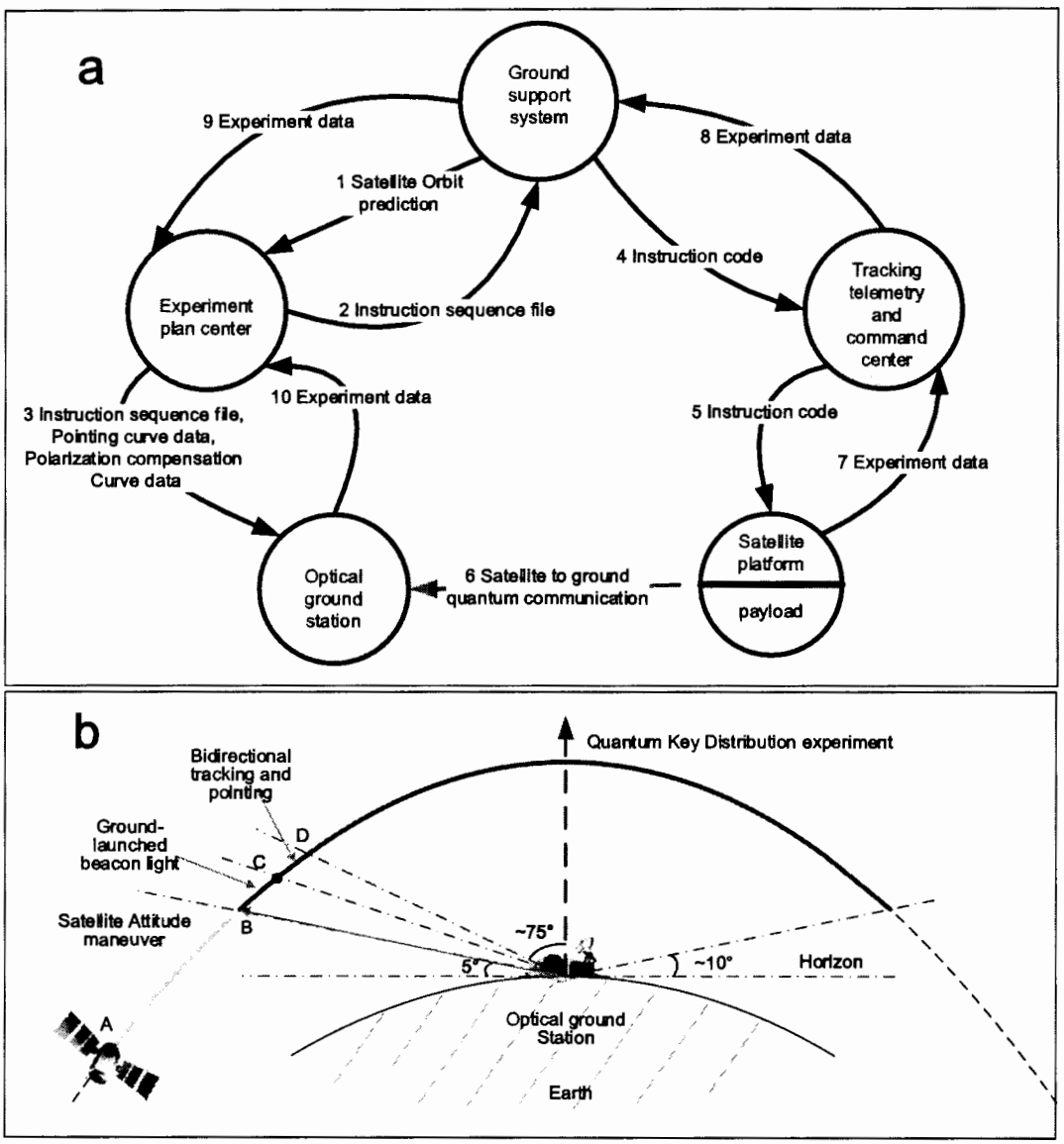

Extended Data Figure 6 | The experimental procedure. a, Instruction and data processes. **b**, Tracking and QKD processes during an orbit.

Extended Data Table 1 | Performance of the APT systems

Components		Transmitter terminal	Receiver terminal
Coarse pointing mechanism	Type	Two-axis gimbal mirror	Two-axis gimbal mount
	Tracking range	Azimuth:±5 ° Elevation: ±5 °	Azimuth:-270 °~+270 ° Elevation:-5 °~+95 °
Coarse camera	Type	CMOS	CCD
	Field of view	2.3 ° × 2.3 °	0.33 ° × 0.33 °
	Pixels & frame rates	1024 × 1024 & 11 Hz 512 × 512 & 40 Hz	512 × 512 & 56 Hz
Fine pointing mechanism	Type	PZT fast steering mirror	Voice-oil fast steering mirror
	Tracking range	±0.8 mrad	±17.5 mrad
Fine camera	Field of view	0.64 mrad × 0.64 mrad	1.3 mrad × 1.3 mrad
	Pixels & frame rates	60 × 60 & 2000 Hz	128 × 128 & 212 Hz
Beacon laser	Power	160 mW	2.7 W
	Wavelength	531.9 nm	671 nm
	Divergence	1.25 mrad	0.9 mrad
Tracking error (1δ)		0.6~1.5 μrad	1~2 μrad

Extended Data Table 2 | QKD data of 23 different orbits from 23 September 2016 to 22 May 2017

Date	Highest altitude angle (°)	Shortest distance (km)	Peak sifted key rate (kHz)	Average sifted key rate (kHz)	Quantum bit error rate
23/09/2016	67.35	527.07	22.1	5.3	1.39 %
29/09/2016	54.25	591.56	24.1	7.7	1.67 %
09/10/2016	28.67	930.2	2.7	0.9	2.16 %
10/10/2016	28.87	926.82	2.1	1.0	1.41 %
19/12/2016	47.79	645.08	14.1	6.1	1.14 %
04/01/2017	43.4	685.04	10.8	4.6	1.21 %
06/01/2017	71.68	513.46	11.1	3.8	1.40 %
12/01/2017	35.8	788.19	2.1	0.8	2.82 %
01/12/2016	24.99	1034.66	1.2	0.7	2.18 %
13/02/2017	44.5	695.76	13.9	2.6	1.85 %
14/02/2017	85.7	507.00	13.6	4.5	1.39 %
21/02/2017	29.64	929.67	9.0	5.9	1.17 %
08/03/2017	79.6	511.35	21.4	9.9	1.08 %
11/03/2017	42.69	711.94	15.6	6.6	1.11 %
20/04/2017	82.85	491.92	11.5	5.8	2.48 %
27/04/2017	40.04	728.20	6.1	1.4	1.00 %
07/05/2017	68.24	530.33	40.2	12.1	1.39 %
11/05/2017	54.85	598.09	17.2	2.5	2.30 %
14/05/2017	49.45	641.65	7.9	2.9	1.19 %
17/05/2017	65.24	548.41	11.4	2.9	1.27 %
18/05/2017	31.49	883.23	1.9	0.9	1.68 %
20/05/2017	70.34	531.05	17.8	5.9	2.31 %
22/05/2017	31.31	887.84	6.5	3.8	1.58 %

Extended Data Table 3 | Performance of the transmitter and receiver

Components			Data
Transmitter (weak coherent pulses)	Telescope diameter		300 mm
	Wavelength		848.62 nm
	Offset of wavelength		<0.006 nm
	Linewidth (3 dB)		~0.1 nm
	Pulse width (FWHM)		~200 ps
	Polarization contrast ratio		>225:1
	Divergence		~10 μrad
	Frequency		100 MHz
	Mean photon number	Signal	0.8
		Decoy	0.1
		Vacuum	0
	Probability	Signal	0.5
		Decoy	0.25
		Vacuum	0.25
Receiver	Telescope diameter		1 m
	Optical efficiency @850nm		~16%
	Detector efficiency @850nm		~50%
Synchronization	Laser pulse (FWHM)		0.88 ns
	Laser frequency		10.7 kHz
Synchronization jitter of transmitter and receiver (1δ)			~0.5 ns

Extended Data Table 4 | Observed data for a single orbit at Xinglong station

T (s)	Y_0	S_{μ_s}	S_{μ_l}	E_{μ_s}	E_{μ_l}	R_{pulse}	R_{total}
273	5.89×10^{-7}	1.22×10^{-4}	1.52×10^{-5}	1.1 %	1.8 %	1.10×10^{-5}	300939

T is the effective time for QKD, Y_0 is the yield for the vacuum states, s_l is the counting rate for a source of intensity μ_l, E_l is the quantum bit error rate of the states of intensity μ_l, R_{pulse} is final key rate per clock cycle and R_{total} is the total final key size of the experiment.

REPORT

CHEMICAL PHYSICS

In the Copenhagen interpretation of quantum mechanics, a particle is fully described by its complex wave function Ψ, which is characterized by both an amplitude and phase. However, only the square modulus of the wave function, $|\Psi|^2$, can be directly observed (*1*, *2*). Recent developments in attosecond technology based on electron-ion recollision (*3*) have provided experimental tools for the imaging of the electronic wave function (not its square) in bound states or ionization continua. High-harmonic spectroscopy on aligned molecules was used to reconstruct the highest-occupied molecular orbital of nitrogen (*4*, *5*) and to observe charge migration (*6*). Strong-field tunneling was used to measure the square modulus of the highest-occupied molecular orbital for selected molecules (*7*). Furthermore, recollision holography (*8*, *9*) permitted a measurement of the phase and amplitude of a continuum electron generated in an intense laser field.

Complementary to recollision-based measurements, photoelectron spectroscopy with attosecond extreme ultraviolet (XUV) pulses has also measured photoelectron wave packets in continuum states (*10*–*16*) by exploiting quantum interferences (*17*–*19*). However, decomposition of the wave function of an ejected photoelectron into angular momentum eigenstates with a fully characterized amplitude and phase is more difficult. First, in general, a one-photon transition with linearly polarized light generates two orbital angular momentum (ℓ) states, according to the selection rule $\Delta\ell = \pm 1$. Second, because the initial state has a $(2\ell + 1)$-fold degeneracy (labeled by m, the magnetic quantum number) and because m is conserved for interactions with linearly polarized light, photoelectron waves with a range of m are produced. Hence, the photoelectron momentum distribution contains a sum of contributions from different initial states, each of which is a coherent sum of different angular momentum components, making it difficult to decompose the continuum state into individual angular momentum components (*20*–*22*).

Here we preferentially create an almost pure f-wave continuum wave function with $m = 0$ in neon by using an attosecond XUV pulse train synchronized with an infrared (IR) laser pulse through the process of high-harmonic generation. The isolation of the f-wave with $m = 0$ is attributed to the XUV excitation to a resonant bound state that is Stark-shifted by the IR field. By adding an additional coherent pathway that produces an isotropic electron wave, we create a hologram and reveal the alternating sign of the lobes of the f-wave. By controlling the phase of the interfering pathways with attosecond precision, we are able to determine the amplitudes and phases of all six partial-wave components that contribute to the continuum wave function.

The experimental setup is described in detail in the supplementary materials (SM). An 800-nm wavelength laser pulse with a 35-fs duration is focused onto an argon gas jet, producing high-harmonic emission that we label "XUV." In the frequency domain, the emission has peaks at odd-integer multiples of the driving laser frequency. In the time domain, the XUV pulse is composed of a train of attosecond pulses. The high-harmonic emission is focused onto a second gas jet containing neon gas. The neon atoms are excited and photoionized by different high-harmonic orders, and the resulting photoelectrons are recorded by a velocity map–imaging (VMI) spectrometer, which measures their two-dimensional (2D) projection onto a detection plane (*23*). For the phase-resolved measurements, we generate an XUV spectrum that contains both even and odd harmonics, using both 800- and 400-nm driving laser pulses (*24*). In both cases, part of the 800-nm pulse (called "IR") is also focused onto the neon gas, permitting resonant (1 + 1′)-photon, XUV + IR ionization and Stark-shifting of the resonant bound states (*25*). The two-color temporal control and stability of the experiment is <50 as.

We first consider the situation where the XUV is generated by 800 nm only (i.e., no 400-nm contribution). The XUV spectrum then consists of a comb of odd harmonics of the IR driver laser frequency (i.e., no even harmonics). Figure 1A shows the XUV + IR photoelectron momentum distribution for the ionization of neon that is measured under these conditions. At very low momentum, i.e., close to the ionization threshold, a six-fold angular structure is clearly observed. For comparison, an image recorded for helium under the same conditions is shown in Fig. 1B. This experiment may be viewed as the angular-resolved version of a previous study in helium by Swoboda *et al.* (*26*), in which the phase shift due to an intermediate resonance was mapped out. For neon, in Fig. 1A, the outer ring is produced through direct ionization by harmonic 15 (H15), whereas the inner structure results from (1 + 1′)-photon, H13 + IR ionization through the 3d intermediate resonance. The widths in the radial direction of all observed features are a consequence of the frequency bandwidth of the XUV and IR pulses (*27*).

Figure 1C shows an energy level diagram that rationalizes the experimental observations in neon. The XUV photon energy and the IR intensity create a resonance condition for H13 with the Stark-shifted 3d level (see SM). The addition of an IR photon enables (1 + 1′)-photon ionization, producing the central feature seen in Fig. 1A. In Fig. 1C, the atomic eigenstates are labeled with the usual atomic physics notation, i.e., with principal quantum number n and with the orbital angular momentum labeled as s ($\ell = 0$), p ($\ell = 1$), d ($\ell = 2$), and f ($\ell = 3$). A dipole transition between states changes ℓ by ±1. For neon ($1s^2 2s^2 2p^6$), the 2p→3d transition is dipole-allowed, and in the dipole approximation, the continuum electron resulting from XUV + IR ionization must have either p- or f-wave character. We show that the experimental results are consistent with a continuum electron wave function that is predominantly an f-wave with $m = 0$.

The amplitude of the six-fold structure is modulated when the relative delay between the XUV and the IR laser pulses is varied. This modulation is due to the interference between the resonant H13 + IR pathway and the nonresonant H15 − IR pathway (we use the notation H13 + IR and H15 − IR to denote two-photon pathways composed of one harmonic order plus or minus one infrared

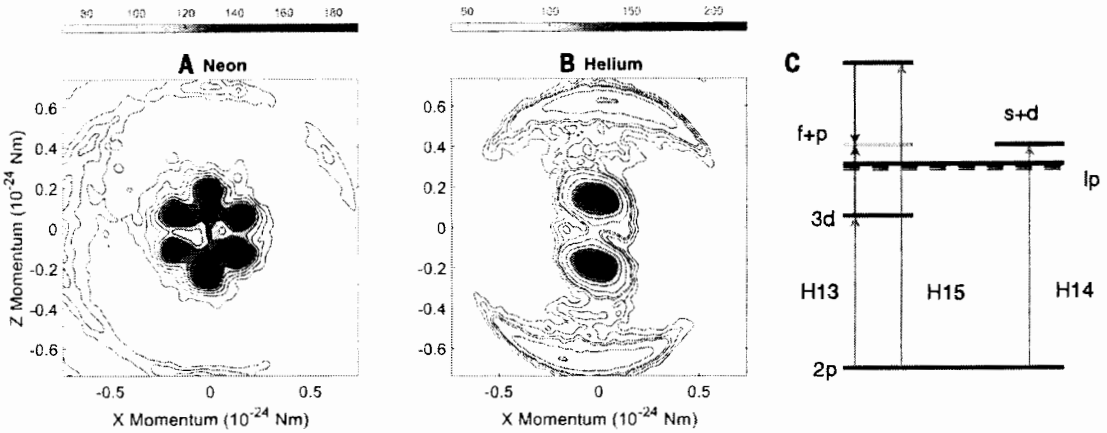

Fig. 1. Experimental velocity-map electron images. The observed photoelectron momentum distributions result from the ionization of (**A**) neon and (**B**) helium by an attosecond pulse train synchronized with the fundamental IR laser pulse. Both pulses were polarized along the vertical (z) axis. In both images, the outer rings are due to direct ionization by harmonics 15 (neon) and 17 (helium). The central feature in the neon image results from (1 + 1′)-photon, XUV + IR ionization via the 3d state. The slight left-right asymmetry arises from imperfections in the microchannel plate detector. An energy level diagram in (**C**) shows the levels that are relevant for understanding the neon experiment. The green line labels the six-fold low-energy feature seen in (A).

photon). The SM shows that the phase of the six-fold structure is different from that of the higher-order sidebands, consistent with the occurrence of a phase shift due to the 3d resonance. This result is consistent with the observations of Swoboda *et al.* (*26*) in helium.

Experimentally, the resonant excitation to the Stark-shifted 3d state can be confirmed by measurements of the photoelectron momentum distribution as a function of both the photon energy of the XUV and the IR laser intensity (0 to 4 × 10^{12} W/cm^2; see SM). At a given XUV photon energy, the six-fold structure is observed when the H13 photon energy matches the 2p→3d resonant energy plus the ponderomotive shift resulting from the IR laser intensity (see SM). However, when the XUV photon energy is larger than the Stark-shifted 2p→3d transition, the six-fold structure disappears into a broad distribution.

The initial 2p state of neon has three orthogonal orbitals, p_x, p_y, and p_z (we consider that in the experiment the laser is polarized along the z direction, and the photoelectron is detected in the xz plane). Ionization from each initial state should contribute to the final angular distributions. The three components of a continuum f-wave resulting from (1+1′)-photon ionization from the three p orbitals are illustrated in Fig. 2, along with their simulated VMI projections. It is clear that the six-fold structure of Fig. 1A corresponds only to the m = 0 case, which is the only orbital that displays the experimentally observed node in the horizontal direction (x direction). The dominance of the m = 0 channel is both notable and unexpected. Like the ground state, in the absence of the laser field, the m = 0 and m = ±1 components of the 3d resonance are degenerate. Our experiment thus suggests that a Stark shift of the 3d resonant state may be responsible for the selection of the m = 0 component. We show in the SM that the Stark shift and ionization rate may be different for m = 0 and m = ±1, causing only the m = 0 channel to be shifted into resonance. Figure S5 shows that, for a particular combination of XUV frequency and IR intensity, the contribution of photoelectrons produced through the m = 0 channel exceeds by an order of magnitude the contributions from the m = ±1 channels. This calculation was performed with a 3D time-dependent Schrödinger equation (TDSE) solver by using an effective potential for argon, not neon. As discussed in the SM, this calculation demonstrates the plausibility of m = 0 selection by the Stark shift, but the calculation must be done for a benchmarked neon potential.

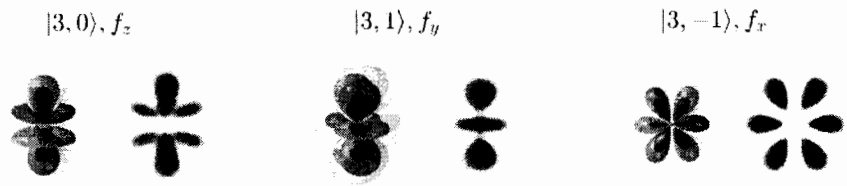

Fig. 2. Calculated continuum wave functions and predicted VMI projections. The individual wave functions for the possible f-wave components are shown to the left of the corresponding projections of the square of the wave function on a 2D plane. Quantization axis is along the vertical (z) axis. Only the m = 0 case (left) is consistent with the experiment, which always exhibits a node along the horizontal axis. The radial part of the wave functions was simulated with a Gaussian width to correspond to the experimental energy width of the VMI images; the radial information in the experiment is not used—only the angular distributions are used. $f_y = Im(|3,1\rangle + |3,-1\rangle)/\sqrt{2}$ and $f_x = Re(|3,1\rangle - |3,-1\rangle)/\sqrt{2}$.

We next modified the experiment by introducing a third, XUV-only, one-photon pathway to the final continuum state as a homodyne phase reference. Experimentally, this was done by adding the second harmonic of the 800-nm laser pulse to the high-harmonic generation process, resulting in the creation of both even and odd harmonics (*24*). Even-order harmonic H14 creates photoelectrons with the same energy as the H13 + IR and H15 − IR pathways (see Fig. 1C). Direct ionization from the 2p ground state by H14 produces s- and d-waves, which interfere with the predominant f-wave that is created by both (1 + 1′)-photon processes. By varying the relative delay between the XUV and IR pulses, the phases of the XUV + IR, (1 + 1′)-photon processes are altered, whereas the s- and d-waves are unaffected by the delay, providing a constant phase reference for the other channels.

Figure 3 shows measured photoelectron momentum distributions from neon at three different XUV-IR time delays. Compared with Fig. 1A, the lobes in the six-fold angular pattern alternate in intensity, and the intensity distribution is controlled by the XUV-IR delay. The alternating three-fold features can be rationalized in a simple picture by coherently adding an f-wave to an s-wave, or taking their difference, as illustrated in Fig. 3, while neglecting the p- and d-wave components.

The three VMI images shown in Fig. 3A are taken from a series of 100 images recorded at different XUV-IR time delays. These images were

binned into 8° angular sectors, and the counts in each sector were integrated to extract the angular distribution for each image. In Fig. 4A, we plot the observed electron angular distributions of the central structure as a function of the XUV-IR delay. The experimental results are compared to a model in which six possible spherical harmonics are added coherently and then projected onto the xz plane to simulate the VMI images. The total continuum wave function is written as

$$\psi(\theta,\phi) = A_s Y_{00} + A_d e^{i\phi_d} Y_{20} + (A_{p13} e^{i\phi_{p13}} Y_{10} + A_{f13} e^{i\phi_{f13}} Y_{30}) e^{i\omega_0 \tau} + (A_{p15} e^{i\phi_{p15}} Y_{10} + A_{f15} e^{i\phi_{f15}} Y_{30}) e^{-i\omega_0 \tau} \quad (1)$$

where the A's represent amplitudes of each partial wave contribution, ϕ are the corresponding phases, ω is the IR laser frequency, τ is the XUV-IR delay time, and $Y_{\ell m}(\theta, \phi)$ are spherical harmonics. The first two terms of the right side of the equation describe the one-photon ionization by H14 producing s- and d-waves, whereas the latter two terms (containing the dependence on the XUV-IR delay τ) result from the pathway through the 3d resonant state involving H13, and the direct ionization channel involving H15, both producing p- and f-waves. A fit of this model to the experimental data yields the results shown in Fig. 4B; the fitting parameters are listed in Table 1. To ensure that a global optimum was found, we employed a particle swarm optimization algorithm with 10^7 initial conditions. The amplitudes in Table 1 confirm the dominance of the f- and s-wave components over the respective p- and d-wave components that we have used in the discussion of Fig. 3.

As an additional check, we show in the SM that the partial-wave amplitudes and phases in Table 1 are consistent with several further experiments. One is the series of experiments that produced the data shown in Fig. 1A, which were recorded without H14 present; here the equal intensities of all six lobes can only be reproduced when the f- and p-waves are added with the relative phase and amplitude shown in Table 1. In a

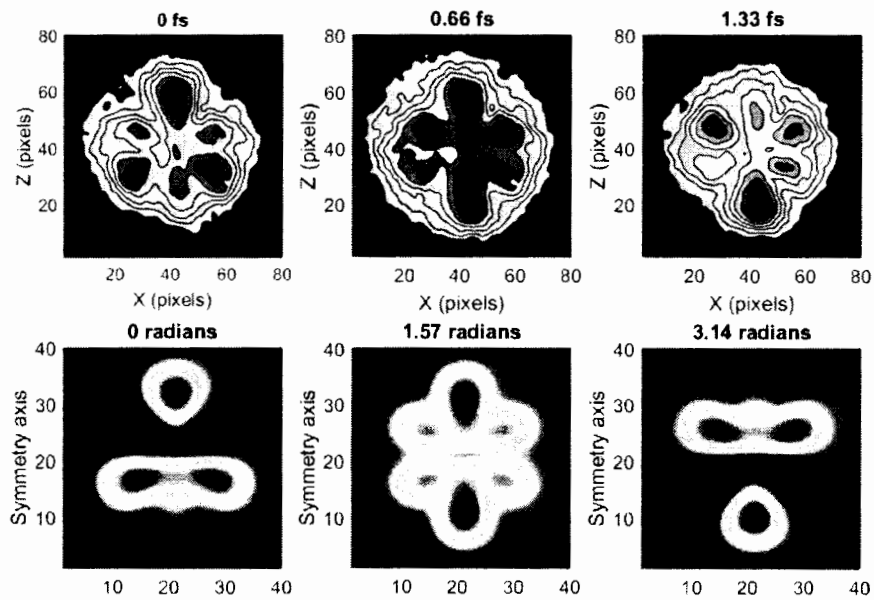

Fig. 3. Electron momentum angular distributions with three pathways. (**Top**) Experimental electron momentum distributions resulting from the ionization of neon via the three pathways (H13, H14, H15) shown in Fig. 1C. The polarization direction is vertical. (**Bottom**) Calculated images for a pure s-wave added to a pure f-wave (m = 0) with equal amplitudes, squared and projected onto a plane, to show that the experimental results are dominated by these two components. For simplicity (and as supported by the data in Table 1), the p- and d-wave contributions are not included. The s-wave component is produced by direct one-photon ionization with H14 and provides a phase reference for the other two interfering pathways. As the phase of the IR pulse is advanced by the times shown above each figure, the phase of the f-wave component is varied. The resulting interference introduces an up-down asymmetry in the momentum distribution that can be controlled by the IR phase.

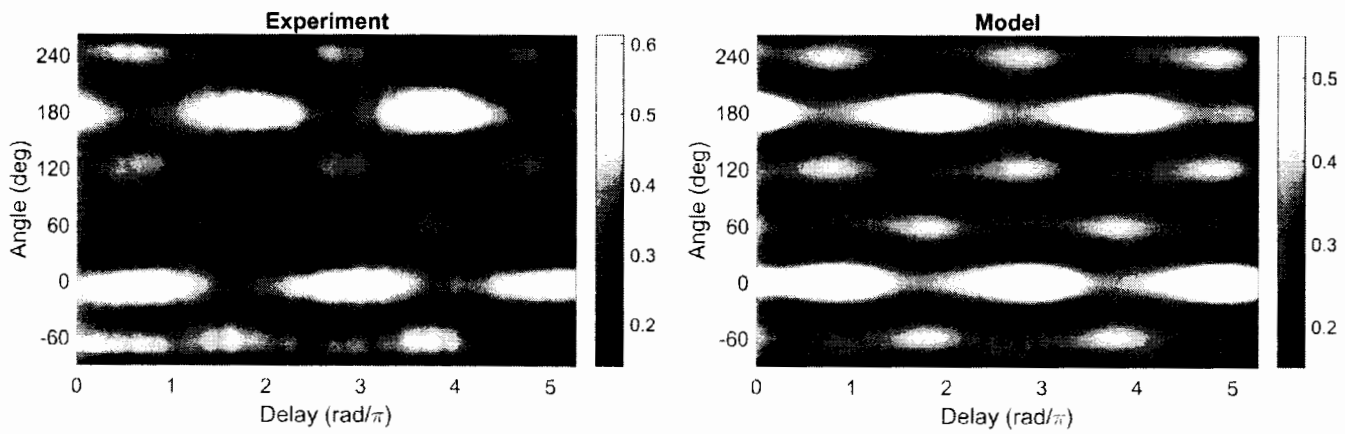

Fig. 4. Angular distribution of the central feature of the VMI images versus XUV-IR delay. Angle zero is defined as the upward direction in the VMI images, parallel to the polarization (z) axis. A delay of π radians corresponds to a delay of half an IR optical period (1.33 fs). (**Left**) Experimental data. (**Right**) Calculated angular distribution based on fitting a 12-parameter model (see Eq. 1) to the experimental data. The amplitudes and phases of each partial wave are listed in Table 1. The dominant pattern is reproduced: Alternating lobes at 0° and 180°, with minor lobes at −60°, 60°, 120°, and 240°. This pattern is associated with the six-fold structure of the dominant f-wave contribution.

Table 1. Parameters of the model fit. The experimental photoelectron angular distributions as a function of XUV-IR delay, shown in Fig. 4A, are fitted to a model composed of six partial waves (see Eq. 1). The amplitudes and phases of each partial wave are listed. The amplitudes are normalized so that the sum of their squares equals one. The phase of the s-wave is defined as zero. ϕ_0 represents an arbitrary common phase that determines time zero. The column labeled "Amplitude^2" is the square of the values in the "Amplitude" column. Errors shown are the range of each parameter such that the residual least-squares error between the model and the experiment increases by 10%.

Fitting parameter	Amplitude	Amplitude^2	Phase (rad)
A_s	$0.83^{+0.04}_{0.04}$	0.697	0
A_{p13}	$0.16^{+0.05}_{0.05}$	0.024	$0.54^{+0.41}_{0.34} + \phi_0$
A_{p15}	$0.15^{+0.05}_{0.04}$	0.022	$1.93^{+0.41}_{0.42} - \phi_0$
A_d	$0.10^{+0.05}_{0.06}$	0.011	$1.57^{+0.30}_{0.30}$
A_{f13}	$0.32^{+0.04}_{0.04}$	0.104	$4.16^{+0.19}_{0.20} + \phi_0$
A_{f15}	$0.39^{+0.03}_{0.04}$	0.151	$5.04^{+0.16}_{0.16} - \phi_0$

further experiment, no IR was present, and the inner structure was produced by H14 alone; here the observed angular distribution is in approximate agreement with the relative phase and amplitude of the s- and d-waves in Table 1.

We have shown that, by combining coherent photoionization pathways through a Stark-shifted resonant state, we can create almost pure f-waves with a single magnetic quantum number $m = 0$. The addition of a direct photoionization pathway producing predominantly an s-wave provides a constant phase reference that allows a determination of the phase of the f-wave lobes. By varying the relative phase of the pathways, we can control the direction in which the electrons emanate from the atom, and we can verify the quantum phase of the lobes of the f-wave. We have spatially imaged the angular structure of the continuum wave function and coherently interfered it using a holographic reference composed largely of an isotropic s-wave, leading to the determination of the sign of the quantum wave function. This is a form of coherent control, in which the parity and direction of the electrons can be controlled (*13*, *19*).

In addition, the fitting of a model to the complete experimental data set allows us to determine the exact makeup of the total continuum wave function. In particular, we can determine the amplitude and phase of each partial-wave component. In photoionization parlance, this is a "complete" experiment (*20*).

We have implemented a number of novel approaches, such as a sophisticated two-color interference experiment with careful use of both even and odd harmonics and the use of Stark-tuning to include or exclude desired quantum pathways. These new tools in the attosecond toolbox may allow us to study more complex systems. For example, can we apply a similar approach to a molecule? By exploiting rotational wave packets, will it be possible to determine both the amplitude and phase of transition moments in the molecular frame?

If the photon energy of the XUV can be tuned widely to select a particular intermediate quantum state, our method allows the measurement of phase-resolved orbital images of other states and in different atoms. For instance, if the electron is excited from a lower-lying level to a doubly excited state, dynamical changes in the amplitude and phase resulting from electron correlation can be imaged directly with attosecond time resolution.

REFERENCES AND NOTES

1. H. Wimmel, *Quantum Physics and Observed Reality: A Critical Interpretation of Quantum Mechanics* (World Scientific, Singapore, 1992).
2. A. S. Stodolna *et al.*, *Phys. Rev. Lett.* **110**, 213001 (2013).
3. H. Niikura *et al.*, *Nature* **417**, 917–922 (2002).
4. J. Itatani *et al.*, *Nature* **432**, 867–871 (2004).
5. S. Haessler *et al.*, *Nat. Phys.* **6**, 200–206 (2010).
6. P. M. Kraus *et al.*, *Science* **350**, 790–795 (2015).
7. M. Meckel *et al.*, *Science* **320**, 1478–1482 (2008).
8. M. Meckel *et al.*, *Nat. Phys.* **10**, 594–600 (2014).
9. D. Ray *et al.*, *Phys. Rev. Lett.* **100**, 143002 (2008).
10. V. Gruson *et al.*, *Science* **354**, 734–738 (2016).
11. S. Haessler *et al.*, *Phys. Rev. A* **80**, 011404 (2009).
12. K. T. Kim *et al.*, *Phys. Rev. Lett.* **108**, 093001 (2012).
13. G. Laurent *et al.*, *Phys. Rev. Lett.* **109**, 083001 (2012).
14. J. Mauritsson *et al.*, *Phys. Rev. Lett.* **105**, 053001 (2010).
15. T. Remetter *et al.*, *Nat. Phys.* **2**, 323–326 (2006).
16. A. Rouzée *et al.*, *J. Phys. At. Mol. Opt. Phys.* **47**, 124017 (2014).
17. J. Cooper, R. N. Zare, *J. Chem. Phys.* **48**, 942–943 (1968).
18. J. Cooper, R. N. Zare, in *Atomic Collision Processes*, G. Geltman, K. T. Mahanthappa, W. E. Brittin, Eds. (Lectures in Theoretical Physics, Gordon and Breach, 1969), vol. XIc, pp. 317–337.
19. Y.-Y. Yin, C. Chen, D. S. Elliott, A. V. Smith, *Phys. Rev. Lett.* **69**, 2353–2356 (1992).
20. U. Becker, *J. Electron Spectrosc. Relat. Phenom.* **96**, 105–115 (1998).
21. J. C. Hansen, J. A. Duncanson, R.-L. Chien, R. S. Berry, *Phys. Rev. A* **21**, 222–233 (1980).
22. K. L. Reid, *Annu. Rev. Phys. Chem.* **54**, 397–424 (2003).
23. A. T. J. B. Eppink, D. H. Parker, *Rev. Sci. Instrum.* **68**, 3477–3484 (1997).
24. N. Dudovich *et al.*, *Nat. Phys.* **2**, 781–786 (2006).
25. E. B. Saloman, C. J. Sansonetti, *J. Phys. Chem. Ref. Data* **33**, 1113–1158 (2004).
26. M. Swoboda *et al.*, *Phys. Rev. Lett.* **104**, 103003 (2010).
27. N. Dudovich, D. Oron, Y. Silberberg, *Phys. Rev. Lett.* **88**, 123004 (2002).

nature

LETTERS

In classical electromagnetism, the Lorentz force for a particle of charge q moving with velocity $\mathbf{v}$ in a magnetic field $\mathbf{B}$ is $\mathbf{v} \times q\mathbf{B}$. In the Hamiltonian formulation of quantum mechanics, where potentials play a more central role than fields, the single-particle Hamiltonian is $\mathcal{H} = \hbar^2(\mathbf{k} - q\mathbf{A}/\hbar)^2/2m$, where $\mathbf{A}$ is the vector potential giving rise to the field $\mathbf{B} = \nabla \times \mathbf{A}$, $\hbar\mathbf{k}$ is the canonical momentum and m is the mass. In both formalisms, only the products $q\mathbf{B}$ and $q\mathbf{A}$ are important. To generate a synthetic magnetic field $\mathbf{B}^*$ for neutral atoms, we engineered a Hamiltonian with a spatially dependent vector potential $\mathbf{A}^*$ producing $\mathbf{B}^* = \nabla \times \mathbf{A}^*$.

The quantum mechanical phase is the relevant and significant quantity for charged particles in magnetic fields. A particle of charge q travelling along a closed loop acquires a phase $\phi = 2\pi\Phi_B/\Phi_0$ due to the presence of magnetic field $\mathbf{B}$, where Φ_B is the enclosed magnetic flux and $\Phi_0 = h/q$ is the flux quantum. A similar path-dependent phase, the Berry's phase[13], is the geometric phase acquired by a slowly moving particle adiabatically traversing a closed path in a Hamiltonian with position-dependent parameters. The Berry's phase depends only on the geometry of the parameters along the path, and is distinct from the dynamic contribution to the phase, which depends upon the speed of the motion.

The close analogy with the Berry's phase implies that properly designed position-dependent Hamiltonians for neutral particles can simulate the effect of magnetic fields on charged particles. We created such a spatially varying Hamiltonian for ultracold atoms by dressing them in an optical field that couples different spin states. The appropriate spatial dependence can originate from the laser beams' profile[10,14,15] or, as here, from a spatially dependent laser–atom detuning[16]. An advantage of this optical approach over rotating gases is that the synthetic field exists at rest in the laboratory frame, allowing all trapping potentials to be time-independent.

The large synthetic magnetic fields accessible by this approach make possible the study of unexplored bosonic quantum-Hall states, labelled by the filling factor $\nu = \Phi_B/\Phi_0$, the ratio of atom number to the number of flux quanta. The outstanding open questions in quantum-Hall physics centre on systems whose elementary quasiparticle excitations are anyons: neither bosons nor fermions. In some cases these anyons may be non-abelian, meaning that moving them about each other can implement quantum gates, which makes non-abelian anyons of great interest for this 'topological' quantum computation[17]. In electronic systems, the observed $\nu = 5/2$ quantum-Hall state may be such a system, but its true nature is still uncertain[18]. In contrast, the $\nu = 1$ bosonic quantum-Hall state with contact interactions has the same non-abelian anyonic excitations as the $\nu = 5/2$ state in electronic systems is hoped to have[19].

To engineer a vector potential $\mathbf{A}^* = A_x^*\hat{x}$, we illuminated a ^{87}Rb Bose–Einstein condensate (BEC) with a pair of Raman laser beams with momentum difference along $\hat{x}$ (Fig. 1a). These coupled together the three spin states, $m_F = 0$ and ± 1, of the $5S_{1/2}$, $F = 1$ electronic ground state (Fig. 1b), producing three dressed states whose energy–momentum dispersion relations $E_j(k_x)$ are experimentally tunable. Example dispersions are illustrated in Fig. 1c. The lowest of these, with minimum at $k_{\min}$, corresponds to a term in the Hamiltonian associated with the motion along $\hat{x}$, namely $\mathcal{H}_x^* \approx \hbar^2(k_x - k_{\min})^2/2m^* = \hbar^2(k_x - q^*A_x^*/\hbar)^2/2m^*$, where A_x^* is an engineered vector potential that depends on an externally controlled Zeeman shift for the atom with synthetic charge q^*, and m^* is the effective mass along $\hat{x}$. To produce the desired spatially dependent $A_x^*(y)$ (see Fig. 1d), generating $-B^*\hat{z} = \nabla \times \mathbf{A}^*$, we applied a Zeeman shift that varied linearly along $\hat{y}$. The resulting B^* was approximately uniform near $y = 0$, at which point $A_x^* = B^*y$. (Here, the microscopic origin of the synthetic Lorentz force[20] was optical along $\hat{x}$, depending upon the velocity along $\hat{y}$; the force along $\hat{y}$ was magnetic, depending upon the $\hat{x}$ velocity.) In this way, we engineered a Hamiltonian for ultracold atoms that explicitly contained a synthetic magnetic field, with vortices in the ground state of a BEC. This is distinctly different from all existing experiments, where vortices are generated by phase imprinting[21,22], rotation[7–9], or a combination thereof[23]. Each of these earlier works presents a different means of imparting angular momentum to the system yielding rotation. Figure 1e shows an experimental image of the atoms with $B^* = 0$. Figure 1f, with $B^* > 0$, shows vortices. This demonstrates an observation of an optically induced synthetic magnetic field.

We created a ^{87}Rb BEC in a 1,064-nm crossed dipole trap, loaded into the lowest-energy dressed state[21] with atom number N up to

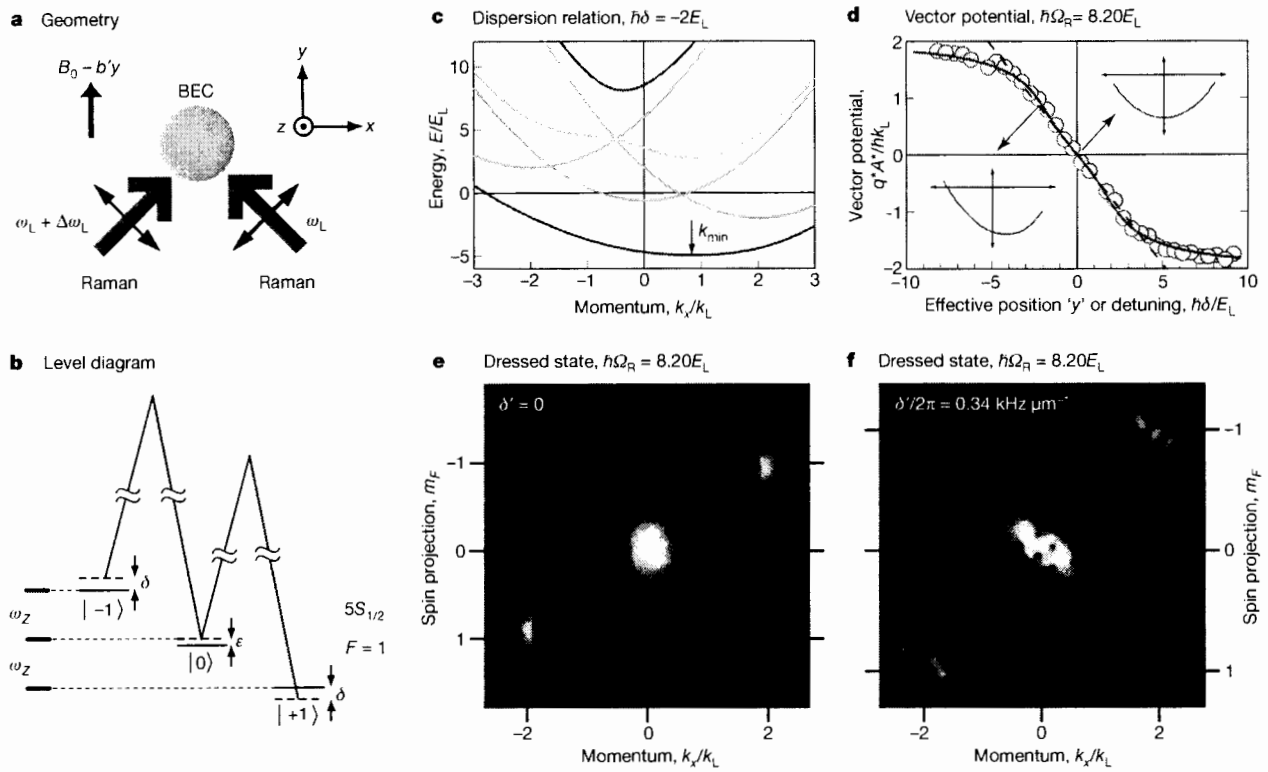

Figure 1 | Experiment summary for synthesizing magnetic fields. a, The BEC is in a crossed dipole trap in a magnetic field $B = (B_0 - b'y)\hat{y}$. Two Raman beams propagating along $\hat{y} \mp \hat{x}$ (linearly polarized along $\hat{y} \pm \hat{x}$) have frequencies ω_L and $\omega_L + \Delta\omega_L$. **b**, Raman coupling scheme within the $F = 1$ manifold: ω_Z and ε are the linear and quadratic Zeeman shifts, and δ is the Raman detuning. **c**, Energy–momentum dispersion relations. The grey curves represent the states without Raman coupling; the three coloured curves represent $E_j(k_x)$ of the dressed states. The arrow indicates the minimum at k_{min}. **d**, Vector potential $q^*A_x^* = \hbar k_{min}$ versus Raman detuning δ. The insets show the dispersion $E_1(k_x)$ for $\hbar\delta = 0$ (top inset) and $-2E_L$ (bottom inset). **e**, **f**, Dressed BEC imaged after a 25.1-ms TOF without (**e**) and with (**f**) a gradient. The spin components $m_F = 0$ and ± 1 separate along $\hat{y}$ owing to the Stern–Gerlach effect.

2.5×10^5, and a Zeeman shift $\omega_Z/2\pi = g\mu_B B/h \approx 2.71$ MHz, produced by a real magnetic bias field $B\hat{y}$. The $\lambda = 801.7$ nm Raman beams propagated along $\hat{y} \pm \hat{x}$ and differed in frequency by a constant $\Delta\omega_L \simeq \omega_Z$, where a small Raman detuning $\delta = \Delta\omega_L - \omega_Z$ largely determined the vector potential A_x^*. The scalar light shift from the Raman beams, combined with the dipole trap, gave an approximately symmetric three-dimensional potential, with frequencies $f_x, f_y, f_z \approx 70$ Hz. Here, $\hbar k_L = h/(\sqrt{2}\lambda)$ and $E_L = \hbar^2 k_L^2/2m$ are the appropriate units for the momentum and energy.

The spin and momentum states $|m_F, k_x\rangle$ coupled by the Raman beams can be grouped into families of states labelled by the momentum $\hbar k_x$. Each family $\Psi(k_x) = \{|-1, k_x + 2k_L\rangle, |0, k_x\rangle, |+1, k_x - 2k_L\rangle\}$ is composed of states that differ in linear momentum along $\hat{x}$ by $\pm 2\hbar k_L$, and are Raman-coupled with strength $\hbar\Omega_R$. For each k_x, the three dressed states are the eigenstates in the presence of the Raman coupling, with energies[24] $E_j(k_x)$. The resulting vector potential is tunable within the range $-2k_L < q^*A_x^*/\hbar < 2k_L$. In addition, $E_j(k_x)$ includes a scalar potential[16] V'. A_x^*, V', and m^* are functions of Raman coupling Ω_R and detuning δ, and for our typical parameters $m^* \approx 2.5m$, reducing f_x from about 70 Hz to about 40 Hz. The BEC's chemical potential $\mu/h \approx 1$ kHz is much smaller than the $\sim h \times 10$ kHz energy separation between dressed states, so the BEC only occupies the lowest-energy dressed state. Further, it justifies the harmonic expansion around $q^*A_x^*/\hbar$, valid at low energy. Hence, the complete single-atom Hamiltonian is $\mathcal{H} = \mathcal{H}_x^* + \hbar^2\left(k_y^2 + k_z^2\right)/2m + V(\mathbf{r})$, where $V(\mathbf{r})$ is the external potential including $V'(\Omega_R, \delta)$.

The dressed BEC starts in a uniform bias field $B = B_0\hat{y}$, at Raman resonance ($\delta = 0$), corresponding to $A_x^* = 0$[24]. To create a synthetic field B^*, we applied a field gradient b' such that $B = (B_0 - b'y)\hat{y}$, ramping in 0.3 s from $b' = 0$ to a variable value up to 0.055 Tm^{-1}, and then held it constant for t_h to allow the system to equilibrate. The detuning gradient $\delta' = g\mu_B b'/h$ generates a spatial gradient in A_x^*. For the detuning range in our experiment, $\partial A_x^*/\partial\delta$ is approximately constant, leading to an approximately uniform synthetic field B^* given by $B^* = \partial A_x^*/\partial y = \delta'\partial A_x^*/\partial\delta$ (see Fig. 1d). To probe the dressed state, we switched off the dipole trap and the Raman beams in less than 1 μs, projecting each atom into spin and momentum components. We absorption-imaged the atoms after a time-of-flight (TOF) ranging from 10.1 ms to 30.1 ms (Fig. 1e, f).

For a dilute BEC in low synthetic fields, we expect to observe vortices. In this regime, the BEC is described by a macroscopic wavefunction $\psi(\mathbf{r}) = |\psi(\mathbf{r})|e^{i\phi(\mathbf{r})}$, which obeys the Gross–Pitaevskii equation (GPE). The phase ϕ winds by 2π around each vortex, with amplitude $|\psi| = 0$ at the vortex centre. The magnetic flux Φ_{B^*} results in N_v vortices and for an infinite, zero-temperature system, the vortices are arrayed in a lattice[25] with density q^*B^*/h. For finite systems vortices are energetically less favourable, and their areal density is below this asymptotic value, decreasing to zero at a critical field B_c^*. For a cylindrically symmetric BEC, B_c^* is given by $q^*B_c^*/h = 5/(2\pi R^2)\ln(0.67R/\xi)$ where R is the Thomas–Fermi radius and ξ is the healing length[26]. B_c^* is larger for smaller systems. For our non-cylindrically symmetric system, we numerically solve the GPE to determine B_c^* for our experimental parameters (see Methods).

For synthetic fields greater than the critical value, we observed vortices that enter the condensate and reach an equilibrium vortex number N_v after about 0.5 s. Owing to a shear force along $\hat{x}$ when the Raman beams are turned off, the nearly symmetric *in situ* atom cloud tilts during TOF. Although the vortices' positions may rearrange, any initial order is not lost. During the time of our experiment, the

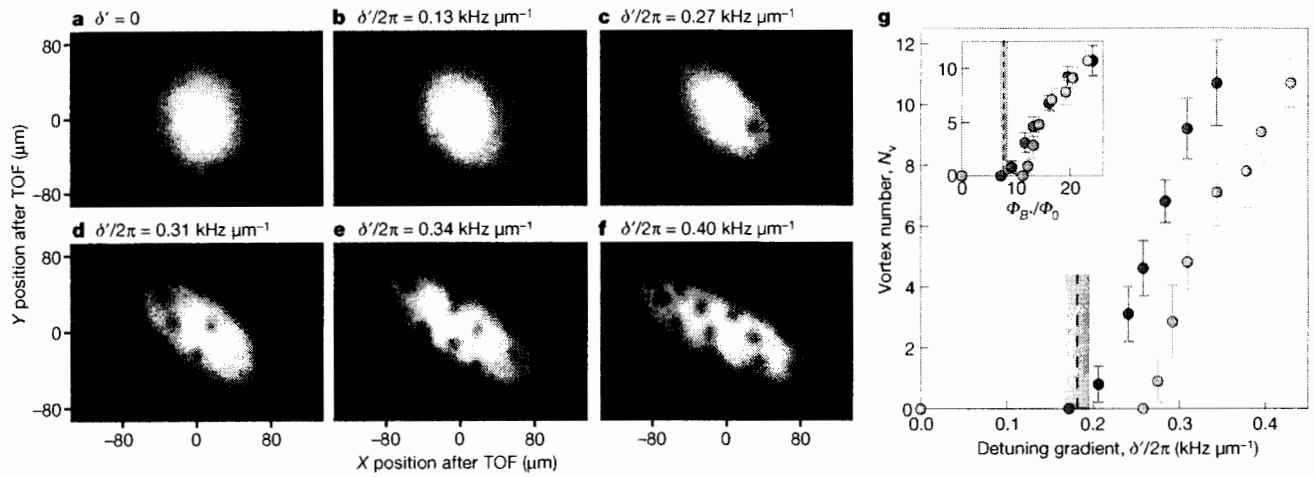

Figure 2 | Appearance of vortices at different detuning gradients. Data was taken for $N = 1.4 \times 10^5$ atoms at hold time $t_h = 0.57$ s. **a–f**, Images of the $|m_F = 0\rangle$ component of the dressed state after a 25.1-ms TOF with detuning gradient $\delta'/2\pi$ from 0 to 0.43 kHz μm^{-1} at Raman coupling $\hbar\Omega_R = 8.20E_L$. **g**, Vortex number N_v versus δ' at $\hbar\Omega_R = 5.85E_L$ (blue circles) and $8.20E_L$ (red circles). Each data point is averaged over at least 20 experimental realizations, and the uncertainties represent one standard deviation σ. The inset displays N_v versus the synthetic magnetic flux $\Phi_{B^*}/\Phi_0 = \mathcal{A}q^*\langle B^*\rangle/h$ in the BEC. The dashed lines indicate δ', below which vortices become energetically unfavourable according to our GPE computation, and the shaded regions show the 1σ uncertainty from experimental parameters.

vortices did not form a lattice and the positions of the vortices were irreproducible between different experimental realizations, consistent with our GPE simulations. We measured N_v as a function of detuning gradient δ' at two couplings, $\hbar\Omega_R = 5.85E_L$ and $8.20E_L$ (Fig. 2). For each Ω_R, vortices appeared above a minimum gradient when the corresponding field $\langle B^*\rangle = \delta'\langle \partial A_x^*/\partial\delta\rangle$ exceeded the critical field B_c^*. (For our coupling, B^* is only approximately uniform over the system and $\langle B^*\rangle$ is the field averaged over the area of the BEC.) The inset shows N_v for both values of Ω_R plotted versus $\Phi_{B^*}/\Phi_0 = \mathcal{A}q^*\langle B^*\rangle/h$, the vortex number for a system of area $\mathcal{A} = \pi R_x R_y$ with the asymptotic vortex density, where R_x (or R_y) is the Thomas–Fermi radius along $\hat{x}$ (or $\hat{y}$). The system size, and thus B_c^*, are approximately independent of Ω_R, so we expected this plot to be nearly independent of Raman coupling. Indeed, the data for $\hbar\Omega_R = 5.85E_L$ and $8.20E_L$ only deviated for $N_v < 5$, probably owing to the intricate dynamics of vortex nucleation[27].

Figure 3 illustrates a progression of images showing that vortices nucleate at the system's edge, fully enter to an equilibrium density and then decay along with the atom number. The timescale for vortex nucleation depends weakly on B^*, and is more rapid for larger B^* with more vortices. It is about 0.3 s for vortex number $N_v \geq 8$, and increases to about 0.5 s for $N_v = 3$. For $N_v = 1$ (B^* near B_c^*), the single vortex always remains near the edge of the BEC. In the dressed state, spontaneous emission from the Raman beams removes atoms from the trap, causing the population to decay with a 1.4(2)-s lifetime, and the equilibrium vortex number decreases along with the area of the BEC.

To verify that the dressed BEC has reached equilibrium, we prepared nominally identical systems in two different ways. First, we varied the initial atom number and measured N_v as a function of atom number N at a fixed hold time of $t_h = 0.57$ s. Second, starting with a large atom number, we measured both N_v and N, as they

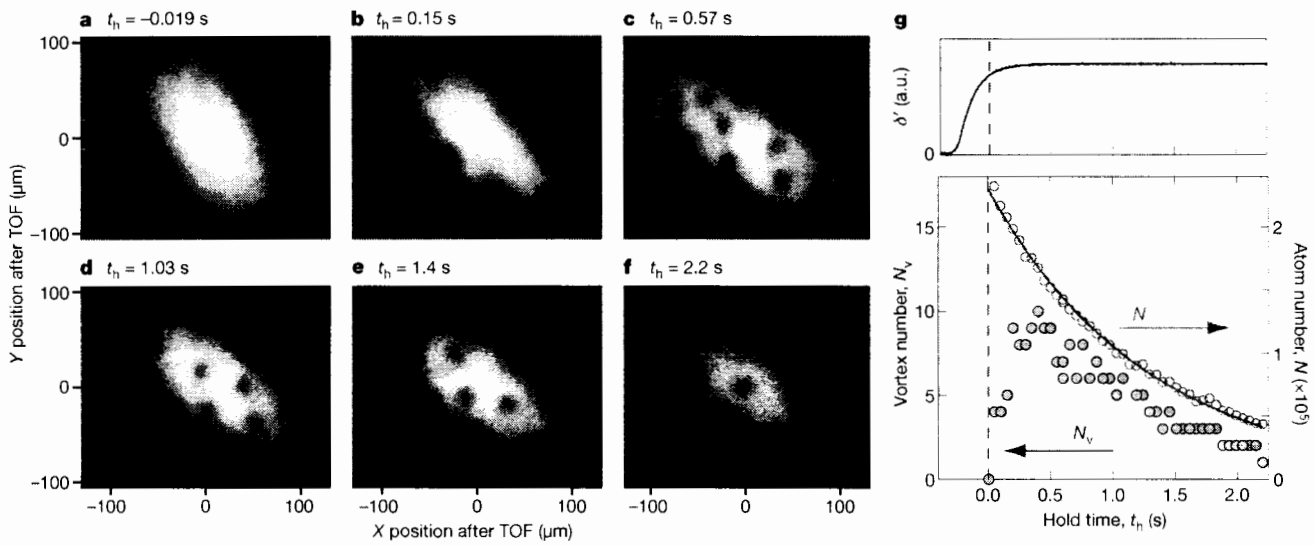

Figure 3 | Vortex formation. **a–f**, Images of the $|m_F = 0\rangle$ component of the dressed state after a 30.1-ms TOF for hold times t_h between −0.019 s and 2.2 s. The detuning gradient $\delta'/2\pi$ is ramped to 0.31 kHz μm^{-1} at the coupling $\hbar\Omega_R = 5.85E_L$. **g**, Top panel shows time sequence of δ'. (a.u., arbitrary units.) Bottom panel shows vortex number N_v (solid symbols) and atom number N (open symbols) versus t_h with a population lifetime of 1.4(2) s. The number in parentheses is the uncorrelated combination of statistical and systematic 1σ uncertainties.

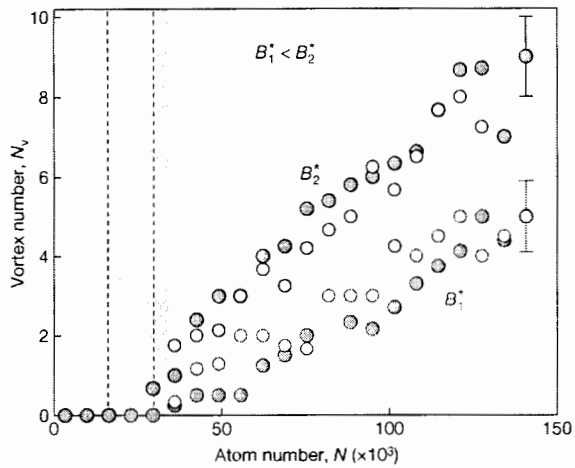

Figure 4 | Equilibrium vortex number. Vortex number N_v versus atom number N at detuning gradient $\delta_1'/2\pi = 0.26$ kHz μm^{-1} (red circles) and $\delta_2'/2\pi = 0.31$ kHz μm^{-1} (black circles), corresponding to synthetic fields $B_1^* < B_2^*$, at Raman coupling $\hbar\Omega_R = 5.85E_L$. The two data points with the largest N show representative 1σ uncertainties, estimated from data in Fig. 2g. We vary N by its initial value with a fixed hold time $t_h = 0.57$ s (solid symbols), and by t_h with a fixed initial N (open symbols). The vertical dashed lines indicate N, below which vortices become energetically unfavourable computed using our GPE simulation. The shaded regions reflect the 1σ uncertainties from the experimental parameters.

decrease with t_h (Fig. 3). Figure 4 compares N_v versus N measured with both methods, each at two detuning gradients corresponding to fields $B_1^* < B_2^*$. The data show that N_v as a function of N is the same for these preparation methods, providing evidence that for $t_h \geq 0.57$ s, N_v has reached equilibrium. As the atom number N falls, the last vortex departs the system when the critical field—increasing with decreasing N—surpasses the actual field.

In conclusion, we have demonstrated optically synthesized magnetic fields for neutral atoms resulting from the Berry's phase, a fundamental concept in physics. This novel approach differs from experiments with rotating gases, in which it is difficult to add optical lattices and rotation is limited by heating, metastability, and the difficulty of adding large angular momentum, preventing access to the quantum-Hall regime. A standout feature in our approach is the ease of adding optical lattices. For example, the addition of a two-dimensional (2D) lattice makes it immediately feasible to study the fractal energy levels of the Hofstadter butterfly[28]. Further, a one-dimensional lattice can divide the BEC into an array of 2D systems normal to the field. A suitable lattice configuration allows access to the $\nu \approx 1$ quantum-Hall regime, with an ensemble of 2D systems each with approximately 200 atoms, and with a realistic interaction energy of about $k_B \times 20$ nK.

METHODS SUMMARY

Dressed state preparation. We created a ^{87}Rb BEC in a crossed dipole trap[29], with $N \approx 4.7 \times 10^5$ atoms in $|F = 1, m_F = -1\rangle$. The quadratic Zeeman shift was $\hbar\varepsilon = 0.61E_L$ for $\omega_Z/2\pi = g\mu_B B/h \approx 2.71$ MHz, where g is the Landé g-factor. To maintain $\delta = 0$ at the BEC's centre as we ramped the field gradient b', we changed $g\mu_B B_0$ by as much as $7E_L$. Simultaneously, we decreased the dipole beam power by 20%, producing our approximately 40-Hz trap frequency along $\hat{x}$. Additionally, the detuning gradient $\delta' y$ made the scalar potential V' anti-trapping along $\hat{y}$, reducing f_y from 70 Hz to 50 Hz for our largest δ'. Spontaneous emission from the Raman beams decreased the atom number to $N \approx 2.5 \times 10^5$ for $t_h = 0$, with a condensate fraction of 0.85.

Numerical method. We compared our data to a finite temperature 2D stochastic GPE[30] simulation including the dressed state dispersion $E(k_x, y)$ that depends on y through the detuning gradient δ'. We evolved the time-dependent projected GPE:

$$i\hbar\frac{\partial\psi(\mathbf{x},t)}{\partial t} = \mathcal{P}\left\{\left[E\left(-i\hbar\frac{\partial}{\partial x}, y\right) - \frac{\hbar^2}{2m}\frac{\partial^2}{\partial y^2} + g_{2D}|\psi(\mathbf{x},t)|^2\right]\psi(\mathbf{x},t)\right\}$$

$\mathcal{P}$ projects onto a set of significantly occupied modes, and g_{2D} parameterizes the 2D interaction strength. The stochastic GPE models interactions between the highly occupied modes described by ψ and sparsely occupied thermal modes with dissipation and an associated noise term. We approximately accounted for the finite extent along $\hat{z}$ by making g_{2D} depend on the local 2D density. For low temperatures this 2D model correctly recovers the three-dimensional Thomas–Fermi radii, and gives the expected 2D density profile. These quantitative details are required to compute correctly the critical field or number for the first vortex to enter the system, which are directly tied to the 2D condensate area.

Received 7 August; accepted 20 October 2009.

1. Greiner, M., Mandel, O., Esslinger, T., Hänsch, T. W. & Bloch, I. Quantum phase transition from a superfluid to a Mott insulator in a gas of ultracold atoms. *Nature* 415, 39–44 (2003).
2. Regal, C. A., Greiner, M. & Jin, D. S. Observation of resonance condensation of fermionic atom pairs. *Phys. Rev. Lett.* 92, 040403 (2004).
3. Zwierlein, M. W. *et al.* Condensation of pairs of fermionic atoms near a Feshbach resonance. *Phys. Rev. Lett.* 92, 120403 (2004).
4. Tsui, D. C., Stormer, H. L. & Gossard, A. C. Two-dimensional magnetotransport in the extreme quantum limit. *Phys. Rev. Lett.* 48, 1559–1562 (1982).
5. Laughlin, R. B. Anomalous quantum Hall effect: an incompressible quantum fluid with fractionally charged excitations. *Phys. Rev. Lett.* 50, 1395–1398 (1983).
6. Zwierlein, M. W., Abo-Shaeer, J. R., Schirotzek, A., Schunck, C. H. & Ketterle, W. Vortices and superfluidity in a strongly interacting Fermi gas. *Nature* 435, 1047–1051 (2005).
7. Schweikhard, V., Coddington, I., Engels, P., Mogendorff, V. P. & Cornell, E. A. Rapidly rotating Bose-Einstein condensates in and near the lowest Landau level. *Phys. Rev. Lett.* 92, 040404 (2004).
8. Madison, K. W., Chevy, F., Wohlleben, W. & Dalibard, J. Vortex formation in a stirred Bose-Einstein condensate. *Phys. Rev. Lett.* 84, 806–809 (2000).
9. Abo-Shaeer, J. R., Raman, C., Vogels, J. M. & Ketterle, W. Observation of vortex lattices in Bose-Einstein condensates. *Science* 292, 476–479 (2001).
10. Juzeliūnas, G. & Öhberg, P. Slow light in degenerate Fermi gases. *Phys. Rev. Lett.* 93, 033602 (2004).
11. Jaksch, D. & Zoller, P. Creation of effective magnetic fields in optical lattices: the Hofstadter butterfly for cold neutral atoms. *N. J. Phys.* 5, 56.1–56.11 (2003).
12. Sorensen, A. S., Demler, E. & Lukin, M. D. Fractional quantum Hall states of atoms in optical lattices. *Phys. Rev. Lett.* 94, 086803 (2005).
13. Berry, M. V. Quantal phase factors accompanying adiabatic changes. *Proc. R. Soc. Lond. A* 392, 45–57 (1984).
14. Juzeliūnas, G., Ruseckas, J., Öhberg, P. & Fleischhauer, M. Light-induced effective magnetic fields for ultracold atoms in planar geometries. *Phys. Rev. A* 73, 025602 (2006).
15. Gunter, K. J., Cheneau, M., Yefsah, T., Rath, S. P. & Dalibard, J. Practical scheme for a light-induced gauge field in an atomic Bose gas. *Phys. Rev. A* 79, 011604 (2009).
16. Spielman, I. B. Raman processes and effective gauge potentials. *Phys. Rev. A* 79, 063613 (2009).
17. Nayak, C., Simon, S. H., Stern, A., Freedman, M. & Sarma, S. D. Non-abelian anyons and topological quantum computation. *Rev. Mod. Phys.* 80, 1083–1159 (2008).
18. Radu, I. P. *et al.* Quasi-particle properties from tunneling in the formula fractional quantum Hall state. *Science* 320, 899–902 (2008).
19. Cooper, N. R. Rapidly rotating atomic gases. *Adv. Phys.* 57, 539–616 (2008).
20. Cheneau, M. *et al.* Geometric potentials in quantum optics: A semi-classical interpretation. *Europhys Lett.* 83, 60001 (2008).
21. Leanhardt, A. E. *et al.* Imprinting vortices in a Bose-Einstein condensate using topological phases. *Phys. Rev. Lett.* 89, 190403 (2002).
22. Andersen, M. F. *et al.* Quantized rotation of atoms from photons with orbital angular momentum. *Phys. Rev. Lett.* 97, 170406 (2006).
23. Matthews, M. R. *et al.* Vortices in a Bose-Einstein condensate. *Phys. Rev. Lett.* 83, 2498–2501 (1999).
24. Lin, Y.-J. *et al.* Bose-Einstein condensate in a uniform light-induced vector potential. *Phys. Rev. Lett.* 102, 130401 (2009).
25. Yarmchuk, E. J., Gordon, M. J. V. & Packard, R. E. Observation of stationary vortex arrays in rotating superfluid helium. *Phys. Rev. Lett.* 43, 214–217 (1979).
26. Lundh, E., Pethick, C. J. & Smith, H. Zero-temperature properties of a trapped Bose-condensed gas: beyond the Thomas-Fermi approximation. *Phys. Rev. A* 55, 2126–2131 (1997).
27. Murray, D. R., Öhberg, P., Gomila, D. & Barnett, S. M. Vortex nucleation in Bose-Einstein condensates due to effective magnetic fields. *Phys. Rev. A* 79, 063618 (2009).
28. Hofstadter, D. R. Energy levels and wave functions of Bloch electrons in rational and irrational magnetic fields. *Phys. Rev. B* 14, 2239–2249 (1976).
29. Lin, Y.-J., Perry, A. R., Compton, R. L., Spielman, I. B. & Porto, J. V. Rapid production of ^{87}Rb Bose-Einstein condensates in a combined magnetic and optical potential. *Phys. Rev. A* 79, 063631 (2009).
30. Blakie, P. B., Bradley, A. S., Davis, M. J., Ballagh, R. J. & Gardiner, C. W. Dynamics and statistical mechanics of ultra-cold Bose gases using c-field techniques. *Adv. Phys.* 57, 363–455 (2008).

With the advent of quantum technologies, scientists are now trying to build quantum networks that are expected to be much more powerful than the simple sum of their constituents[1]. Pioneering experiments in this line of research include the photonic coupling of identical quantum nodes, such as atomic ensembles[3,4,9], single trapped atoms[10,11] and ions[12], and solid-state devices[13–15]. Each platform comes with individual functionalities, for example in terms of processing and storage. Hence, a hybrid quantum network, which benefits from the strengths of different platforms, would offer more capabilities than a network consisting of identical quantum systems. Although great efforts have been devoted to building hybrid quantum systems, for example devices combining different quantum systems on a single chip[16] or different species of closely spaced trapped ions[17,18], interactions between these systems are typically mediated by microwave photons or Coulomb interactions, which are not favourable for long-distance quantum communication.

Photonic interconnections between different quantum systems have so far been realized in very few experiments[19–22], but these have neither demonstrated quantum state transfer nor interfaced two different long-lived quantum memory systems, which are both crucial requirements for quantum network applications. A photonic quantum interconnection between different platforms has been demonstrated previously[23], but only using a single atomic species. The main challenge in efficiently interfacing two different quantum systems via a photonic link is to obtain strong light–matter interaction between a single mediating photon and the two matter systems, whose atomic transitions can differ considerably in wavelength and linewidth.

Here, we demonstrate quantum state transfer between two fundamentally different quantum memory systems by means of a single photon at telecommunication wavelength. On the one hand, we use a laser-cooled ensemble of ^{87}Rb atoms, which, besides being an excellent quantum memory and single-photon source[24], also gives access to tunable nonlinear interactions enabling quantum processing through Rydberg excitations[25]. On the other hand, we use a rare-earth-ion-doped crystal (Pr^{3+}:Y_2SiO_5) that exhibits outstanding properties for multiplexed long-lived quantum state storage[6,26–28]. To overcome the

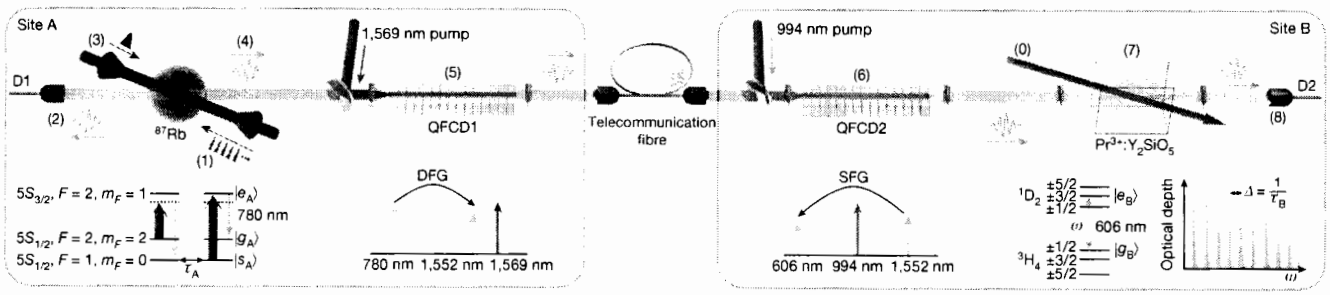

Figure 1 | Schematic set-up and relevant level schemes. At site A, a cold cloud of ^{87}Rb atoms is held inside a MOT. Following the DLCZ protocol, non-classically correlated photon pairs are produced by first sending classical write pulses (1), generating a spin-wave inside the atomic cloud heralded by a write photon (2), which is spectrally filtered by a monolithic Fabry–Perot cavity (not shown). Upon a write-photon detection at D1, the spin-wave is read out by sending a classical read pulse (3), generating the read photon (4). QFCD1 consists of a periodically poled lithium niobate (PPLN) crystal with an integrated proton exchange waveguide that is continuously pumped by a strong pump laser at 1,569 nm. It converts the read photon from 780 nm to 1,552 nm (5). The converted photon is then separated from the strong pump light by dielectric bandpass filters (not shown) before it is sent through a telecommunication fibre to site B where QFCD2 (consisting of a PPLN ridge waveguide pumped by strong 994 nm laser radiation) converts it to 606 nm by means of SFG (6), before the photon is again spectrally filtered by several elements (not shown; see Methods). The Pr^{3+}:Y_2SiO_5 crystal was initially prepared with an AFC (0) using a strong preparation beam at 606 nm, to store the converted read photon (7). The inset shows the optical depth of a typical AFC structure. After retrieval, the photon is finally detected at D2 (8).

wavelength gap between the two systems, we use quantum frequency-conversion techniques to convert photons emitted by the ^{87}Rb quantum memory from 780 nm to the telecommunication C-band at 1,552 nm and then back to 606 nm to resonantly interact with the Pr^{3+}:Y_2SiO_5 crystal. We show that a single collective spin excitation (spin-wave) stored in the cold atomic quantum memory can be optically transferred to a long-lived collective optical excitation inside the crystal. By transmitting correlated single photons and qubits, we demonstrate quantum correlation preserving and coherent quantum state transfer between the disparate quantum nodes.

The basic concept of our experiment can be understood in terms of the scheme depicted in Fig. 1, which is separated into two main sites A and B (for a detailed description and figure see Methods and Extended Data Fig. 1). At site A, we operate a ^{87}Rb magneto-optical trap (MOT) to generate synchronizable single photons of controllable bandwidth and temporal shape (see Methods) which are later frequency-converted from 780 nm to 1,552 nm in an all-solid-state quantum frequency-conversion device (QFCD). Following the Duan–Lukin–Cirac–Zoller (DLCZ) protocol[29], we send a series of classical write pulses onto the Rb atoms to create Raman-scattered write photons with intrinsic excitation probability p_e per optical mode and trial. A single optical mode of the isotropically emitted write photons is collected and sent to single-photon detector (SPD) D1. A detection event at D1 heralds the generation of a spin-wave involving long-lived ground states of the ^{87}Rb ensemble. After a programmable storage time, we apply a classical read pulse, to deterministically read out the spin-wave and generate a read photon in a well-defined spatio-temporal mode, with a fibre-coupled retrieval efficiency of $\eta_{\mathrm{ret}}^{\mathrm{A}} \approx 30\%$. Depending on the temporal shape of the read pulse, we generate single read photons with Gaussian envelope or time-bin envelope exhibiting a sub-natural linewidth of about 2 MHz (see Methods). The read single photon is then sent to the first QFCD, which converts it from 780 nm to 1,552 nm via difference frequency generation (DFG)[30] with an internal conversion efficiency of $\eta_{\mathrm{int}}^{\mathrm{QFCD1}} = 56\%$. After noise filtering, the converted photon is then coupled into a 10 m telecommunication fibre and sent to site B in another laboratory.

At site B, the telecommunication read photon is first up-converted to 606 nm ($\eta_{\mathrm{int}}^{\mathrm{QFCD2}} = 60\%$) via sum frequency generation (SFG) in QFCD2. After noise filtering, the single photon is sent to the Pr^{3+}:Y_2SiO_5 crystal inside a cryostat at a temperature of 3.5 K. We use the atomic frequency comb (AFC) scheme[5] to store, analyse and retrieve the converted single photon. We create an AFC of 4-MHz width with absorption peaks spaced by $\Delta = 400$ kHz on the optical transition of Pr^{3+} at 606 nm. Then, the converted single photon is stored by the AFC and collectively re-emitted with an efficiency of $\eta^{\mathrm{B}} = 30\%$ after a pre-defined storage time of $\tau_{\mathrm{B}} = 1/\Delta = 2.5\,\mu$s before being detected by SPD D2. The probability of obtaining an emitted, converted, stored and retrieved photon after the crystal, conditioned on a write photon detection at D1, is approximately 10^{-3}. This includes 1.2% total conversion efficiency (with all optical losses) from 780 nm to 606 nm.

An important experimental requirement to successfully achieve quantum state transfer is to precisely match the central frequencies of the converted read photon and the prepared AFC. Also, the linewidths of all the lasers involved must be minimized to ensure efficient storage and stable interference conditions for the qubit analysis. We estimate that the frequency stability of the converted photon needs to be better than 1 MHz (see Methods). This is done by active frequency stabilization and a chopped beat-note lock between classical 780 nm light converted in the QFCDs and the 606 nm preparation laser as reference (see Methods).

Before interfacing the two quantum systems, we characterized the read photons generated at site A. Figure 2a shows the heralded auto-correlation function $\alpha = g^{(2)}_{r_A, r_A|w}$ (see Methods) for different p_e measured via a Hanbury Brown–Twiss set-up inserted directly after the MOT. We obtain strongly anti-bunched read photons in the single-photon regime ($\alpha < 0.5$) for low p_e (less than about 11%) and in the non-classical regime ($\alpha < 1$) for p_e less than about 25%, before surpassing

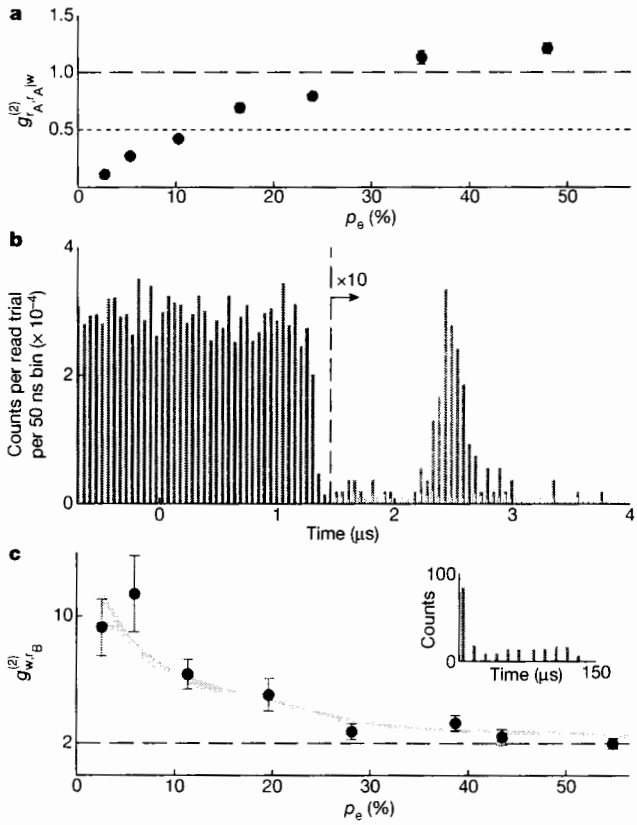

Figure 2 | Photon generation, conversion and storage. a, Anti-bunching parameter α of the read photon after the MOT, plotted against excitation probability p_e. The dashed line indicates the threshold for classical states ($\alpha \geq 1$) and the dotted line the threshold for a two-photon Fock state ($\alpha = 0.5$). **b**, Time histogram of detections at D2 if the spin-wave ($p_e \approx 35\%$) is read out from the cold atomic Rb quantum memory, the photons are frequency-converted in the QFCDs, and stored at $t = 0$ in the crystal. During storage (at $t = 1.2\,\mu$s), the pump of QFCD2 is gated off, and the re-emitted photons are detected as a pronounced AFC echo at $t = 2.5\,\mu$s (red trace, detected coincidence rate approximately 90 per hour in a 400 ns window around the echo). The green trace corresponds to the noise level, that is, if no read photon is sent. To improve clarity, the counts on the right-hand side have been multiplied by 10. **c**, Normalized cross-correlation $g^{(2)}_{w,r_B}$ between the write photons from the cold atomic quantum memory and the converted, stored and retrieved read photons from the crystal for different p_e. The green area corresponds to the expected $g^{(2)}_{w,r_B}$ as deduced from a model similar to that used in previous work[30]. The dashed line represents the classical upper bound $g^{(2)}_{w,r_B} = 2$. The inset shows a typical $g^{(2)}$ histogram of coincidence detections for several read-out trials separated by the trial period of about 13 μs obtained at $p_e \approx 11\%$. Error bars correspond to ±1 s.d. of the photon counting statistics.

the classical threshold for higher p_e owing to multiple spin-wave excitations.

We now present photon generation, conversion and storage involving the whole experimental set-up. We first verify that photons emitted by the atomic quantum memory can be successfully converted and stored in the crystal. At site A, we create heralded 220-ns-long (full-width at half-maximum, FWHM) Gaussian read photons at $p_e \approx 35\%$. Figure 2b shows the histogram of detection events at D2. The photons arrive at the crystal at $t = 0\,\mu$s, but no leakage is visible here, as the photons are buried in the noise generated by the QFCDs. The noise is suppressed at $t = 1.2\,\mu$s by gating off the pump of QFCD2. At $t = 2.5\,\mu$s we detect a pronounced echo signature from the retrieved read photons with a signal-to-noise ratio of 17 ± 2, mostly limited by the dark counts of D2. The echo shows a similar Gaussian temporal

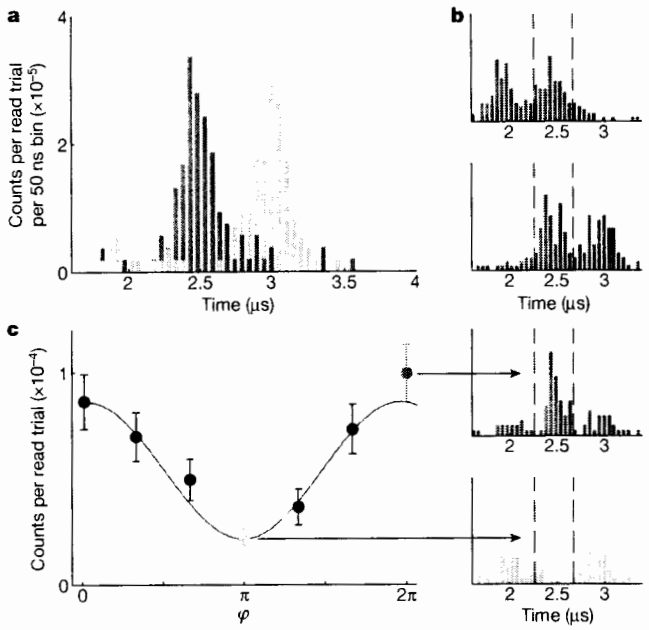

Figure 3 | Coherence preservation. a, Detected echo of Gaussian-shaped read photons which were created ($p_e \approx 35\%$) at either an early time $t = 0$ (red) or at a later time $t = 0.5\,\mu s$ (blue) at site A and stored for $\tau_B = 2.5\,\mu s$ at site B. **b**, Time-bin photons stored and retrieved after either a short storage time, $\tau_{B_1} = 2\,\mu s$ (top), or a long one, $\tau_{B_2} = 2.5\,\mu s$ (bottom). **c**, Time-bin interference fringe: coincidence counts between initial write-photon detections at D1 and detection events during the time-bin overlap at D2 if a time-bin read photon is stored and retrieved from the crystal prepared with two AFCs. Error bars correspond to ±1 s.d. of the photon-counting statistics. On the right, two examples of time histograms between detection events at D1 and D2 are shown for $\varphi = 0°$ (top) and $\varphi = 180°$ (bottom). The 400 ns coincidence window where the time bins overlap is indicated by dashed lines.

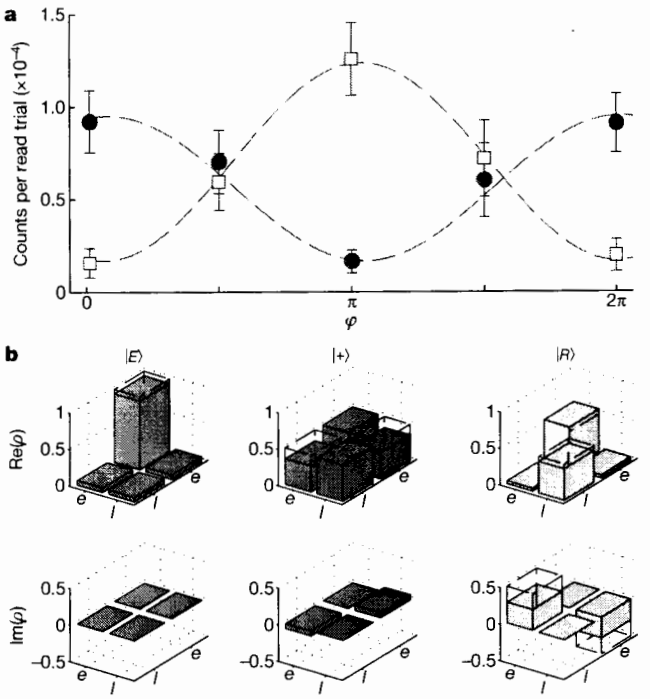

Figure 4 | Single-photon qubit transfer. a, Interference fringes from a single time-bin read photon $|\Psi_{eq}\rangle = \frac{1}{\sqrt{2}}(|e\rangle + e^{i\varphi}|l\rangle)$ generated at site A ($p_e \approx 5\%$ corresponding to $\alpha = 0.26$) if the second AFC is prepared with zero detuning (red dots, $V = 70\% \pm 6\%$) or shifted by 200 kHz (blue open squares, $V = 76\% \pm 3\%$). Error bars correspond to ±1 s.d. of the photon-counting statistics. **b**, Real and imaginary parts of the reconstructed density matrices measured after the crystal at site B if the qubits $|E\rangle, |+\rangle, |R\rangle$ are generated at site A, converted in the QFCDs and stored at B. Open boxes indicate the target state.

shape to the initial read photons, with a slightly larger FWHM of approximately 260 ns.

To investigate the non-classicality of the state transfer, we measured the normalized cross-correlation function $g^{(2)}_{w,r_B}$ (see Methods) of the converted, stored and retrieved photons with the initial write photons for different p_e by comparing coincidences in different storage trials (see Fig. 2c). At $p_e \approx 5\%$ (with a coincidence rate of approximately 20 counts per hour) we obtain $g^{(2)}_{w,r_B} = 11.4 \pm 2.4$, demonstrating quantum-correlation-preserving state transfer, as the $g^{(2)}_{w,r_B}$ value stays well above the classical bound of $g^{(2)} = 2$ assuming thermal statistics for the write and read photons (see Methods). The same holds true for a broad range of p_e and for storage times τ_B up to 10 μs (see Methods). The experimental data in Fig. 2c match well with the expected behaviour (green area) calculated through a simple model that takes into account the measured cross-correlation $g^{(2)}_{w,r_A}$ after the MOT and the total signal-to-noise ratio of the read photon after conversion and storage[30].

Next, we studied the coherence properties of the state transfer between the two different quantum systems. We use time-bin qubits, which offer advantages for long-distance quantum communication due to their robustness against external perturbations. If a heralding write photon is detected at D1, we shape the read pulse in a way that the spin-wave stored in the Rb quantum memory is mapped onto a photonic time-bin qubit $|\Psi_A\rangle = c_1|e\rangle + c_2 e^{i\varphi}|l\rangle$, where $|e\rangle$ and $|l\rangle$ represent early and late time bins, φ is their relative phase, controlled by the phase of the second read-out peak, and $c_1^2 + c_2^2 = 1$ (see Methods). To store the photonic time-bin qubit, we take advantage of the intrinsic temporal multimodality of the AFC scheme[5].

Figure 3a shows the time histogram of detection events at D2 of the early and late time bins (created at $p_e \approx 35\%$) sent through the QFCDs, and stored and retrieved from the crystal prepared with a single AFC of $\tau_B = 2.5\,\mu s$ storage time. The two echoes represent the polar states of a time-bin qubit and exhibit an average signal-to-noise ratio of 19 ± 2. If a delocalized time-bin photon ($c_1 = c_2 = 1/\sqrt{2}$) is created in the Rb quantum memory, converted in the QFCDs and stored in the crystal for either $\tau_{B_1} = 2\,\mu s$ or $\tau_{B_2} = 2.5\,\mu s$, we detect the histograms shown in Fig. 3b. To analyse the qubit, we use the crystal as an interferometer by preparing two overlapping AFCs with storage times τ_{B_1} and τ_{B_2} ($\eta^B = 10\%$ each)[5]. In that case, we obtain the histograms shown in the right panels of Fig. 3c. These two histograms were recorded with a phase shift of $\varphi = 0°$ (top) and $\varphi = 180°$ (bottom) between the early and late time bins. Strong interference between the two temporal modes can be seen in the central region where the time bins overlap. Measuring the coincidences in that time window versus φ gives the interference fringe depicted in Fig. 3c with a fitted visibility of $V = 60\% \pm 9.9\%$, confirming the high degree of coherence preservation between the two disparate quantum systems.

Finally, to demonstrate qubit transfer between the cold atomic cloud and the crystal via telecommunication photons, we decreased p_e to 5%, generating true single time-bin read photons at site A with an anti-bunching parameter of $\alpha = 0.26 \pm 0.02$ (see Fig. 2a). Following the same approach as above, we show in Fig. 4a that with converted and stored single time-bin photons, we obtain interference between overlapping bins with visibilities around 70%. Moreover, we show that, by changing the central frequency of the second AFC by 200 kHz, the phase of the interference fringe can be shifted by 180°, verifying the intrinsic phase-analysing capabilities of the AFC (see Methods). This capability permits the measurement of time-bin qubits in different

bases and hence a full analysis of the stored qubits by quantum state tomography. Figure 4b shows the reconstructed density matrices ρ of the retrieved states after the crystal at site B when three orthogonal time-bin qubits $|E\rangle = |e\rangle$, $|+\rangle = \frac{1}{\sqrt{2}}(|e\rangle + |l\rangle)$ and $|R\rangle = \frac{1}{\sqrt{2}}(|e\rangle + i|l\rangle)$ are generated in the cold atomic quantum memory at site A, afterwards converted in the QFCDs, and stored at site B. The state reconstruction is based on maximum likelihood estimation. The qubit fidelity conditioned on a successful detection of the photon after retrieval from the crystal (conditional fidelity) is calculated as $\mathcal{F}^{c}_{|\Psi\rangle} = \langle\Psi|\rho|\Psi\rangle$ with $|\Psi\rangle$ denoting the target state. From Fig. 4b, it is evident that we obtain a high overlap between the reconstructed qubits and the target states with conditional fidelities of $\mathcal{F}^{c}_{|+\rangle} = 85.4\% \pm 6.6\%$, $\mathcal{F}^{c}_{|R\rangle} = 78.2\% \pm 6.9\%$ and $\mathcal{F}^{c}_{|E\rangle} = 93.8\% \pm 2.8\%$, where the errors were estimated via Monte Carlo simulations taking into account the uncertainty of the photon-counting statistics. Despite the low total efficiency of the state transfer, we demonstrate an average conditional fidelity of $\mathcal{F}^{c} = 85.8\% \pm 3.3\%$ for the generated and transferred qubit, which is consistent with results inferred at higher p_e and surpasses the classical threshold of 66.7% by more than five standard deviations (5 s.d.). Overall, the conditional fidelities are limited by the signal-to-noise ratio of the retrieved photons, and thus by the efficiencies of all the involved processes. However, for the equatorial states, the main limitation is the finite linewidth of the combined laser system, which we estimate to be around 600 kHz (see Methods). This large sensitivity to frequency fluctuations is due to the large separation between the two time bins (500 ns) imposed by the AFC bandwidth.

For potential applications in hybrid quantum networks, the transfer efficiency (currently 10^{-3}) will need to be greatly increased. The largest part of the inefficiency is due to technical optical loss in the various elements ($\eta_{\text{loss}} = 0.04$). This could be greatly improved by using, for example, fibre-pigtailed waveguide converters. The combined quantum memory efficiency ($\eta_{\text{QM}} = 0.09$) could also be increased with state-of-the-art techniques[6,31]. Increased efficiencies would also enable spin-wave storage in the crystal, leading to on-demand read-out and longer storage times[28]. Although all efficiencies could in principle be pushed towards unity (except fibre transmission), an interesting direction to alleviate optical losses would be to implement a non-destructive detection of the time-bin qubit with the AFC, as recently proposed[32].

Our work represents a demonstration of quantum communication between heterogeneous quantum nodes and opens up prospects for combining quantum nodes with different capabilities. Moreover, it gives a perspective on how the distance between the nodes can be extended by back and forth conversion of photonic qubits into the telecommunication C-band. The technique could also be extended to connect other physical platforms, for example single ions or nitrogen–vacancy centres for which heralded absorption is possible. Our results hold promise for the realization of large-scale hybrid quantum networks.

Online Content Methods, along with any additional Extended Data display items and Source Data, are available in the online version of the paper; references unique to these sections appear only in the online paper.

Received 7 June; accepted 26 September 2017.

1. Kimble, H. J. The quantum internet. *Nature* **453,** 1023–1030 (2008).
2. Wallquist, M., Hammerer, K., Rabl, P., Lukin, M. & Zoller, P. Hybrid quantum devices and quantum engineering. *Phys. Scr.* **T137,** 014001 (2009).
3. Chou, C. W. *et al.* Measurement-induced entanglement for excitation stored in remote atomic ensembles. *Nature* **438,** 828–832 (2005).
4. Chanelière, T. *et al.* Storage and retrieval of single photons transmitted between remote quantum memories. *Nature* **438,** 833–836 (2005).
5. de Riedmatten, H., Afzelius, M., Staudt, M. U., Simon, C. & Gisin, N. A solid-state light-matter interface at the single-photon level. *Nature* **456,** 773–777 (2008).
6. Hedges, M. P., Longdell, J. J., Li, Y. & Sellars, M. J. Efficient quantum memory for light. *Nature* **465,** 1052–1056 (2010).
7. Clausen, C. *et al.* Quantum storage of photonic entanglement in a crystal. *Nature* **469,** 508–511 (2011).
8. Saglamyurek, E. *et al.* Broadband waveguide quantum memory for entangled photons. *Nature* **469,** 512–515 (2011).
9. Eisaman, M. D. *et al.* Electromagnetically induced transparency with tunable single-photon pulses. *Nature* **438,** 837–841 (2005).
10. Ritter, S. *et al.* An elementary quantum network of single atoms in optical cavities. *Nature* **484,** 195–200 (2012).
11. Hofmann, J. *et al.* Heralded entanglement between widely separated atoms. *Science* **337,** 72–75 (2012).
12. Moehring, D. L. *et al.* Entanglement of single-atom quantum bits at a distance. *Nature* **449,** 68–71 (2007).
13. Usmani, I. *et al.* Heralded quantum entanglement between two crystals. *Nat. Photon.* **6,** 234–237 (2012).
14. Pfaff, W. *et al.* Unconditional quantum teleportation between distant solid-state quantum bits. *Science* **345,** 532–535 (2014).
15. Delteil, A., Sun, Z., Fält, S. & Imamoğlu, A. Realization of a cascaded quantum system: heralded absorption of a single photon qubit by a single-electron charged quantum dot. *Phys. Rev. Lett.* **118,** 177401 (2017).
16. Xiang, Z.-L., Ashhab, S., You, J. Q. & Nori, F. Hybrid quantum circuits: superconducting circuits interacting with other quantum systems. *Rev. Mod. Phys.* **85,** 623–653 (2013).
17. Tan, T. R. *et al.* Multi-element logic gates for trapped-ion qubits. *Nature* **528,** 380–383 (2015).
18. Ballance, C. J. *et al.* Hybrid quantum logic and a test of Bell's inequality using two different atomic isotopes. *Nature* **528,** 384–386 (2015).
19. Akopian, N., Wang, L., Rastelli, A., Schmidt, O. G. & Zwiller, V. Hybrid semiconductor-atomic interface: slowing down single photons from a quantum dot. *Nat. Photon.* **5,** 230–233 (2011).
20. Siyushev, P., Stein, G., Wrachtrup, J. & Gerhardt, I. Molecular photons interfaced with alkali atoms. *Nature* **509,** 66–70 (2014).
21. Meyer, H. M. *et al.* Direct photonic coupling of a semiconductor quantum dot and a trapped ion. *Phys. Rev. Lett.* **114,** 123001 (2015).
22. Tang, J.-S. *et al.* Storage of multiple single-photon pulses emitted from a quantum dot in a solid-state quantum memory. *Nat. Commun.* **6,** 8652 (2015).
23. Lettner, M. *et al.* Remote entanglement between a single atom and a Bose–Einstein condensate. *Phys. Rev. Lett.* **106,** 210503 (2011).
24. Sangouard, N., Simon, C., de Riedmatten, H. & Gisin, N. Quantum repeaters based on atomic ensembles and linear optics. *Rev. Mod. Phys.* **83,** 33–80 (2011).
25. Saffman, M., Walker, T. G. & Mølmer, K. Quantum information with Rydberg atoms. *Rev. Mod. Phys.* **82,** 2313–2363 (2010).
26. Ferguson, K. R., Beavan, S. E., Longdell, J. J. & Sellars, M. J. Generation of light with multimode time-delayed entanglement using storage in a solid-state spin-wave quantum memory. *Phys. Rev. Lett.* **117,** 020501 (2016).
27. Kutluer, K., Mazzera, M. & de Riedmatten, H. Solid-state source of nonclassical photon pairs with embedded multimode quantum memory. *Phys. Rev. Lett.* **118,** 210502 (2017).
28. Seri, A. *et al.* Quantum correlations between single telecom photons and a multimode on-demand solid-state quantum memory. *Phys. Rev. X* **7,** 021028 (2017).
29. Duan, L. M., Lukin, M. D., Cirac, J. I. & Zoller, P. Long-distance quantum communication with atomic ensembles and linear optics. *Nature* **414,** 413–418 (2001).
30. Albrecht, B., Farrera, P., Fernandez-Gonzalvo, X., Cristiani, M. & de Riedmatten, H. A waveguide frequency converter connecting rubidium-based quantum memories to the telecom C-band. *Nat. Commun.* **5,** 3376 (2014).
31. Yang, S.-J., Wang, X.-J., Bao, X.-H. & Pan, J.-W. An efficient quantum light–matter interface with sub-second lifetime. *Nat. Photon.* **10,** 381–384 (2016).
32. Sinclair, N. *et al.* Proposal and proof-of-principle demonstration of non-destructive detection of photonic qubits using a Tm:$LiNbO_3$ waveguide. *Nat. Commun.* **7,** 13454 (2016)

METHODS

In the following, we give a detailed description of the experimental procedures and the experimental set-up as shown in Extended Data Fig. 1. We also present additional measurements and discuss limitations. It is convenient to divide the experiment into three sections: the cold atomic gas quantum memory; the solid-state storage device; and the quantum frequency-conversion (QFC) interface. We first discuss these three sections separately, before addressing additional measurements in the final section.

Cold atomic gas quantum memory. *Set-up.* The cold atomic quantum memory at site A consists of a cloud of ^{87}Rb atoms, kept in an ultrahigh-vacuum chamber and cooled by magneto-optical trapping. The cooling and repumping beams (not shown in Extended Data Fig. 1) are derived from the write and read diode lasers which are locked through Doppler-free absorption spectroscopy to Rb reference cells to be resonant with the D_2 line of ^{87}Rb at 780 nm. After passing through acousto-optic modulators (AOMs) in double-pass configuration, the cooling beam is red-detuned by 20 MHz to the $|F=2\rangle \leftrightarrow |F'=3\rangle$ transition, and the repumping beam is resonant to the $|F=1\rangle \leftrightarrow |F'=2\rangle$ transition. They are combined with a magnetic gradient of 20 G cm^{-1} to load $N \approx 10^8$ Rb atoms into the MOT. After a 2-ms-long optical molasses phase, the temperature of the atoms is about $T \approx 100\,\mu K$. Next, all population is prepared in the $|g_A\rangle = |5S_{1/2}, F=2, m_F=2\rangle$ Zeeman sublevel by applying the repumping light and σ^+ polarized optical pumping light on the $|F=2\rangle \leftrightarrow |F'=2\rangle$ transition (not shown in Extended Data Fig. 1).

To generate the spin-wave inside the atomic cloud, we send write pulses (derived from the write laser and a subsequent double-pass AOM) which are 40 MHz red-detuned from the $|g_A\rangle \rightarrow |e_A\rangle = |5P_{3/2}, F=2, m_F=1\rangle$ transition and exhibit a duration of 20 ns (full-width at half-maximum, FWHM). The write pulses pass a polarizing beam splitter (PBS) and a quarter-wave plate to set their polarization to σ^- in the frame of the atoms. The quantization axis is set by a bias magnetic field of $B = 110$ mG along the write/read photon direction. The write pulses generate Raman-scattered write photons, which are emitted on transition $|e_A\rangle \rightarrow |s_A\rangle = |5S_{1/2}, F=1, m_F=0\rangle$. A small fraction of the isotropically emitted write photons is collected at an angle of 3.4° with respect to the write/read pulse axis. The write photons pass a combination of quarter-wave plate, half-wave plate and PBS to couple just the ones with the correct σ^+ polarization into a polarization-maintaining optical fibre. The write photons are then spectrally filtered by a monolithic Fabry–Perot cavity with about 50 MHz linewidth and 24% total transmission (including subsequent fibre coupling) before finally being detected by SPD D1 with 41% efficiency and a dark count rate of 130 Hz.

To read out the atomic spin-wave, after a storage time of $\tau_A = 1.6\,\mu s$ we send read pulses (derived from the read laser and a subsequent double-pass AOM) which are resonant with the $|s_A\rangle \rightarrow |e_A\rangle$ transition. They propagate in the same optical mode but opposite direction to the write pulses, and their polarization is set to σ^+ by a PBS and a quarter-wave plate. The intensity and temporal wave shape of the read pulses are tailored to efficiently generate read photons with tunable waveform[33].

The read photons are emitted on the $|e_A\rangle \rightarrow |g_A\rangle$ transition and leave the atomic cloud in the opposite direction to the write photons owing to the phase-matching condition $\boldsymbol{k}_r = \boldsymbol{k}_R + \boldsymbol{k}_W - \boldsymbol{k}_w$, where $\boldsymbol{k}_r, \boldsymbol{k}_w$ ($\boldsymbol{k}_R, \boldsymbol{k}_W$) represent the wave vectors of the photonic (pulse) modes. The polarization of the read photons is σ^- when leaving the atomic cloud and is subsequently changed to linear by a quarter-wave plate. The read photons are filtered by a combination of half-wave plate and PBS before they are coupled with an efficiency of approximately 60% into a polarization-maintaining fibre. The fibre is connected to a micro-electromechanical single-mode fibre-optic switch (FS1) which directs the read photons or classical lock light to the QFC interface (see below).

To generate sub-natural-linewidth single photons in the cold atomic quantum memory that exhibit a temporally delocalized wave shape suitable for encoding photonic time-bin qubits, we follow the approach described in earlier work[33]. If a heralding write photon is detected at D1, we map the spin-wave in the Rb quantum memory onto a photonic time-bin qubit depending on the temporal shape of the read pulse. Instead of sending a simple Gaussian-shaped read-out pulse to the cold atomic ensemble, we apply an appropriately imbalanced doubly peaked read-out pulse. The first (early) peak reads out the stored spin-wave with half the retrieval efficiency $\eta^A_{ret}/2$, and the second (late) peak with full retrieval efficiency η^A_{ret}. This creates the desired time-bin read photon with equal photon detection probabilities in both time bins ($c_1 = c_2 = 1/\sqrt{2}$). By controlling the phase φ between the read-out peaks, we can thus create a time-bin photon representing an equatorial qubit state $|\Psi_{eq}\rangle = (|e\rangle + e^{i\varphi}|l\rangle)/\sqrt{2}$.

Moreover, by changing the duration of the read-out peaks, we are able to precisely tune the duration of the whole photon or both time bins individually. We are thereby able to create single photons which exhibit sub-natural linewidths in the range of 2 MHz, matching the spectral requirements of the AFC memory. This also allows us to generate two time bins with identical shape, as needed for high-visibility interference for the coherence preservation and qubit analysis experiments.

Extended Data Fig. 2 shows an example histogram of a time-bin read photon generated at $p_e = 5\%$ in the cold atomic quantum memory detected right after the MOT at site A. Characterization of that photon by a Hanbury Brown–Twiss set-up after the MOT yields a heralded autocorrelation value of $g^{(2)}_{r_A,r_A|w} = 0.26 \pm 0.02$, confirming the single-photon nature of that time-bin read photon.

Solid-state storage device. *Set-up.* The solid-state storage device at site B is a bulk Pr^{3+}:Y_2SiO_5 crystal (Scientific Materials) cooled to 3.5 K in a cryostat (Cryostation, Montana Instruments). With a Pr^{3+} ion concentration of 0.05% and a length of 5 mm, the crystal features a total optical depth of about 10 at the frequency of the $^3H_4 \leftrightarrow {}^1D_2$ transition (see Fig. 1). The laser used to address this transition at 606 nm is a Toptica DL SHG pro, stabilized through the Pound–Drever–Hall technique to a home-made Fabry–Perot cavity in vacuum. From that laser we derive the reference beam for the QFC frequency locking (see below) and the beam necessary to prepare and operate the solid-state memory. The latter beam is modulated in amplitude and frequency by means of a double-pass AOM and is guided to the cryostat through a polarization-maintaining single-mode fibre. It finally arrives at the crystal with a waist of 300 μm and an angle of about 4° with respect to the direction of the converted single photons. These, instead, have a waist at the crystal of 40 μm.

The chosen technique to store the converted single photons is the AFC protocol[34]. It relies on the preparation of a periodic absorptive structure within the inhomogeneously broadened absorption profile of Pr^{3+} which is able to maintain the coherence of the absorbed photons. In fact, a photon absorbed by an AFC with periodicity Δ is mapped into a coherent superposition of atomic excitations that, after a time $\tau_B = 1/\Delta$, experiences a rephasing and gives rise to a collective re-emission in forward direction.

To reshape the absorption profile of the Pr^{3+}:Y_2SiO_5 crystal into an AFC, we follow a procedure similar to that described elsewhere[35]. We first sweep the laser by 12 MHz with a power of 24 mW. This empties the $|\pm 1/2\rangle_g$ and $|\pm 3/2\rangle_g$ hyperfine states of a certain class of atoms and creates an 18-MHz-wide transparency window. We then send 4-MHz-wide burn-back pulses resonant with the transition $|\pm 5/2\rangle_g \leftrightarrow |\pm 5/2\rangle_e$ to pump back atoms in the state $|\pm 1/2\rangle_g$. Subsequent 5-MHz-wide pulses resonant to the $|\pm 3/2\rangle_g \leftrightarrow |\pm 3/2\rangle_e$ transition clean the $|\pm 3/2\rangle_g$ state which was also repopulated by the burn-back pulses. Moreover, the cleaning pulses have the secondary effect of removing from the frequency range of interest any absorption feature associated with other atomic classes. At this stage, we have a 4-MHz-wide, single-class absorption feature resonant to the transition $|\pm 1/2\rangle_g \leftrightarrow |\pm 3/2\rangle_e$, where we finally prepare the AFC. This is done by burning spectral holes with repetitions of low power pulses whose frequency is changed by a fixed amount Δ. For the storage of time-bin qubits, we repeat the latter operation twice with two different periodicities, Δ_1 and Δ_2, such that the AFC gives access to two different storage times, τ_{B1} and τ_{B2}. Extended Data Fig. 3 shows the comb structures and their corresponding echoes for the different storage times used in the experiment.

To protect the SPD from the leakage of the preparation beam, we use a mechanical shutter after the cryostat which remains closed during the whole AFC preparation. Also, the retrieved photons pass through a bandpass filter (Semrock, centred at 600 nm, linewidth 10 nm) before reaching the detection stage, implemented with the SPD D2 (PicoQuant, 45% detection efficiency and 15 Hz dark-count rate).

Qubit analysis. To analyse the phase of the qubit, we use the AFC as an interferometric device[5]. By preparing two AFCs with different periodicities Δ_1 and Δ_2, leading to storage times of $\tau_{B_1} = 2\,\mu s$ and $\tau_{B_2} = 2.5\,\mu s$ (corresponding to the short and long path of the interferometer), the early echo of the late time bin and late echo of the early time bin overlap and interfere. To control the phase of one arm of the interferometer, we exploit the fact that the emitted echo from an AFC acquires a phase shift of $e^{i2\pi\delta/\Delta}$, where δ is the frequency detuning between the centre of the AFC and the input photon, and Δ the periodicity of the comb[34]. Hence, shifting δ for one of the two AFCs allows full control of the interferometer phase and permits us to set the measurement basis.

Density matrices. Here, we provide the numerical result of the quantum-state tomography[36] in the form of density matrices of the three investigated states, estimated by maximum likelihood estimation. On the basis of a Monte Carlo simulation we obtain a 5 s.d. violation of the 66.7% classical threshold[37]:

$$\rho_R = \begin{bmatrix} 0.567 & 0.040 - i0.284 \\ 0.040 + i0.284 & 0.434 \end{bmatrix}$$

$$\rho_+ = \begin{bmatrix} 0.505 & 0.352 + i0.067 \\ 0.352 - i0.067 & 0.495 \end{bmatrix}$$

$$\rho_E = \begin{bmatrix} 0.941 & 0.063 - i0.001 \\ 0.063 + i0.001 & 0.059 \end{bmatrix}$$

AFC versus photon detuning. The AFC storage efficiency as a function of the frequency detuning δ of the input light from the centre of the comb is investigated in Extended Data Fig. 4. The blue dots show the storage efficiency of 606 nm single classical pulses with 200 ns FWHM, on a 4-MHz-wide comb for a storage time of $\tau_B = 2.5\,\mu s$. As expected, the storage efficiency drops when the input light is no longer resonant with the prepared AFC.

Next, double Gaussian pulses separated by 500 ns, mimicking a time-bin qubit with zero relative phase, are stored on two superimposed combs with 2 μs and 2.5 μs storage times, such that the late echo of the early bin and the early echo of the late bin overlap in time and interfere. The green squares show the area of the interfering peak relative to the total input pulse, as a function of the frequency detuning δ of the input light. It shows an oscillating behaviour corresponding to constructive and destructive interferences caused by the frequency detuning of the input light pulses to the centre of the combs, inducing a relative phase shift of $e^{i2\pi(\delta/\Delta_1 - \delta/\Delta_2)} = e^{i2\pi\delta(\tau_1-\tau_2)}$ between the two interfering echoes. As expected, a 2π phase shift is observed for an input frequency detuning δ of 2 MHz corresponding to the 500 ns separation between the early and late bin.

This measurement highlights the importance of laser stabilization in order to achieve high storage efficiency and strong coherence conservation (see below).

The interface. *Quantum frequency conversion set-up.* The interface between the cold atomic ensemble, emitting read photons at 780 nm, and the crystal, storing photons at 606 nm, is based on two QFCDs[38]. The first QFCD shifts the frequency of 780 nm light to the telecommunication C-band by difference frequency generation (DFG). It is based on a proton exchange waveguide inside a PPLN chip, where 780 nm light is coupled together with 1,569 nm pump light derived from an erbium-doped fibre amplifier fed by an external cavity diode laser. Both light fields are combined on a dichroic mirror and coupled into the waveguide by an aspheric lens with efficiencies of $\eta_{cpl}^{780\ nm} = 44\%$ and $\eta_{cpl}^{1,569\ nm} = 36\%$. Inside the temperature-stabilized waveguide, 290 mW of pump light converts 780 nm light to 1,552 nm through DFG, with an internal conversion efficiency of $\eta_{int}^{QFCD1} = 56\%$. After collimating the waveguide output, a combination of two bandpass filters, each with a transmission bandwidth of 7 nm around 1,552 nm and a maximum optical depth of approximately 12 at 1,569 nm, separates the converted light from the pump light. The combined transmission of the bandpass filters and the subsequent coupling into a single-mode telecommunication fibre is 68%, giving a total device efficiency of QFCD1 of $\eta_{dev}^{QFCD1} = 17\%$.

After passing FS1, the converted light is then sent to a second laboratory via a 10 m telecommunication fibre, where the second QFCD shifts the frequency of 1,552 nm light to 606 nm by SFG. QFCD2 is based on a temperature-stabilized ridge-waveguide made of PPLN. The waveguide is pumped by 994 nm radiation, derived from an external cavity diode laser locked via the Pound–Drever–Hall technique to an external reference cavity with 690 kHz linewidth and a free spectral range (FSR) of 1 GHz to reduce its linewidth. The pump light is amplified by a tapered amplifier, sent through a gating AOM and an optical fibre to clean the spatial mode. After its polarization is adjusted by a half-wave plate, the pump light is combined with the 1,552 nm telecommunication light on a dichroic mirror and coupled into the waveguide by an aspheric lens with efficiencies of $\eta_{cpl}^{994\ nm} = 62\%$ and $\eta_{cpl}^{1,552\ nm} = 51\%$, respectively. Inside the waveguide, a 450 mW pump field converts the 1,552 nm light to 606 nm by means of SFG with an internal conversion efficiency of $\eta_{int}^{QFCD2} = 60\%$. After collimating the waveguide output, several optical elements are used to filter the converted light at 606 nm from the pump radiation, the Raman noise from the first QFCD, and the pump spontaneous parametric down-conversion (SPDC) noise generated and converted in the second QFCD. First, a dichroic mirror (transmission $T_{DM}^{1,552\ nm} = 94\%$) is used, before the light is sent to a diffraction grating (diffraction efficiency $\eta_{Gr}^{606\ nm} = 75\%$) and an etalon ($\eta_{Et}^{606\ nm} = 95\%$, FSR=60 GHz, finesse $F = 6$). In between, a half-wave plate and an anamorphic prism pair adjust the polarization for the grating and the spatial mode of the 606 nm light to couple it efficiently into the second fibre switch (FS2), which directs the converted light to the solid-state storage device. The combined transmission of the filtering elements and the subsequent coupling into the single-mode fibre of FS2 is 48%, giving a total device efficiency for QFCD2 of $\eta_{dev}^{QFCD2} = 15\%$.

The probability for a 780 nm photon at the input of FS1 to exit the second fibre switch FS2 at 606 nm is about 1.2%. This includes all possible losses: conversion efficiencies, waveguide coupling, fibre coupling, optical filtering and transmissions (see Extended Data Table 1).

Frequency locking scheme. Active stabilization of the involved laser frequencies is necessary to ensure that the converted read photons emitted by the cold atomic quantum memory are resonant to the AFC structure prepared in the crystal. Therefore, the conversion interface is used in two different configurations: a 'QFC' mode in which the read photons are converted and sent to the AFC memory, and a 'lock' mode in which 780 nm continuous-wave light, derived from the write laser, is converted and used to stabilize the frequency of the converted read photons. Two single-mode fibre switches (FS1 and FS2) placed before and after the interface are used to swap between the two modes.

The first FS placed before the interface has two inputs and one output and the second one after the interface has one input and two outputs. In the QFC mode, the first fibre switch couples the 780 nm read photons to the frequency converters and the second switch directs the converted 606 nm photons to the solid-state storage device. In the lock mode, FS1 couples 2 mW of 780 nm continuous-wave light to the interface and FS2 sends the converted light to the lock system. An optical beat note between the converted 'lock' light and the reference 606 nm laser (used to prepare the AFC structure in the crystal) is measured using a photodiode. The beat note is stabilized at 104 MHz using a frequency comparator (based on a phase-locked loop referenced to an internal clock) which feeds back an error signal to the 1,569 nm pump laser. Any drift of the involved lasers inducing a frequency shift of the converted photons is then compensated by acting on the current of the 1,569 nm pump laser, thus ensuring that the converted 606 nm read photons are resonant to the AFC structure in the crystal.

Experimental time sequence. The time sequence for the experiments presented in the main text is shown in Extended Data Fig. 5. Synchronized on the cryostat cycle of 1 Hz, it starts by preparing the AFC in the crystal for up to 200 ms. Once completed, the master computer sends a trigger to the slave computer that controls the rest of the experiment (see also Extended Data Fig. 1). The main experiment is then performed during the next 290 ms, corresponding to the low vibration time window of the cryostat cycle. The Rb atoms are cooled at site A inside the MOT for 17 ms while the frequency-conversion interface is in the lock mode. The interface is then switched to the QFC mode, and 20-ns-long write pulses are sent to the atomic memory. If a write photon is detected at detector D1, the atomic ensemble is read out after a DLCZ storage time τ_A by sending a 340-ns-long read pulse. The emitted read photon is converted in the QFCDs and afterwards stored for τ_B in the AFC. During the storage, the 994 nm pump is gated off[39] for 5 μs by the AOM behind the tapered amplifier in order to retrieve the read photon in a noiseless time window. The write/read process lasts for 1 ms until the Rb atoms are recaptured by a new MOT and the interface is switched to the lock mode for the next 17 ms. After 15 MOT captures and the corresponding write/read trials, the sequence restarts at the next cryostat cycle, preparing a new AFC in the crystal.

Additional characterizations. *Cross- and autocorrelation measurements.* To gain information about the non-classicality of the generated quantum states, we assess their normalized cross- and autocorrelation functions. In particular, we measure the normalized cross-correlation between the write and read photons

$$g^{(2)}_{w,r} = \frac{p_{w,r}}{p_w p_r}$$

where $p_{w,r}$ is the probability of detecting a coincidence between the write and read photon, and p_w (p_r) is the probability of detecting a write (read) photon. Moreover, we can measure the heralded autocorrelation of a read photon

$$g^{(2)}_{r1,r2|w} = \frac{p_{r1,r2|w}}{p_{r1|w} p_{r2|w}}$$

via a Hanbury Brown–Twiss set-up. Here, $p_{r1,r2|w}$ denotes the probability of measuring a coincidence between both read photon detections conditioned on a write photon detection, and $p_{r1|w}$ ($p_{r2|w}$) is the probability of detecting a read photon on the first (second) detector conditioned on a write photon detection.

The non-classicality of the correlations between write and converted read photons is assessed by the Cauchy–Schwarz inequality, which states that for classical fields the correlation function is bounded by

$$g^{(2)}_{w,r_B} \leq \sqrt{g^{(2)}_{w,w} g^{(2)}_{r_B,r_B}}$$

where $g^{(2)}_{w,w}$ and $g^{(2)}_{r_B,r_B}$ are the unheralded autocorrelation functions of the write and read photons, respectively. The values that we measure to assess the inequality are shown in Extended Data Table 2. The unheralded write photon autocorrelation shows a value of $g^{(2)}_{w,w} \approx 2$ as expected for the ideal two-mode squeezed state generated by the atomic cloud. The unheralded autocorrelation function $g^{(2)}_{r_B,r_B}$ of the read photons at the output of the crystal was not taken because of unfeasible integration times. Instead, we measured its value at the output of the Rb cloud at site A and at the output of the second frequency-conversion stage QFCD2 at site B. The values shown in Extended Data Table 2 indicate that the read photons generated by the atomic cloud exhibit some bunching with $1 \leq g^{(2)}_{r_A,r_A} \leq 2$. The values after the frequency conversion of $g^{(2)}_{r_{QFCD2},r_{QFCD2}} \approx 1$ indicate that the noise added by the QFCDs has Poissonian statistics. Hence, the read photon autocorrelation at the output of the crystal should not have a value higher than 2, indicating that $g^{(2)}_{w,r_B} > 2$ is a strong sign of non-classicality.

Weak coherent state conversion and storage. The QFC interface, the storage in the crystal and the locking system were first tested and characterized with weak coherent states of light mimicking the single read photons and time-bin qubits obtainable from the cold atomic quantum memory.

Using light from the 780 nm write laser which is sent through another AOM beam line and a set of neutral density filters (not shown in Extended Data Fig. 1), we generated attenuated laser pulses of Gaussian shape and 200 ns duration, at the same optical frequency of the read photons from the cold atomic quantum memory. The weak laser pulses are converted through the QFCDs, then stored for $\tau_B = 2.5\,\mu s$ in the crystal and eventually retrieved and detected at D2. The obtained signal-to-noise ratio of the retrieved echo is shown in Extended Data Fig. 6a, as a function of the average input photon number per pulse. The linear fit highlights the performance in terms of signal-to-noise ratio of our system, showing $\mu_1 = 0.022 \pm 0.001$ with μ_1 being the minimum number of photons per pulse at the input necessary to achieve a signal-to-noise ratio of 1 for the detected echo. The echo then shows a signal-to-noise ratio of 14 for an average photon number of 0.3 per pulse at 780 nm, corresponding to the expected number of read photons at the input of the first QFCD per heralded excitation in the cold atomic quantum memory (fibre-coupled DLCZ retrieval efficiency $\eta_{ret}^{A} \approx 30\%$).

Next, weak coherent time-bin qubits (attenuated doubly-peaked Gaussian pulses, separated by 500 ns and with tunable phase difference φ between the early and late bins) were sent through the QFCDs and the solid-state storage device. The memory is prepared with two AFCs offering simultaneous storage for $\tau_{B_1} = 2\,\mu s$ and $\tau_{B_2} = 2.5\,\mu s$. The early and late bins are overlapped and the interference between the early and late pulses is measured as a function of the relative phase φ. The visibility of this interference is shown in Extended Data Fig. 6b as a function of the photon number per time-bin qubit μ_{in}. With strong coherent pulses, the visibility of this interference is measured to be $V_0 = 67\%$. The decrease of visibility for lower input photon number μ_{in} is due to a decrease in signal-to-noise ratio. Taking this effect into account, the visibility becomes[35]

$$V(\mu_{in}) = V_0 \frac{\mu_{in}}{\mu_{in} + 2\beta\mu_1}$$

where V_0 is the maximum visibility, and β the correcting factor for the reduced efficiency of a double AFC compared with a single one. The simple model reproduces our data well, using the signal-to-noise ratio measured in Extended Data Fig. 6a and V_0 measured with strong light pulses (see following section). The visibilities in the single-photon regime, presented in the main text correspond here to a regime where $\mu_{in} \approx 0.3$ (mimicking the retrieval efficiency η_{ret}^{A} of the atomic memory).

Fidelity limitation. In this section, we discuss the limitations of the fidelity measured and presented in the main paper. The fidelity of the polar states is limited by the signal-to-noise ratio (SNR) of the detected photons: $\mathcal{F}_{pol} = (SNR + 1)/(SNR + 2)$. The fidelity of the equatorial states is mainly limited by the visibility of the interference between early and late time bins: $\mathcal{F}_{eq} = (1 + V)/2$. The visibility V depends on background noise (as shown in the previous section) and the overall frequency jitter of the lasers involved in the experiment.

Because of our relatively high signal-to-noise ratio, the main limitation in our case is most likely given by laser jitter, which stochastically shifts the central frequency of the read photon. As seen in the section 'Solid-state storage device', a frequency shift δ induces a relative phase $2\pi\delta(\tau_1 - \tau_2)$ between the two interferometer arms, thus reducing the measured visibility over several experimental trials.

All the lasers involved in the experiment contribute to this effect—the 780 nm read laser generating the time-bin photon, the two pump lasers of the QFCDs converting the time-bin photon, the 780 nm write laser generating the lock light, and the 606 nm laser preparing the AFCs and acting as the reference for the beat-note lock.

Considering a Gaussian global laser linewidth of σ, the visibility V_0 of the interference between the two time bins separated by $\Delta\tau$ can be expressed as[40]

$$V_0 = \exp\left(-\frac{(2\pi\sigma\Delta\tau)^2}{2}\right)$$

Depending on laser stability, maximum visibilities V_0, measured with strong coherent pulses, between 65% and 75% have been observed. This corresponds to a global linewidth of the lasers between 570 and 700 kHz FWHM (approximately 2.35σ). Extended Data Fig. 7 shows the calculated visibility as a function of the FWHM of the Gaussian linewidth. When the pump laser at 994 nm was not stabilized on a Fabry–Perot cavity, we observed a lower maximum visibility, around 60% (corresponding to a visibility of around 50% in the single-photon regime).

Storage time in the crystal. The preservation of non-classical correlations between the write photons (detected at D1 at site A) and the converted, stored and retrieved read photons (detected at D2 at site B) depending on the storage time τ_B in the crystal is investigated in Extended Data Fig. 8.

First, we show in Extended Data Fig. 8a the total detection probability at D2 of a converted and stored read photon when a heralding write photon is detected at D1. For small τ_B we obtain total efficiencies up to 0.02% matching the expected range determined by individual optical losses. The decrease of the total efficiency over storage time follows the drop of the AFC memory efficiency due to the change in finesse and effective optical depth of the prepared AFC at different τ_B caused by the finite laser linewidth[34].

In Extended Data Fig. 8b, the normalized cross-correlation $g^{(2)}_{w,r_B}$ between the write and read photons depending on τ_B is shown. We observe a relatively constant $g^{(2)}_{w,r_B} \approx 6$ up to a storage time of $\tau_B \approx 8\,\mu s$, after which it finally drops below the classical threshold of $g^{(2)}_{w,r} = 2$ at $\tau_B \approx 10\,\mu s$, where the AFC efficiency is low and its echo detection is limited by dark counts of the detector D2. The green area shows the expected correlations, taking into account the signal-to-noise ratio of the AFC echo, inferred from the AFC efficiencies of Extended Data Fig. 8a, using the same model as in previous work[30].

Data availability. The data that support the findings of this study are available from the corresponding author on reasonable request.

33. Farrera, P. *et al.* Generation of single photons with highly tunable wave shape from a cold atomic ensemble. *Nat. Commun.* **7,** 13556 (2016).
34. Afzelius, M., Simon, C., de Riedmatten, H. & Gisin, N. Multimode quantum memory based on atomic frequency combs. *Phys. Rev. A* **79,** 052329 (2009).
35. Gündoğan, M., Ledingham, P. M., Kutluer, K., Mazzera, M. & de Riedmatten, H. Solid state spin-wave quantum memory for time-bin qubits. *Phys. Rev. Lett.* **114,** 230501 (2015).
36. James, D. F. V., Kwiat, P. G., Munro, W. J. & White, A. G. Measurement of qubits. *Phys. Rev. A* **64,** 052312 (2001).
37. Massar, S. & Popescu, S. Optimal extraction of information from finite quantum ensembles. *Phys. Rev. Lett.* **74,** 1259–1263 (1995).
38. Kumar, P. Quantum frequency conversion. *Opt. Lett.* **15,** 1476 (1990).
39. Maring, N. *et al.* Storage of up-converted telecom photons in a doped crystal. *New J. Phys.* **16,** 113021 (2014).
40. Minář, J., de Riedmatten, H., Simon, C., Zbinden, H. & Gisin, N. Phase-noise measurements in long-fiber interferometers for quantum-repeater applications. *Phys. Rev. A* **77,** 052325 (2008).

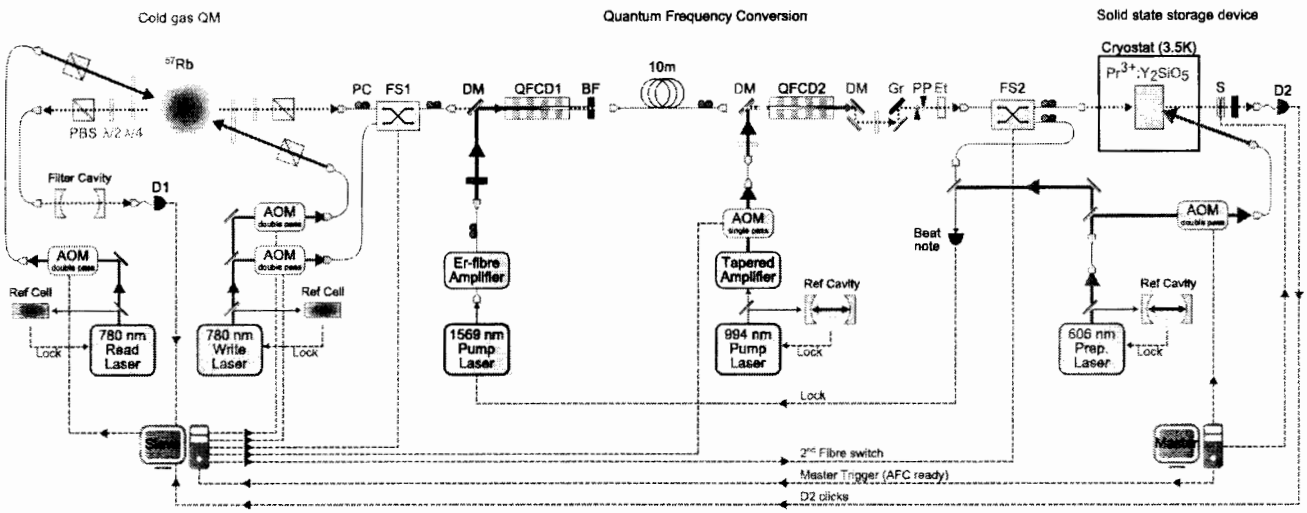

Extended Data Figure 1 | Experimental set-up. On the left, a cold ^{87}Rb quantum memory is operated to generate non-classically correlated photon pairs. In the centre, the single read photons are frequency-converted from 780 nm to 1,550 nm in QFCD1 and afterwards to 606 nm in QFCD2. On the right, the converted read photons are stored and analysed in a crystal before being retrieved and detected. AOM, acousto-optic modulator; BF, bandpass filter; DM, dichroic mirror; Et, etalon; FS, fibre switch; Gr, diffraction grating; $\lambda/2$ ($\lambda/4$) half (quarter)-wave plate; PBS, polarizing beam splitter; PC, polarization controller; PP, anamorphic prism pair; QM, quantum memory; S, mechanical shutter.

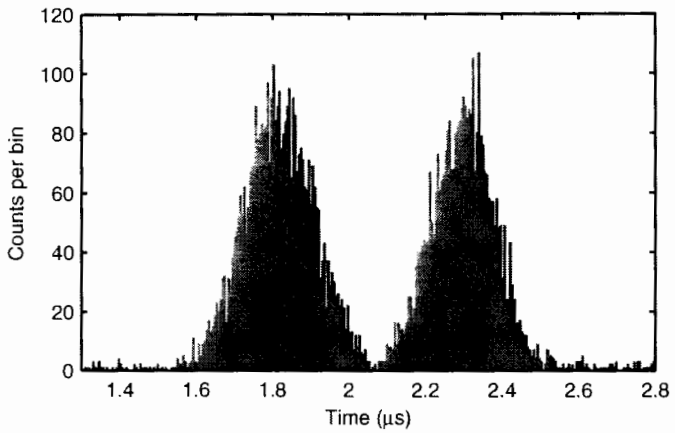

Extended Data Figure 2 | Time-bin read photon. Conditional histogram of a time-bin read photon, taken at $p_e = 5\%$ after the MOT at site A.

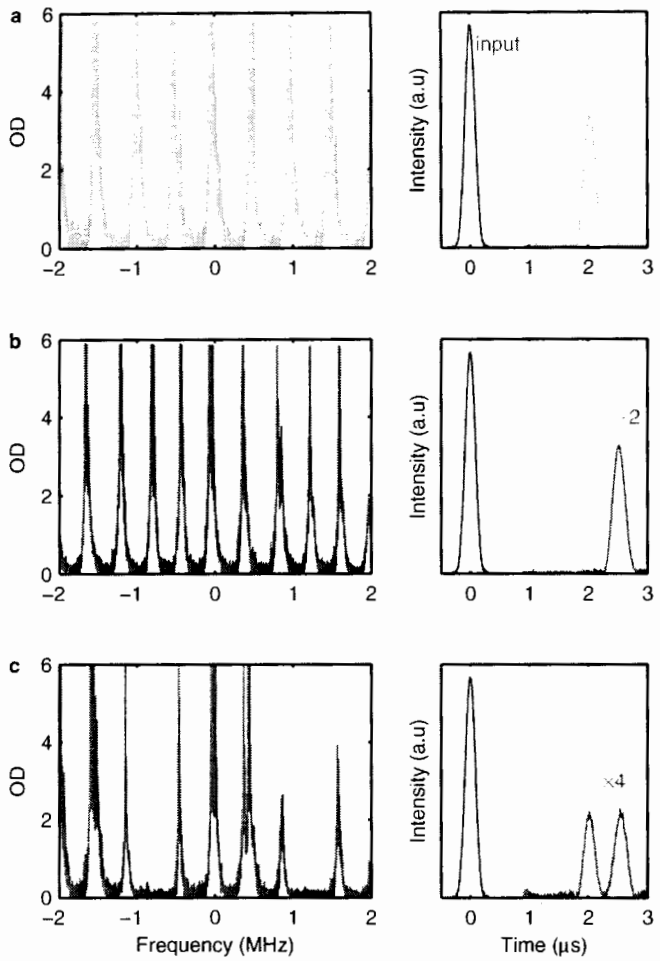

Extended Data Figure 3 | AFC storage characterization. Absorption spectra of AFCs with different periodicities Δ are shown on the left side. Input pulses (200 ns FHWM) derived from the 606 nm preparation laser are sent to the different AFC structures at 0 μs, and their corresponding echoes are shown on the right side. **a**, $\Delta = 500$ kHz. **b**, $\Delta = 400$ kHz. **c**, Double periodicity with $\Delta_1 = 500$ kHz and $\Delta_2 = 400$ kHz leading to a double echo at 2 μs and 2.5 μs. OD, optical depth.

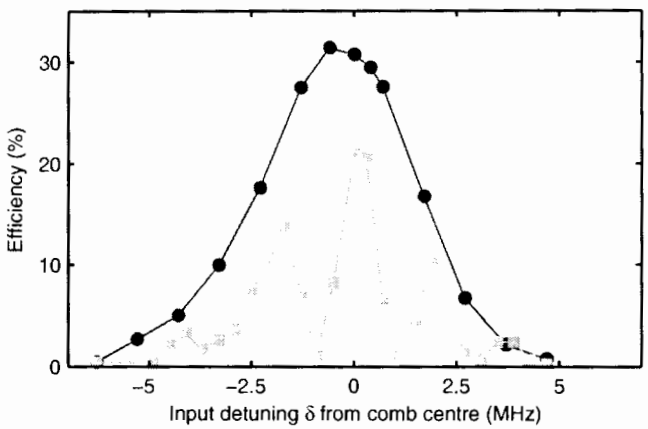

Extended Data Figure 4 | AFC efficiency and interference versus photon detuning. Relative storage efficiency of classical light (derived from the 606 nm preparation laser) versus its frequency detuning δ with respect to the centre of the prepared AFC. For the blue dots, the input is a single Gaussian shaped pulse stored in a single AFC. For the green squares, the input is a doubly peaked pulse (mimicking a time-bin input photon) stored on two superimposed AFCs.

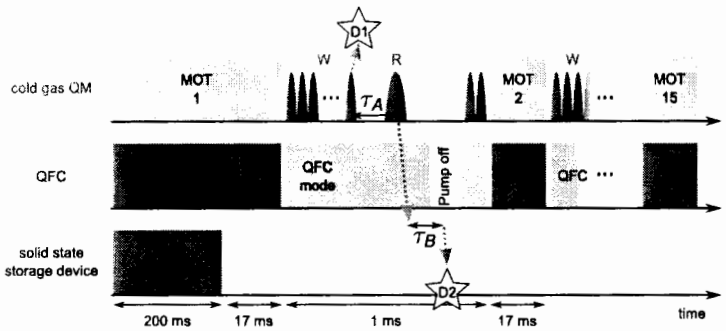

Extended Data Figure 5 | Experimental time sequence. First, the AFC in the crystal is prepared (bottom row), before the main experiment involving the cold atomic quantum memory (top row) and the conversion interface (centre row) starts. Eventual detections of write photons at D1 and converted, stored and restored read photons at D2 are indicated by stars.

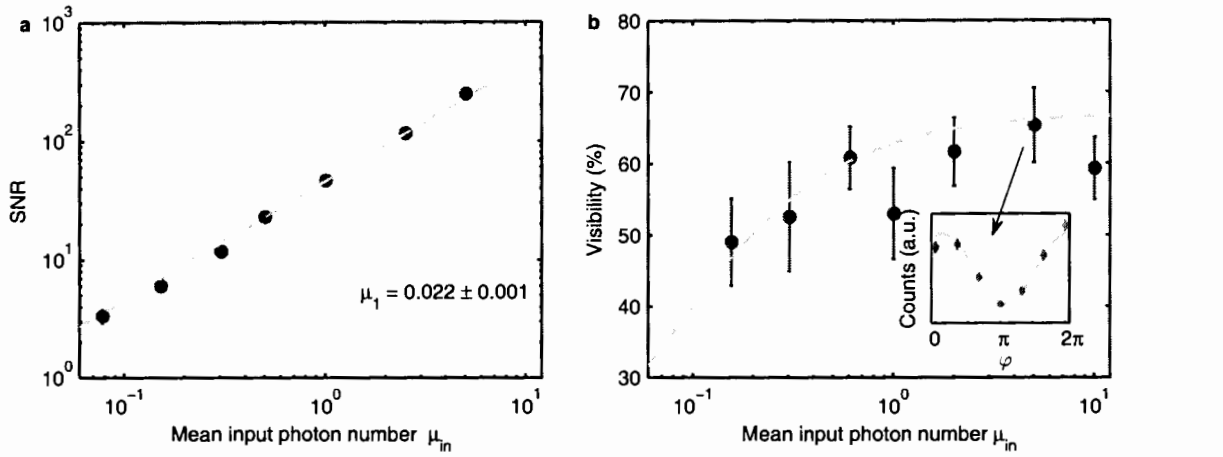

Extended Data Figure 6 | Weak coherent-state measurements. a, Signal-to-noise ratio of the echo retrieved from the crystal, if a weak coherent state is frequency-converted in the QFCDs and stored in the memory depending on the mean input photon number per pulse μ_{in} before the interface. The green line is a fit with the expected linear behaviour. **b**, Visibility of interfering weak coherent time-bin pulses depending on their mean input photon number μ_{in}, after the pulses were frequency converted and stored for $\tau_{B_1} = 2\,\mu s$ and $\tau_{B_2} = 2.5\,\mu s$ in the AFC memory. The green line is the predicted behaviour of the visibility, taking into account the measured signal-to-noise ratio. The inset shows as an example the interference fringe taken at $\mu_{in} \approx 5$.

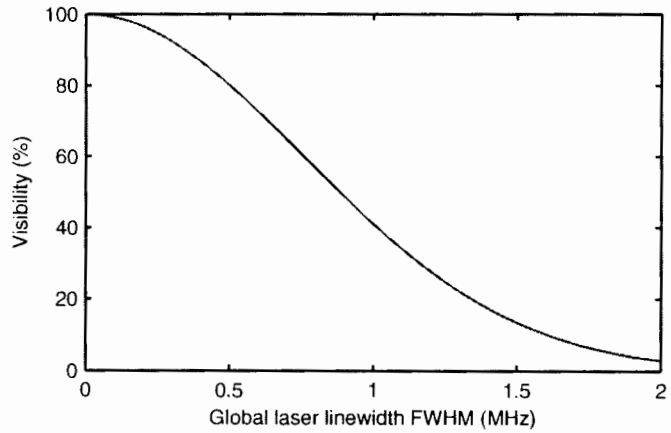

Extended Data Figure 7 | Interference visibility. Calculated visibility V_0 as a function of the laser linewidth FWHM (2.35σ). The shaded area shows the typical operating range of the experiment.

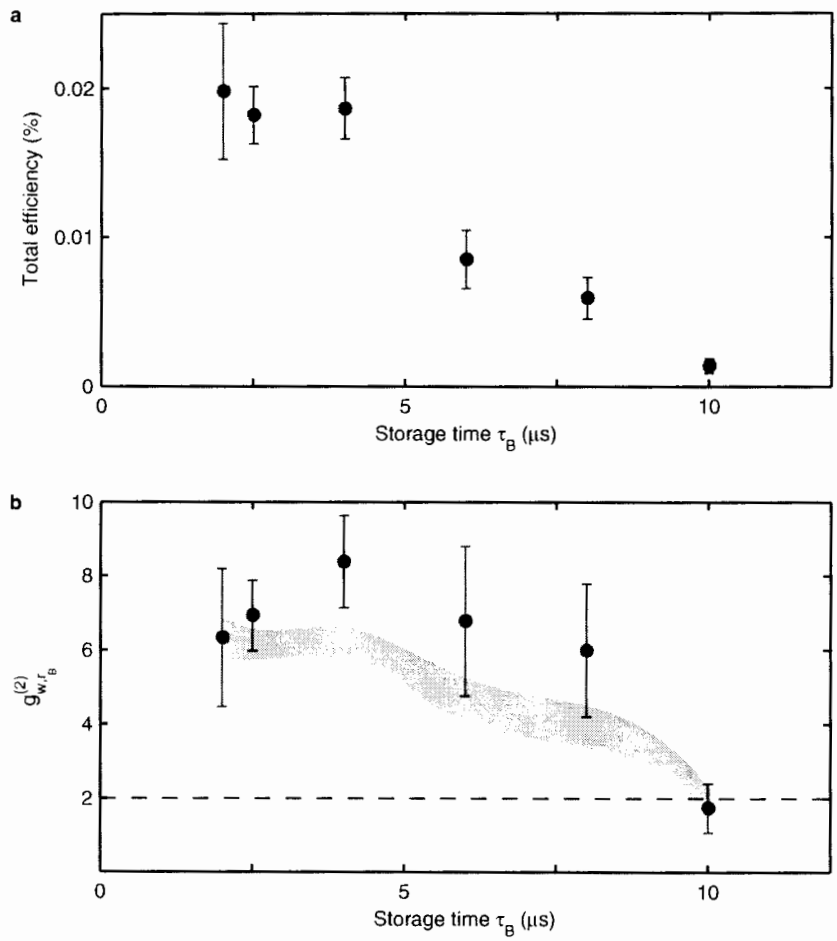

Extended Data Figure 8 | Storage efficiency and cross-correlation versus storage time. a, Total storage efficiency and **b**, normalized cross-correlation function $g^{(2)}_{w,r_B}$ of the initial write photon at site A and the converted, stored and retrieved read photon at site B depending on the storage time τ_B in the crystal, taken at $p_e \approx 10\%$.

Extended Data Table 1 | System losses

Element	Type of loss	T, η (%)	
Cold Gas	Read retrieval (in fibre)	30	
FS1	Transmission	72	
QFCD1	Waveguide coupling	44	$\eta_{device} = 17\ \%$
	Conversion	56	
	Filtering & fibre coupling	68	
QFCD2	Waveguide coupling	51	$\eta_{device} = 15\ \%$
	Conversion	60	
	Filtering	75	
	Fibre coupling	64	
FS2	Transmission	70	
Crystal	AFC storage	29	
	Optical transmission	52	
	Detection	45	

Detailed optical transmissions and efficiencies of the experiment are shown.

Extended Data Table 2 | Unheralded autocorrelation measurements

p_e[%]	$g^{(2)}_{w,w}$	$g^{(2)}_{r_A,r_A}$	$g^{(2)}_{r_{QFCD2},r_{QFCD2}}$
35	1.97(0.10)	1.36(0.05)	1.06(0.05)
10	1.91(0.10)	1.48(0.06)	0.96(0.04)
5	2.13(0.20)	1.35(0.07)	1.00(0.04)

Normalized autocorrelation values for the write and read photon fields. $g^{(2)}_{w_A,w_A}$ is measured after the write photons are filtered with the Fabry–Perot cavity. $g^{(2)}_{r_A,r_A}$ is measured at the output of the fibre that collects the read photons from the atomic cloud. $g^{(2)}_{r_{QFCD2},r_{QFCD2}}$ is measured at the output of QFCD2 at site B.

Cavities play a fundamental role in wave phenomena from quan-tum mechanics to electromagnetism and dictate the spatiotemporal physics of lasers. In general, they are constructed by closing all channels through which waves can escape. We report, at room temperature (295 K), a BIC laser that harnesses optical modes residing in the radiation continuum but, nonetheless, possess arbitrarily high quality factors, Q. These counterintuitive cavities are based on resonance-trapped, symmetry-compatible modes that destructively interfere.

Generally, open systems are described by non-Hermitian effective Hamiltonians that have multivariate and complex eigenvalues describing modes of the system. These eigenvalues exist in a multidimensional hyperspace but, in a given frequency range, the investigation can be reduced to a finite number of variables, thus limiting the complexity of the effective Hamiltonian[7]. When eigenvalues come close to crossing as a function of a geometrical parameter that modifies the system, avoided resonance crossing occurs, that is, eigenvalues repel each other in the entire complex plane[19–21]. Friedrich and Wintgen showed that resonance-trapped BICs represent a particular type of avoided resonance crossing for which coupling occurs predominantly in the far-field.

Our system consists of a thin membrane of semiconductor material suspended in air. We subsequently structure the membrane at the nanometre scale. The field in the air is a superposition of independent waves, which are interpreted as decay channels, and can be either propagating or evanescent. The field in the membrane, which becomes a superposition of coupled waves owing to structuring, is also coupled to the field in air. In the resulting open system described by a non-Hermitian Hamiltonian, the imaginary part of the complex eigenfrequency serves to quantify the decay of modes via the resonance lifetime. This lifetime is governed by coupling amongst different waves within the membrane through the Fourier coefficients of the periodic permittivity. A precise engineering of coupling among relevant waves in reciprocal space can lead to total destructive interference, that is, an infinite lifetime (see section A of Supplementary Information). BICs arise in the limit when a complex eigenfrequency mode tends towards a purely real eigenfrequency mode. They are very peculiar discrete modes in that they are actually embedded within the continuous spectrum but intrinsically possess an infinitely high radiation quality factor as a result of their

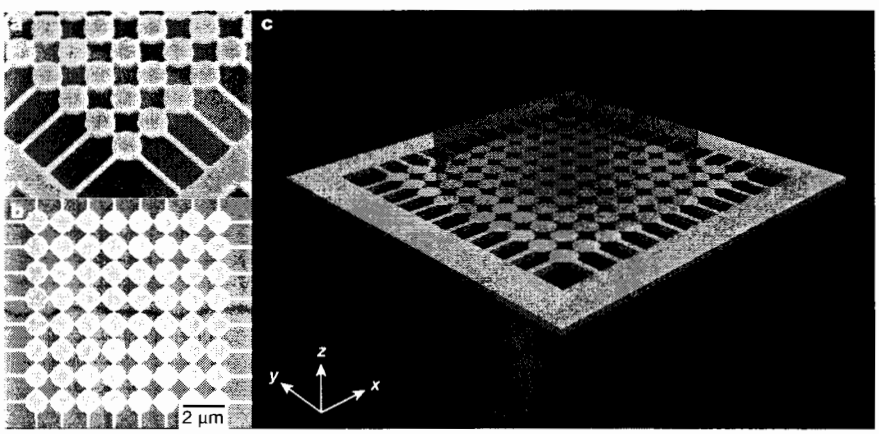

Figure 1 | BIC laser. a, Tilted electron micrograph of InGaAsP multiple quantum wells cylindrical nanoresonator array suspended in air. All structures are fabricated using electron beam lithography followed by reactive ion etching to form the cylinders. We subsequently use wet etching to suspend the structure (see section B of Supplementary Information). **b**, Top view of an 8-by-8 array with supporting bridges, which are used for the mechanical stability of the membrane. The dimensions of the structure are the period (1,200 nm), the thickness (300 nm) and the bridge width (200 nm). **c**, Schematic of the fabricated system illustrating the pump beam (blue) and lasing from the BIC mode (red). The radius of the cylindrical nanoresonators is the key parameter in our BIC design.

[1]Department of Electrical and Computer Engineering, University of California San Diego, La Jolla, California 92093-0407, USA.
*These authors contributed equally to this work.

non-decaying nature. BICs are thus ideally suited for the design of perfect nanophotonic cavities.

As shown in Fig. 1, our BIC cavity is composed of a periodic array of nanoresonators of radius R interconnected by a network of supporting bridges used for the mechanical stability of the system. The membrane consists of several $In_xGa_{1-x}As_yP_{1-y}$ multiple quantum wells, specially designed to operate around the telecommunication wavelength ($\lambda \approx 1.55\,\mu m$). The radius of the cylindrical nanoresonators is the only parameter we use to tune the modes of the membrane and alter the effective Hamiltonian. The structure is fabricated using electron-beam lithography and reactive ion etching to define the cylindrical nanoresonators, followed by a wet etching step to create the membrane (see section B of Supplementary Information). It is worth noting that the radii of the fabricated nanoresonators are always smaller than their nominal design values, a consequence of reactive ion etching. As a result, the maximum achievable radius is strictly smaller than $a/2$ where a is the period of our structure.

To analyse our system, we calculate the quality factors at normal incidence around 1.55 μm, that is, within the gain bandwidth of the material. The system was modelled using a three-dimensional finite-element-method eigenfrequency solver. We restrict the discussion to odd modes (transverse-magnetic-like) as they have much higher quality factors than even modes (transverse-electric-like) in the wavelength range of interest (see section C of Supplementary Information). We find three modes around 1.55 μm with appreciable quality factors, one doubly degenerate mode (modes 1 and 2) and one singly degenerate mode (mode 3). Figure 2a shows their quality factor as a function of the radius ($522\,nm \leq R \leq 534\,nm$). The quality factor of mode 3 is independent of the radius and remains high throughout the calculated range. This mode corresponds to a symmetry-protected mode[22]. In contrast, the quality factor of modes 1 and 2 depends strongly on the radius and reaches a maximum at an optimum radius of $R_{opt} = 528.4\,nm$. At this optimum radius, modes 1 and 2 completely decouple from the radiation continuum and thus become BICs. This mode corresponds to a resonance-trapped mode (see section D of Supplementary Information).

The quality factor can diverge in two different situations. In the first situation (mode 3), coupling to the outside vanishes solely as a result of symmetry mismatch. Any perturbation that preserves symmetry, such as a modification of the radius, has no impact on its quality factor. This type of mode has been extensively studied before[23]. In the second situation (modes 1 and 2), coupling to the outside vanishes as a result of total destructive interference[13,24]. This BIC mode (resonance-trapped) is fundamentally different from previous works on band-edge lasers[25–27] (symmetry-protected) that are restricted to high symmetry points of the reciprocal lattice (see section E of Supplementary Information). Resonance-trapped BICs achieve an infinite quality factor at the singular radius R_{opt} but the quality factor remains very high for radii around R_{opt}. Figure 2b shows the transmission spectrum at normal incidence of our structure, in which the quality factor of modes 1 and 2 can be seen to tend slowly to infinity from its vanishing linewidth.

Figure 2c shows the dispersion relation of the BIC structure at $R = R_{opt}$ along the MΓ and ΓX directions. Here Γ, X, and M are high-symmetry points of the first Brillouin zone for a square lattice. We also plot the complex dispersion relation of modes 1 and 2 (Fig. 2d, e) and mode 3 (Fig. 2f). Figure 2f shows that mode 3 is extremely sensitive to symmetry-breaking perturbations as its quality factor drops sharply away from the Γ point. Quality factors of modes 1 and 2, which are no longer

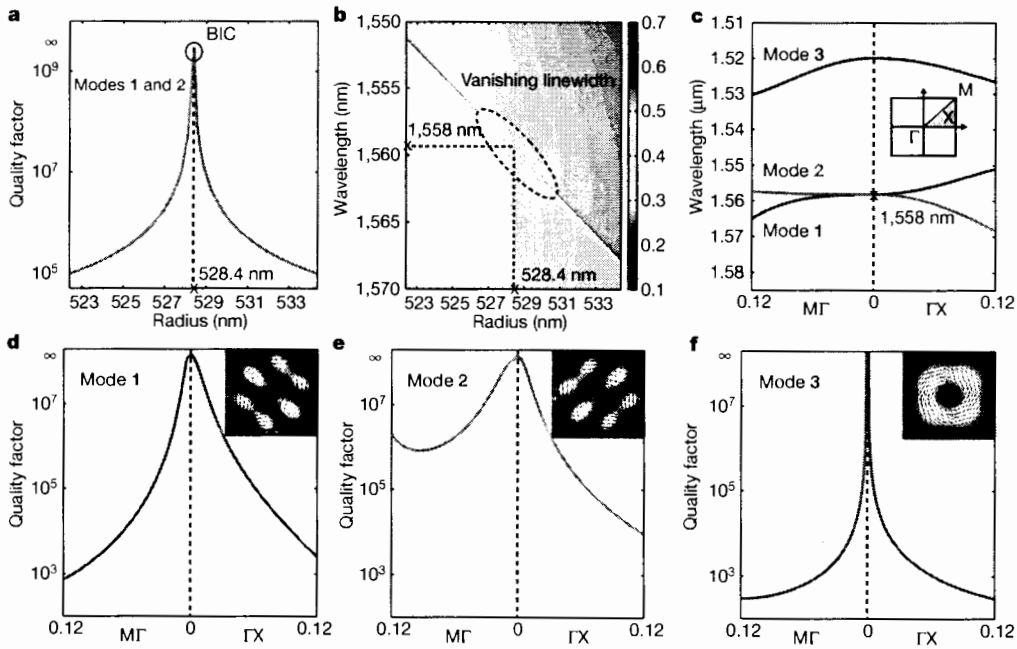

Figure 2 | Design and complex dispersion relation of the BIC cavity. a, Quality factor of high-Q modes at the Γ point around the telecommunication wavelength for different nanoresonator radii. The quality factors of modes 1 and 2, which are doubly degenerate at the Γ point, are strongly dependent on the radius R. For $R = R_{opt}$ at 528.4 nm, this quality factor approaches infinity to form a resonance-trapped BIC. For radii around R_{opt} the quality factor remains very high. **b**, Transmission spectrum at normal incidence showing the vanishing linewidth of modes 1 and 2 when the radius approaches R_{opt}. The wavelength of the modes is a function of the radius and it continuously varies between the smallest radius ($R = 522$ nm) and the largest radius ($R = 534$ nm). **c**, Dispersion relation around 1.55 μm for high-Q modes (1, 2 and 3) in both MΓ and ΓX directions as a function of $k(a/2\pi)$. The inset shows the first Brillouin zone of the square lattice and irreducible contour for cylindrical nanoresonators (shaded area). The contour connects high-symmetry points Γ, X, and M. **d**–**f**, Quality factor of high-Q modes in both the MΓ and the ΓX direction for mode 1 (**d**), mode 2 (**e**), and mode 3 (**f**). Insets represent the normalized electric field on the surface of a unit cell. Modes 1 and 2 are identical under 90-degree rotation. Mode 3 is a symmetry-protected mode and is thus not affected by geometrical changes that preserve symmetry, such as the change of radius. The quality factor of mode 3, however, drops rapidly away from the high-symmetry point Γ. It drops more rapidly compared to the quality factor of modes 1 and 2. The sharper drop of the quality factor of mode 3 away from Γ implies that the integrated quality factor of this mode will be smaller than those of modes 1 and 2 in the case of finite-sized samples.

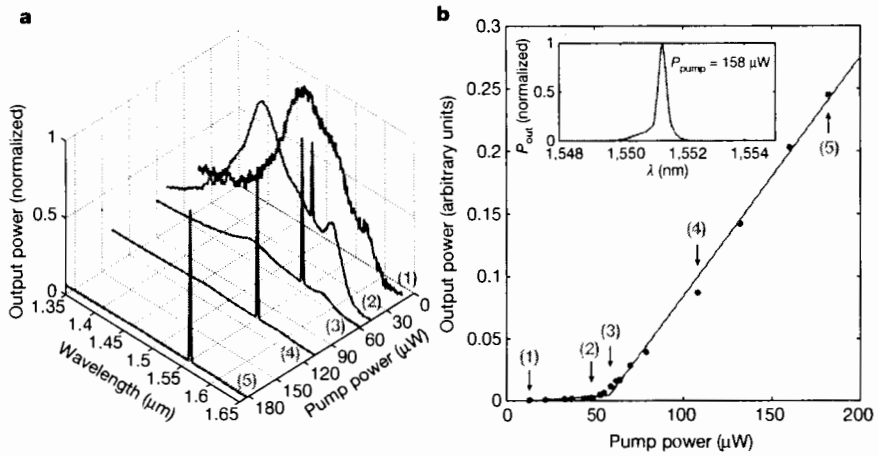

Figure 3 | Experimental characterization of the BIC laser. a, Evolution of the normalized output power as a function of wavelength and pump power for a 16-by-16 array with a nanoresonator radius of 525 nm. We observe the transition from a broad spontaneous emission to a single lasing peak at 1,551.4 nm. **b**, Output power as a function of the average pump power (light–light curve) around the lasing wavelength. We observe the onset of lasing at a threshold power of 56 μW. The red lines are linear fits to the data, indicating the regions of spontaneous and stimulated emission. The blue dots correspond to measurements and numbers (1) to (5) denote the spectra plotted in **a**. Here the standard error in arbitrary units is less than 0.01. The inset shows the lasing spectrum at a pump power of 158 μW with a measured linewidth of about 0.33 nm (detection-limited).

degenerate away from the Γ point (as seen in Fig. 2c), do not drop as sharply as that of mode 3. Modes 1 and 2 are thus much less sensitive to symmetry-breaking perturbations. Additionally, the resonance-trapped BIC is robust because a variation in radius only induces its displacement in k-space (reciprocal space, where k is the wavevector), whereas a symmetry-breaking perturbation destroys the symmetry-protected mode[13]. This is of utmost importance in device design as fabrication tolerances will have less impact on resonance-trapped BICs than on modes that rely on symmetry protection. Moreover, designing a mode with a high quality factor in a large region of k-space is of practical importance because fabricated devices, which are never spatially infinite, always sample the dispersion relation in a finite neighbourhood in k-space[28]. Therefore, for a given quality factor, we can achieve a much smaller device footprint with a resonance-trapped BIC mode than with symmetry-protected modes.

To experimentally demonstrate lasing from our BIC cavity, we optically pump the membrane at room temperature with a pulsed laser ($\lambda = 1{,}064$ nm, $T = 12$ ns pulse at a repetition rate $f = 300$ kHz) and record the spectral emission (see section F of Supplementary

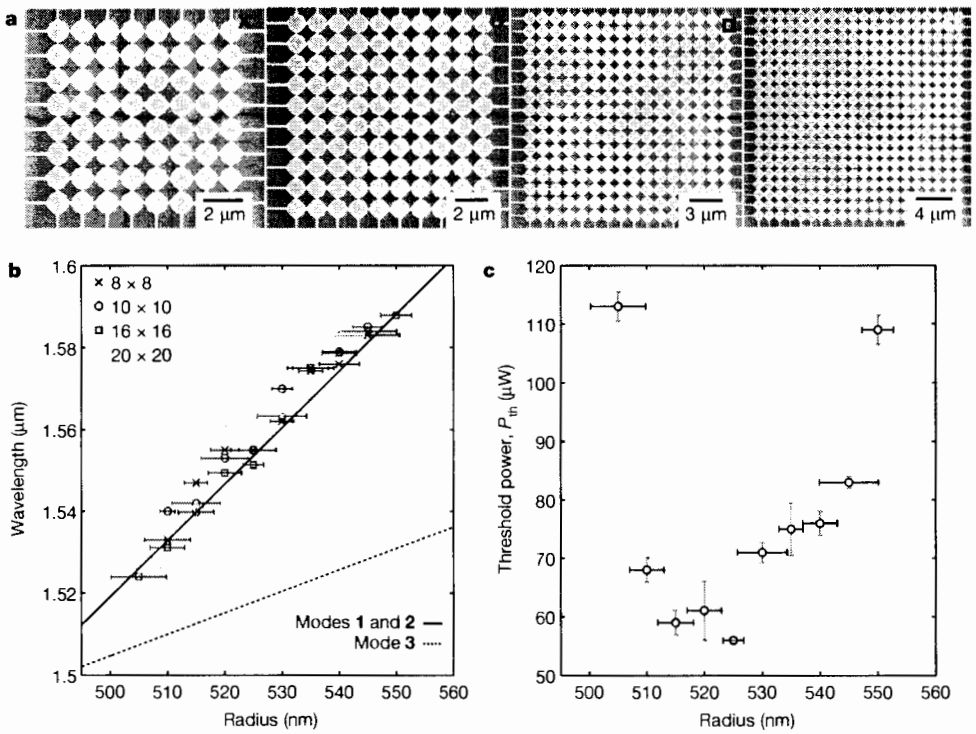

Figure 4 | Scaling of the BIC lasers. a, Electron micrographs of fabricated BIC lasers of size 8-by-8, 10-by-10, 16-by-16, and 20-by-20. **b**, Lasing wavelength as a function of nanoresonator radius, from 500 nm to 550 nm, with array sizes of 8-by-8 (cross), 10-by-10 (circle), 16-by-16 (square), and 20-by-20 (diamond). Each point corresponds to a device with a specific radius, bridge width and array size. Error bars indicate the standard deviation of radii measured from fabricated devices. The lines represent the theoretical resonant wavelength of modes 1 and 2 (solid line) and 3 (dashed line) for different radii of nanoresonators, for the infinite array. The good agreement between the experimental lasing wavelengths and the theoretical resonant wavelengths of the resonance-trapped BIC mode (modes 1 and 2) confirms that lasing action is indeed from the BIC mode. **c**, Additionally, measured threshold power as a function of radii for the lasers clearly shows a minimum (56 μW) close to R_{opt} (about 525 nm) reflecting the maximum quality factor around the BIC singularity and offers further proof of lasing action from the BIC mode (modes 1 and 2). The inverse relationship between quality factor and threshold is evident (see section G of Supplementary Information). Mode 3 has no variation in quality factor with radii. The vertical error bars are the standard error in the threshold power estimated over multiple measurements (varying pump power) repeated more than three times whereas the horizontal error bars represent the standard deviation of measured radii. The green shaded area is a guide to the eye.

Information). Figure 3a shows the evolution of the output power as a function of both the pump power and the wavelength. At low pump power, we observe a spectrally broad photoluminescence spectrum, while at high pump power, we observe a drastic overall suppression of the photoluminescence in favour of one extremely narrow peak, that is, lasing. As depicted in Fig. 3a, three modes show amplification at first ($P_{pump} \approx 48\,\mu W$) but, ultimately, only one remains. Lasing action occurs at a wavelength of 1,551.4 nm with a detection-limited linewidth of about 0.33 nm (see inset of Fig. 3b). Figure 3b shows the evolution of the output power as a function of the pump power around this lasing wavelength. We observe a clear threshold behaviour with a threshold power of $56\,\mu W$ or a density of $140\,mW\,mm^{-2}$.

To further demonstrate the robustness and scalability[29] of our BIC laser, we fabricated several devices (36 devices) with a range of radii and array sizes as seen in Fig. 4a. Figure 4b shows the measured lasing wavelength of devices of different array size (8-by-8, 10-by-10, 16-by-16 and 20-by-20), and different radii of nanoresonators. The solid and dashed lines represent, respectively, the theoretical resonant wavelength of modes 1 and 2 and mode 3 for different radii of nanoresonators in the infinite array. We observe a very good agreement between the experimental lasing wavelengths and the theoretical resonant wavelengths of the resonance-trapped BIC mode (modes 1 and 2). This agreement confirms that lasing action is indeed from the BIC mode over the entire range of radii. Moreover, the persistence of lasing for all array sizes down to as few as 8-by-8 nanoresonators shows the scalability of our BIC laser, thanks to the large quality factor of the resonance-trapped BIC mode in a wide region of k-space. Further evidence of lasing from the BIC mode can directly be observed in the measured threshold power of the lasers. The threshold power has a clear minimum close to R_{opt} (about 525 nm), reflecting a maximum quality factor at the BIC singularity as seen in Fig. 4c. Also see section G of Supplementary Information for a discussion on the influence of quality factor for a finite cavity on the lasing threshold. Additional characterization such as far-field profiles and polarization measurements of these lasing devices are provided in section H of Supplementary Information.

We have thus reported a BIC laser from a cavity mode that can, surprisingly, have arbitrarily high quality factors despite being embedded in the continuum of radiation modes. This cavity, made of an array of suspended cylindrical nanoresonators, shows persistent single-mode lasing for various radii and array sizes. The lasing wavelength follows the theoretical prediction of the BIC mode and the inverse relationship between quality factor and lasing threshold is experimentally demonstrated. These results demonstrate the robustness and scalability of the system. The ability to confine light within the radiation continuum opens up the study of the intriguing topological physics of BICs and the realization of non-standard photonic devices, sensors and sources.

Online Content Methods, along with any additional Extended Data display items and Source Data, are available in the online version of the paper; references unique to these sections appear only in the online paper.

Data Availability The data that support the findings of this study are available from the corresponding author upon reasonable request.

Received 8 July; accepted 8 November 2016.

1. von Neumann, J. & Wigner, E. On some peculiar discrete eigenvalues. *Phys. Z.* **30,** 467 (1929).
2. Herrick, D. R. Construction of bound states in the continuum for epitaxial heterostructure superlattices. *Physica B* **85,** 44–50 (1976).
3. Stillinger, F. H. Potentials supporting positive-energy eigenstates and their application to semiconductor heterostructures. *Physica B* **85,** 270–276 (1976).
4. Friedrich, H. & Wintgen, D. Interfering resonances and bound states in the continuum. *Phys. Rev. A* **32,** 3231–3242 (1985).
5. Hsu, C. W., Zhen, B., Stone, A. D., Joannopoulos, J. D. & Soljačić, M. Bound states in the continuum. *Nat. Rev. Mater.* **1,** 16048 (2016).
6. Linton, C. M. & McIver, P. Embedded trapped modes in water waves and acoustics. *Wave Motion* **45,** 16–29 (2007).
7. Lepetit, T. & Kanté, B. Controlling multipolar radiation with symmetries for electromagnetic bound states in the continuum. *Phys. Rev. B* **90,** 241103(R) (2014).
8. Marinica, D. C. *et al.* Bound states in the continuum in photonics. *Phys. Rev. Lett.* **100,** 183902 (2008).
9. Bulgakov, E. N. & Sadreev, A. F. Bound states in the continuum in photonic waveguides inspired by defects. *Phys. Rev. B* **78,** 075105 (2008).
10. Dreisow, F. *et al.* Adiabatic transfer of light via a continuum in optical waveguides. *Opt. Lett.* **34,** 2405–2407 (2009).
11. Plotnik, Y. *et al.* Experimental observation of optical bound states in the continuum. *Phys. Rev. Lett.* **107,** 183901 (2011).
12. Weimann, S. *et al.* Compact surface Fano states embedded in the continuum of waveguide arrays. *Phys. Rev. Lett.* **111,** 240403 (2013).
13. Hsu, C. W. *et al.* Observation of trapped light within the radiation continuum. *Nature* **499,** 188–191 (2013).
14. Monticone, F. & Alù, A. Embedded photonic eigenvalues in 3D nanostructures. *Phys. Rev. Lett.* **112,** 213903 (2014).
15. Molina, M. I., Miroshnichenko, A. E. & Kivshar, Y. S. Surface bound states in the continuum. *Phys. Rev. Lett.* **108,** 070401 (2012).
16. Zhang, M. & Zhang, X. Ultrasensitive optical absorption in graphene based on bound states in the continuum. *Sci. Rep.* **5,** 8266 (2015).
17. Zhen, B., Hsu, C. W., Lu, L., Stone, A. D. & Soljačić, M. Topological nature of optical bound states in the continuum. *Phys. Rev. Lett.* **113,** 257401 (2014).
18. Miyai, E. *et al.* Photonics: Lasers producing tailored beams. *Nature* **441,** 946 (2006).
19. Sadreev, A. F., Bulgakov, E. N. & Rotter, I. Bound states in the continuum in open quantum billiards with a variable shape. *Phys. Rev. B* **73,** 235342 (2006).
20. Wiersig, J. Formation of long-lived, scarlike modes near avoided resonance crossings in optical microcavities. *Phys. Rev. Lett.* **97,** 253901 (2006).
21. Persson, E., Rotter, I., Stöckmann, H.-J. & Barth, M. Observation of resonance trapping in an open microwave cavity. *Phys. Rev. Lett.* **85,** 2478–2481 (2000).
22. Sakoda, K. *Optical Properties of Photonic Crystals* Chs 3, 8 (Springer, 2005).
23. Fan, S. & Joannopoulos, J. D. Analysis of guided resonances in photonic crystal slabs. *Phys. Rev. B* **65,** 235112 (2002).
24. Yang, Y., Peng, C., Liang, Y., Li, Z. & Noda, S. Analytical perspective for bound states in the continuum in photonic crystal slabs. *Phys. Rev. Lett.* **113,** 037401 (2014).
25. Kogelnik, H. & Shank, C. V. Stimulated emission in a periodic structure. *Appl. Phys. Lett.* **18,** 152–154 (1971).
26. Meier, M. *et al.* Laser action from two-dimensional distributed feedback in photonic crystals. *Appl. Phys. Lett.* **74,** 7–9 (1999).
27. Imada, M. *et al.* Coherent two-dimensional lasing action in surface-emitting laser with triangular lattice photonic crystal structure. *Appl. Phys. Lett.* **75,** 316–318 (1999).
28. Xu, T., Yang, S., Nair, S. V. & Ruda, H. E. Confined modes in finite-size photonic crystals. *Phys. Rev. B* **72,** 045126 (2005).
29. Koenderink, A. F., Alù, A. & Polman, A. Nanophotonics: Shrinking light-based technologies. *Science* **348,** 516–521 (2015).